REPUBLIQUE ALGERIENNE DEMOCRATIQUE ET POPULAIRE

MINISTERE DE L'ENSEIGNEMENT SUPERIEUR ET DE LA RECHERCHE SCIENTIFIQUE

UNIVERSITE MOHAMED BOUDIAF - M'SILA

FACULTE DE TECHNOLOGIES
DEPARTEMENT DE GENIE ELECTRIQUE

N° : . . . . . .

DOMAINE : Génie Electrique

FILIERE : Electrotechnique
OPTION : Commande Electrique

Mémoire présenté pour l'obtention du diplôme de Master Académique

Par:

BEN KAIHOUL Nasr eddine

REBAII Ameur

Intitulé

LQR Control of Parallel Distributed Generation Units Based Islanded Microgrid

Soutenu devant le jury composé de:

DJERIOUI Ali	Université Mohamed Boudiaf de M'Sila	Président
BELLA Saad	Université Mohamed Boudiaf de M'Sila	Rapporteur
BARKAT Said	Université Mohamed Boudiaf de M'Sila	Co-Rapporteur
ZORIG Abdelmalik	Université Mohamed Boudiaf de M'Sila	Examinateur

2021 / 2022

Acknowledgement

أولا نشكر الله عز وجل الذي بتوفيقه وبفضله تمكنا من انجاز هذه المذكرة.

We would like to thank and offer our greatest gratitude and appreciation to our supervisors Mr. Bella Saad and Mr. Barkat Said who have been extremely helpful with their priceless support and guidance throughout this work, and for providing us with valuable comments and suggestions during the development of this work.

Our thanks go to the members of the board of examiners for accepting to read, evaluate, and comment on this thesis.

We would also like to give special thanks to our families as a whole for their continuous support and understanding when undertaking our research and writing our project.

List of figures

List of Tables

Nomenclature

DC	DC-Bus Voltage
AC	Direct Current
f	Frequency
f_{sw}	Switching Frequency
k_p	Proportional Gain
k_i	Integrator Gain
I_{iabc}	Input Three-Phase Currents
V_{iabc}	Input Three-Phase Voltages
I_{oabc}	Output Three-Phase Currents
V_{oabc}	Output Three-Phase Voltages
I_{dq}	dq-axes Currents
I_{dq}^*	dq-axis Reference Current
V_{dq}^*	dq-axis Reference Voltage
L_f	Filter Inductance
r	Filter Resistance
C_f	Filter Capacitance
P	Active Power
Q	Reactive Power
P^*	Reference Active Power
Q^*	Reference Reactive Power
V_{dq}	dq-axes Voltages
V_{dq}^*	Reference dq-axes Voltage
T	Sampling Period

ζ	Damping Factor
ω	Angular Frequency
ω_n	Natural Frequency
Z_o	Output Impedance
DG	Distributed Generation
MG	Micro-Grid
SVPWM	Space Vector Pulse Width Modulation
LQR-I	Linear Quadratic Regulator with Integrator
PI	Proportional Integral Control
PIL	Processor In the Loop
VSI	Current Source Converter

General Introduction

Nowdays, the primary sources of electricity in the world are from fossil fuels; corresponding to 75% of the world electric energy production. The rationale of their domination is the accessibility of the fuel and its high energy density once it is combusted. Since fossil fuels need many years to be exploitable, they are classified as non-renewable energy sources; these sources will soon be used and cannot meet the growing energy demands [1]. In addition, there is a unanimous consensus that the combustion of fossil fuels is damaging the environment. With a view to keeping the environment clean, these fossil fuels are now being replaced by the renewable energy sources (RESs) such as solar, wind, geothermal, hydro and so on [2]. For example in Algeria the growth rate of electricity consumption was around 11.5% in 2010/2011 reaching 14 GW in 2014. In order to foster the national electricity production capacity and reduce the environmental impacts, a national renewable energy programme 2011/2030 has been adopted. The national PV solar energy production strategy consists of the construction of 23 solar power plants in the Central Highlands Ain Azel (Setif), Ras el Oued (Bordj Bou Arreridj), Oued El Ma (Batna), Chelghoum El Eid (Mila), Ain El Melh (M'sila), etc [3].

Commonly, power systems are structured such that the power flow is done in one main direction, starting from power stations with large central generators connected across transformers into a high-voltage transmission grid that delivers power to the distribution system through grid transformers and distribution transformers until they reach consumers [4]. However, in recent years there has been a parallel development that was characterized by connecting small capacity generating units directly to the distribution

networks, and it was called the distributed generation (DG) units, and therefore power generation is no longer limited to the beginning of transmission lines, but also at the distribution areas, due to the presence of small capacity-controlled generating units. It is carried out according to smart systems to operate optimally to control the amount of generated capacity, store it and feed the loads at the lowest possible cost. This is the basis on which the smart electrical grid is built. In the present world, RES-based DG technology is gaining popularity to generate electric power. This is because of the fact that a variety of dispersed energy can be used here [5]. DG technology offers numerous technical, environmental, and economical benefits [6] [7] such as :

1- Reliable and effective power supply with higher energy efficiency;
2- Low transmission and distribution losses with flexible installation;
3- Less environmental pollution, and low operating costs;
4- Reducing dependence on central generating stations;
5- Involve individuals as an essential part of the grid as consumers and as suppliers of energy.

The new DG based electrical grid, also called microgrid (MG), can deliver electricity from suppliers to customers and to manage appliances at consumers' homes to avoid wasting energy, therefore reducing costs and increasing independency and transparency [8].

However, the deployment of distirbuted generation sysetm has many challenges, which might complicate the control structure. So it is imperative to know the control difficulties in order to warranty both quality of supply and ensuring power management supervising critical and non-critical loads. Some key power system concepts based on power versus frequency droops methodology, voltage control, and hierarchical control levels can be applied to improve system stability, enhance active and reactive support, ride through capability, among others [9].

The control and power management of an islanded AC microgrid formed by two DG units connected in parallel is the main idea addressed in this work. To achieve this goal, the following points are performed:

- Ensuring power sharing by managing the microgrid units using droop control.
- Eliminating circulation current induced by connecting inverters in parallel using the virtual impedance concept.
- Enhancing power quality by controlling the voltage and current by using linear quadratic regulator approach.

In order to fulfill the aforementioned objectives, the present manuscript is structured in four chapters. The main content of each chapter is briefly described below:

In the first chapter of this thesis, the concept of microgrid will be clarified and details about its structure, components and working states will be given. The second part of the chapter will be devoted to the mathematical model of a distributed generation unit made up of a three-phase voltage source feeding a three-phase load through an LC filter.

In the second chapter, the control methods of an islanded microgrid will be discussed. Several control techniques were applied in the literature; among them, the classic PI-based droop control is the most seen for such systems. In this regard, this chapter will present a detailed study of the voltage and current control of two parallel inverters operating as part of an islanded microgrid.

The mathematical theory of LQR controller will be detailed in the first part of the third chapter. In its second part, the closed-loop stability will be analyzed and verified, and then a simulation will be performed on Simulink to verify the effectiveness of the proposed LQR and compare its performance with that of classical PI controller.

In fourth chapter, PIL simulation using STM32F4 discovery board of LQR control of two parallel VSIs forming an islanded microgrid is performed. First, general description of the discovery board and its most prominent features will be given, and then the various stages

of PIL simulation will be detailed. Finally, LQR control of the proposed parallel system will be validated and commented on.

This manuscript will be ended by a general conclusion summarizing the most important findings and providing suggestions for further work.

Chapter I

Modeling of a Three-Phase Inverter Unit Based Islanded Microgrid

I.1 Introduction

In this chapter, an overview of different structures of power generation will be given. Firstly, a focus will be placed on the centralized generation and the challenging issues related to the use of this type of structure before moving to the detailed study of the distributed generation system. This chapter also introduces the importance of keeping up with the new and growing trend in power structure, which is towards using distributed generation systems. As we will focus in this thesis on the autonomous microgrid, it is worth to present the mathematical model of the three-phase voltage source interfacing three-phase loads through an LC-filter. Since this study tends to enhance power quality, employing space vector pulse width modulation (SVPWM) strategy to control the inverter switches is the best choice; hence, SVPWM is well discussed.

I.2 Centralized Generation

In last years, the electricity consumption has significantly grown due to the increase in the integration of new loads. To fulfill this demand, for long large power plants have been deployed and used as a proposed solution. These power plants are usually based on fossil and nuclear energy, which can produce large amounts of electricity to cover both power demand and losses in power transmission lines. Thanks to its size, these power plants allow to support the expansion of the grid to supply and connect more loads via complex lines with guaranteeing the continuity of electricity at all times, everywhere in the grid [10].

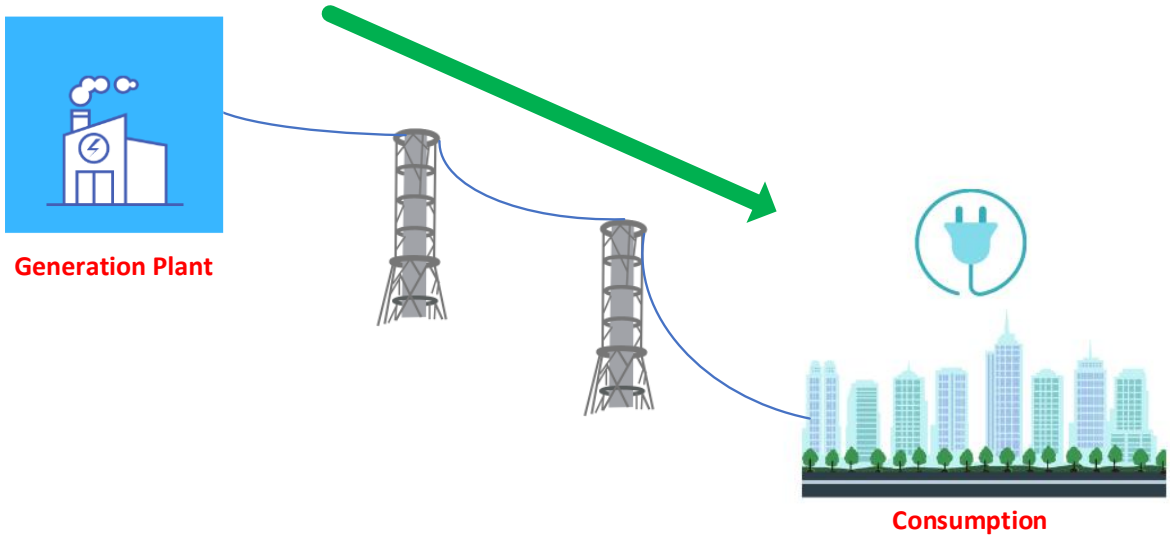

Fig. I.1. Simplified configuration of a centralized generation network

Twenty years ago, the global policy resides in centralizing the energy production, which led to the current paradigm of centralized generation as illustrated in Fig. (I.1). This type of generation aims to take the production plants away outside cities in order to reduce water and air pollution in urban areas.

Despite the advantages offered by centralized generation, this structure has many challenges at technical, economic, environmental and social levels [11].

I.2.1. Economic Challenges

The centralized generation faces many challenges at the economic level, including [12]:

- The reduction in production and energy transmission costs in order to offer consumers competitive tariffs while meeting the most stringent power quality requirements and reliability of the power supply;
- The dependency of these production systems on fossil resources impacts the production cost, which is greatly influenced by diversity of their prices. Prices that fluctuate daily and keep rising constantly due to its dislocation and the difficulties associated with its extraction;

- The relative availability of these resources encourage the price volatility in international markets;
- The cost of power plants facilities is still very high.

I.2.2. Environmental Impact

The environment impact of centralized power generation is significant due to the use of fuel and gas and other source of unclean energy. The electricity sector is responsible for emission of toxic particles, which leads to cause damage to the environment. Also, the use of nuclear plants produces radioactive waste of high range of danger.

All these economic challenges and environmental problems facing the power generation plants have hastened to find alternatives that are more reliable and less expensive, taking into account that they are environmentally friendly. All this and that made us think about the distributed generation.

I.3. Distributed Generation

Distributed generation is a new concept that is emerged to solve some problems that arise in centralized generation systems by offering a new structure to meet the energy demand. Distributed generation systems are designed to guarantee the reliability of the power supply and the quality of service for a limited number of consumers. Distributed generation has contributed to the emergency of new grid configurations, including microgrid and smartgrid [13]. These networks are composed of different distributed generation devices (photovoltaic panels, wind turbines, diesel generators, ...), of storage devices, as well as control system, supervision and energy management systems [14]. The concept of these microgrids is shown in Fig. (I.2). They have the advantage of operating in connected mode to the main network, or in an isolated mode. The isolated mode allows the microgrid to support the needs of locally installed loads, while the connected mode intervenes to support the global network by injecting part or all of the power produced into it [15].

I.4. Microgrid Definition

A microgrid is defined as an energy system, as shown in Fig. (I.2); it is composed of several distributed generation units, which allows the integration of a large proportion of energy sources mainly of renewable nature (wind, photovoltaic, biomass, hydraulics, etc.) associated with storage elements. The configuration of microgrids offers a significant gain in terms of efficiency and reliability thanks to the decentralization and parallel implementation of several distributed generation units [16]. Indeed, the power demanded by the loads is shared between different generation units, which contributes in improving reliability and efficiency of these systems. Each generation unit is made up of a static electrical energy conversion interface based on power electronics as well as an output low-pass filter for the suppression of high-frequency harmonics. However, microgrids face very significant challenges, including maintaining the balance between production and consumption in the presence of intermittent energy sources and uncertain loads [17].

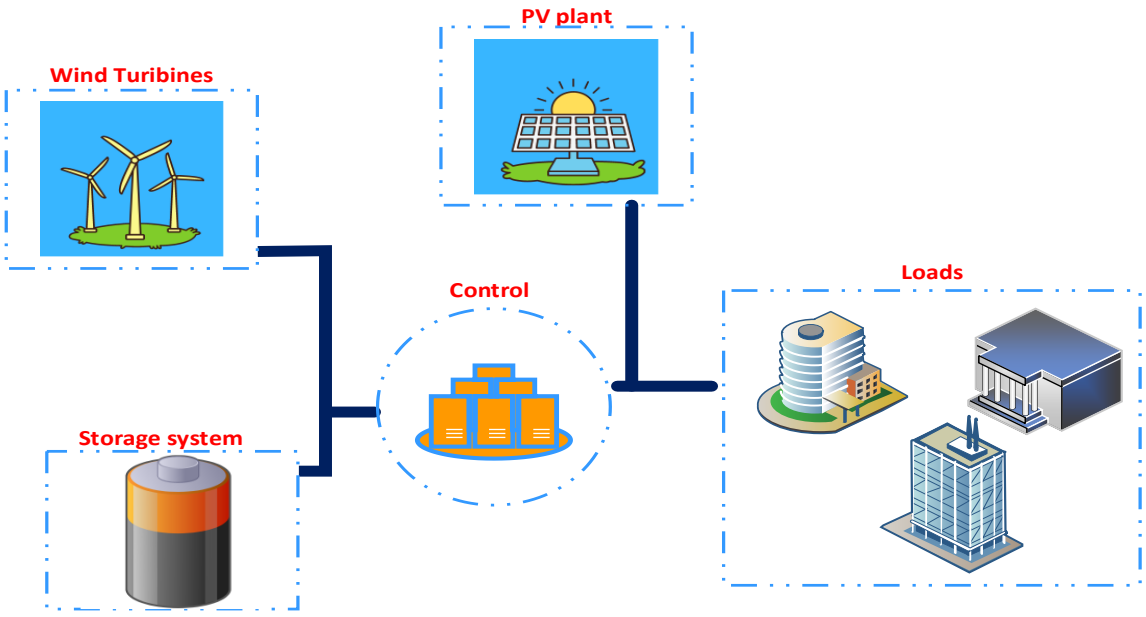

Fig. I.2. Typical diagram of a micro-grid

I.5. Micro Grid Operation Modes

Microgrid can operate either in grid connected or in islanded mode [18]. This is due to the possibility of using VSI in Voltage Controlled Mode (VSM) or Current Controlled Mode (CCM) [19],[20],[21]. In the following, the features of both operating modes are described.

1.5.1 Grid-Connected Mode

When the microgrid is in grid-connected mode, it can either import energy from the main grid or export power to the main grid to control the active and reactive power flow and to supervise the energy storage [22],[23].

Depending on the demand, the main grid and the local DGs might send power to the loads. If an event in the main grid occurs, an islanded operation mode might be implemented. The MG islanding process might be resulted from an intentional disconnection from the main grid such as maintenance needs or from a wanted and forced disconnection when a fault occurs in the main network such as voltage dips [24].

I.5.2. Islanded Operation Mode

It is said that a microgrid is in islanded mode when it is not connected to the main grid [25]. A microgrid operating in islanded mode can be advantageous in different scenarios. One of them is in rural places where it is difficult either to reach it or to install line of network distribution due to the high cost. Hence, in this case the best key solution is to give access to electricity to consumers via a microgrid operating in islanded mode.

Another possible scenario when a grid fault occurs, the microgrid is disconnected from the grid to ensure the continuity of supplying and powering the local loads and protecting the distributed generators and storage systems. Therefore, the grid reliability is improved as well as its capability of reducing the number if consumers that experience the voltage outage. It is worth noting that this operation is done when the grid is suitable to guarantee the power quality needed by loads.

The microgrid in islanded mode has to be carried out the same duties as the main grid carries:

- Voltage and frequency control: the accepted voltage deviation from its nominal value is $\pm 5\%$, and the accepted one for the frequency should be $\pm 2\%$;
- Power balance: this is to say that the amount of power produced by distributed energy resources must match the power needed by the loads. If there is an overproduction, energy storage systems can be a good choice. However, if there is an underproduction, the voltage drops causing power outage and blackout [26];
- Power quality: the Total Harmonic Distortion (THD) should be lesser than 5%, except this the microgrid may not be in a proper operation and the loads will be malfunctioning [16].

The above requirements will be ensured by making the inverter interfacing the microgrid operating in voltage-controlled mode. In this thesis, a special attention will be given to the islanded mode in which an LC filter is used to interface the loads. In next two sections, the control paradigm and the modeling of power converter with LC filter used in microgrid will presented.

I.6 Architecture of an AC Islanded Microgrid

A microgrid is designed by putting in parallel one or many distributed generators (DGs) with loads. Paralleling DGs allows efficiently responding to increasing demand of energy, also allowing securing the energy supply in case of perturbation or failure by reducing the dependency of these architectures vis-a-vis DGs units. Its construction is varied according to the need and constraints related to the application; these following elements are often observed [27]:

- Storage system, diesel generators, renewable energy sources (RESs);
- Power electronics converters (essentially, we find inverter controlled in voltage source);

- Filtering devices and interconnection lines;
- Electrical loads.

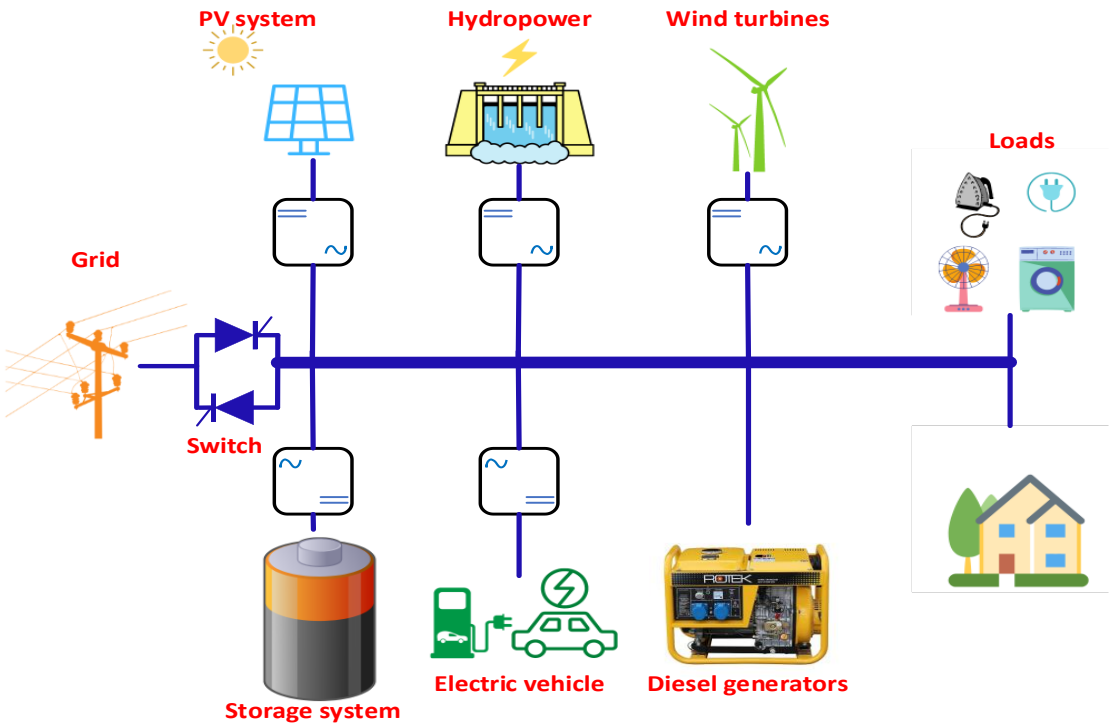

Fig. I.3.Typical configuration of autonomous microgrid

The operation of autonomous microgrid consists of paralleling many distributed generators to guarantee the continuity of the service and also to ensure the stability of the system and its robustness facing perturbations. For that, each DG unit has to be governed by two control stages, which are voltage regulation and current control. Whereas the control strategy employed in microgrid follows, in general, a hierarchic structure as depicted in Fig. (I.4).

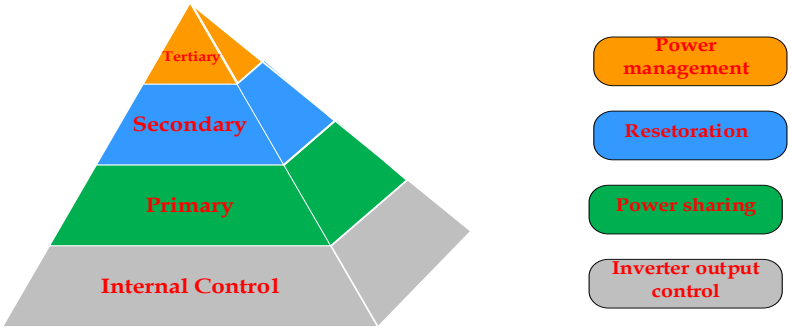

Fig. I.4. Hierarchical levels of a flexible microgrid operation modes

I.6.1 Internal Control

This control layer is the lower level of this architecture containing the inverter output control. It consists of regulating the output voltage and the current while keeping the system stable [28].

I.6.2 Primary Control

This level of control is dedicated to the management of load distribution and flow of active and reactive powers between the various distributed units. Usually, the droop control method is adopted to emulate the physical behavior in order to share power and make the system stable. It includes virtual impedance to imitate the physical output impedance [29].

I.6.3 Secondary Control

Secondary control is intended to provide restoration of frequency and amplitude voltage to their nominal values. Indeed, when applying the primary control to properly share the powers, frequency and amplitude of the reference voltages of each generation unit will vary according to the droop laws. These variations generate a deviation of the operating point of the system from its nominal position and may exceed the allowable margins established by international standards, i.e. a margin of 2% for the frequency and a margin of 5% for the voltage amplitude (Standard NF EN 50160). The secondary control acts to restore the frequency and the amplitude to nominal values using the information collected by means of communication links between the different distributed generation units [30].

I.6.4 Tertiary Control

This control layer is the highest level in the control hierarchy and it is generally designed to optimize the energy flows between the different MGs or between a microgrid and the main grid. Tertiary control facilitates the planning of exploitation of the power flow and management of the purchase and sale of energy [31].

I.7. Microgrid Design and Modeling

Generally, in autonomous microgrid a distributed generator is connected to an inverter in series with an LC-filter [32] in order to interface it to the loads as shown in Fig. (I.5). In literature, there are many developed modulation techniques used to generate switching signals for the inverter unit. Mostly, space vector pulse width modulation (SVPWM) is used to improve the output quality and enhance efficiency. In next sections, a brief about DC-bus sizing, LC filter design, inverter modeling, and SVPWM detail will be given.

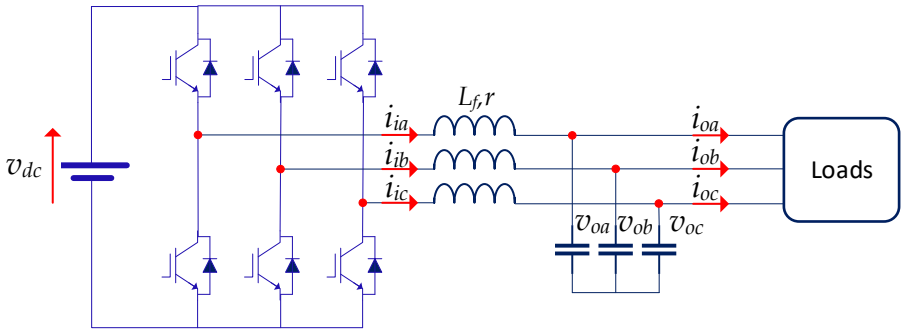

Fig. I.5. Basic schematic diagram of a power stage of a three-phase inverter in autonomous microgrid

I.8. Microgrid Design

I.8.1. DC-Bus Voltage Choice

The DC-bus voltage is the main parameter that has to be selected. Indeed, if the level of the DC voltage is low it can be considered one of limits that limit either the grid connected operation or the maintaining of the unity power factor requirement [33]. For this reason, the lowest level of DC-bus voltage should be [34].

$$v_{dc} > \sqrt{3}\sqrt{2}v_{rms} \quad \text{(I.1)}$$

Where v_{rms} is the root-mean-square (rms) voltage

According to (I.1), v_{dc} can be calculated as follows:

For $v_{rms} = \frac{400}{\sqrt{2}} = 282.85$ V, $v_{dc} > 693$ V

The value of v_{dc} should be chosen greater than 693 V to take in consideration voltage transients.

I.8.2. LC Filter Design

LC filter ensures harmonics attenuation related to the output voltage caused by switching process. Fig. (I.6) presents a single-phase equivalent circuit of the LC filter.

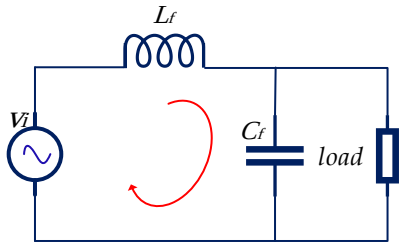

Fig. I.6. Single phase equivalent circuit of the LC-filtered VSI

I.8.2.1 Ripple Analysis and Inverter-Side Inductance Design

The inverter-side inductance is designed in order to limit the ripple of the inverter-side current. The equation (I.2) is used to determine the value of inductance for a specified peak-to-peak inductor current for continuous-current operation [35] [36].

$$\frac{L_f \Delta i}{(1-m)T_{sw}} = \frac{2}{3} m v_{dc} \tag{I.2}$$

where (m) is the inverter modulation factor, and T_{sw} is the switching period. The value of (m) takes (0.5) at the maximum peak to peak current ripple, hence

$$\Delta i_{\max} = \frac{v_{dc}}{6 f_{sw} L_f} \tag{I.3}$$

where L_f is the inverter side inductor and its value should be equal or superior to $\frac{v_{dc}}{6 f_{sw} \Delta i_{\max}}$ where $f_{sw} = \frac{1}{T_{sw}}$ is the switching frequency.

To find the value of the inductance, the maximum peak to peak current ripple is calculated using the following equation:

For *R=5 Ω* and for single phase full bridge inverter $V_{rms} = v_{dc} = 1000V$

We find $I_{rms} = 200A$

$\Delta i_{\max} = 20\%$ of rated current $\Delta i_{\max} = 40A$

For f_{sw} =1 KHz , L_f should be:

$L_f \geq \frac{v_{dc}}{6 f_{sw} \Delta i_{\max}}$,we find $L_f \geq 294\ \mu H$

I.8.2.2 Filter Capacitance Design

The system of equations that modeled the LC filter is:

$$(sL_f + r)i = v_i - v_o \tag{I.4}$$

$$(sC_f)v_o = i - i_o \tag{I.5}$$

With some substitutions, the output voltage is expressed as:

$$v_o = \frac{v_i - i_o(sL_f + r)}{L_f C_f s^2 + rC_f s + 1} \tag{I.6}$$

So, the transfer function $\frac{v_o}{v_i}$ can be obtained as:

$$\frac{v_o}{v_i} = \frac{1}{L_f C_f s^2 + rC_f s + 1} \tag{I.7}$$

Considering that filter resistance is neglected, the resonance frequency at maximum amplitude of this transfer function can be obtained as:

$$f_{res} = \frac{1}{2\pi\sqrt{L_f C_f}} \tag{I.8}$$

To avoid the resonance frequency and ensure the stability of the system, the resonance frequency should be designed considering the criterion below [37]:

$$10f_{fun} < f_{res} < 0.5f_{sw} \tag{I.9}$$

Where f_{fun} is the fundamental frequency ,and f_{sw} is the switching frequency

According to [38], the reactive power should be 5% of the rated apparent power (S), which results in:

$$Q = \frac{v_{rms}^2}{1/2\pi f_{fun} C_f} = 5\% \times S$$

The capacitance is expressed by:

$$C_f = \frac{0.05S}{v_{rms}^2 2\pi f_{fun}}$$

The value of the capacitance is calculated by:

$$C_f = \frac{0.05s}{v_{rms}^2 \pi f_{fun}} = \frac{0.05 \times 32000}{282.85^2 \times 3.14 \times 50} = 127.38\ \mu F$$

C_f should be $C_f \geq 127.38 \mu F$

I.9. Inverter Modeling

Six switches on three legs are needed to form a three-phase two-level inverter. The switches must have antiparallel diodes to provide return paths for currents when voltage and current waveforms are not in phase. Shoot-through must be avoided, which means the two switches in each leg must not be in on-state at the same time. Therefore, a dead-time must be implemented to avoid any DC-bus shoot-through in VSI [39].

The two-level VSI, shown in Fig. (I.7), operates based on the turn ON/OFF of the switching elements depending on the state of the control signals (s_1, s_2, s_3) that are issued from SVPWM strategy.

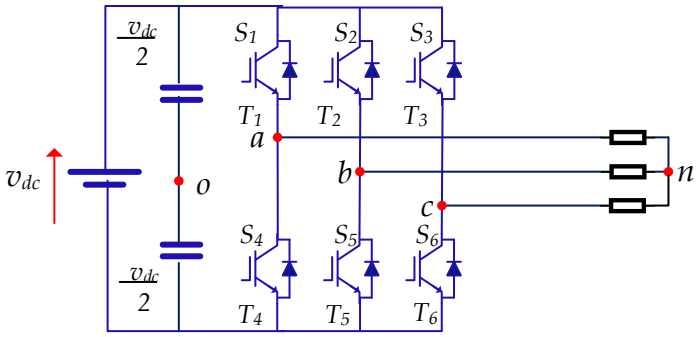

Fig. I.7. Three-phase inverter circuit diagram

Each switching function is defined by:

$$S_i = \begin{cases} 1 & \text{when } T_i \text{ is ON and } T_{i+3} \text{ is OFF} \\ 0 & \text{when } T_i \text{ is OFF and } T_{i+3} \text{ is ON} \end{cases} \quad \text{(I.10)}$$

The potentials of the nodes a, b, and c of the converter with respect to the imaginary midpoint *O* are given by the equation (I.11).

$$\begin{cases} v_{ao} = \frac{v_{dc}}{2}(2S_1 - 1) \\ v_{bo} = \frac{v_{dc}}{2}(2S_2 - 1) \\ v_{co} = \frac{v_{dc}}{2}(2S_3 - 1) \end{cases} \quad \text{(I.11)}$$

The line to line voltages are given by:

$$\begin{cases} u_{ab} = v_{ao} - v_{bo} = \frac{v_{dc}}{2}(2S_1 - 1) - \frac{v_{dc}}{2}(2S_2 - 1) = v_{dc}(S_1 - S_2) \\ u_{bc} = v_{bo} - v_{co} = \frac{v_{dc}}{2}(2S_2 - 1) - \frac{v_{dc}}{2}(2S_3 - 1) = v_{dc}(S_2 - S_1) \\ u_{ca} = v_{co} - v_{ao} = \frac{v_{dc}}{2}(2S_3 - 1) - \frac{v_{dc}}{2}(2S_1 - 1) = v_{dc}(S_3 - S_1) \end{cases} \quad \text{(I.12)}$$

The phase voltages with respect to the neutral point (n) on the side of the AC load can be obtained by:

$$\begin{cases} v_{an} = v_{ao} - v_{no} \\ v_{bn} = v_{bo} - v_{no} \\ v_{cn} = v_{co} - v_{no} \end{cases} \quad \text{(I.13)}$$

In a balanced three-phase system, we have:

$$v_{an} + v_{bn} + v_{cn} = 0 \quad \text{(I.14)}$$

By summing v_{ao} andv_{bo} andv_{co} the following equation is obtained.

$$v_{no} = \frac{1}{3}(v_{ao} + v_{bo} + v_{co}) \quad \text{(I.15)}$$

The inverter three output voltages v_{an} and v_{bn} and v_{cn} can be expressed as:

$$\begin{cases} v_{an} = v_{ao} - v_{no} = v_{ao} - \frac{1}{3}(v_{ao} + v_{bo} + v_{co}) = \frac{2}{3}v_{ao} - \frac{1}{3}v_{bo} - \frac{1}{3}v_{co} \\ v_{bn} = v_{bo} - v_{no} = v_{bo} - \frac{1}{3}(v_{ao} + v_{bo} + v_{co}) = -\frac{1}{3}v_{ao} + \frac{2}{3}v_{bo} - \frac{1}{3}v_{co} \\ v_{cn} = v_{co} - v_{no} = v_{co} - \frac{1}{3}(v_{ao} + v_{bo} + v_{co}) = -\frac{1}{3}v_{ao} - \frac{1}{3}v_{bo} + \frac{2}{3}v_{co} \end{cases} \quad \text{(I.16)}$$

From (I.11) and (I.16), the phase voltages of the inverter can be written as function of the states (S_1, S_2, S_3), and DC-link voltage as follows:

$$\begin{cases} v_{an} = \frac{2}{3}\frac{v_{dc}}{2}(2S_1 - 1) - \frac{1}{3}\frac{v_{dc}}{2}(2S_2 - 1) - \frac{1}{3}\frac{v_{dc}}{2}(2S_3 - 1) \\ v_{bn} = -\frac{1}{3}\frac{v_{dc}}{2}(2S_1 - 1) + \frac{2}{3}\frac{v_{dc}}{2}(2S_2 - 1) - \frac{1}{3}\frac{v_{dc}}{2}(2S_3 - 1) \\ v_{cn} = -\frac{1}{3}\frac{v_{dc}}{2}(2S_1 - 1) - \frac{1}{3}\frac{v_{dc}}{2}(2S_2 - 1) + \frac{2}{3}\frac{v_{dc}}{2}(2S_3 - 1) \end{cases} \quad \text{(I.17)}$$

By simplifying equation (1.17), it results:

$$\begin{cases} v_{an} = \frac{v_{dc}}{3}(2S_1 - S_2 - S_3) \\ v_{bn} = \frac{v_{dc}}{3}(-S_1 + 2S_2 - S_3) \\ v_{cn} = \frac{v_{dc}}{3}(-S_1 - S_2 + 2S_3) \end{cases} \quad \text{(I.18)}$$

By expressing (I.18) in a matrix form, the VSI conversion matrix is defined by the following equation:

$$\begin{bmatrix} v_{an} \\ v_{bn} \\ v_{cn} \end{bmatrix} = \frac{v_{dc}}{3} \begin{bmatrix} 2 & -1 & -1 \\ -1 & 2 & -1 \\ -1 & -1 & 2 \end{bmatrix} \begin{bmatrix} S_1 \\ S_2 \\ S_3 \end{bmatrix} \quad \text{(I.19)}$$

I.10. Mathematical Model of the LC Filter

I.10.1. Model in Natural Frame

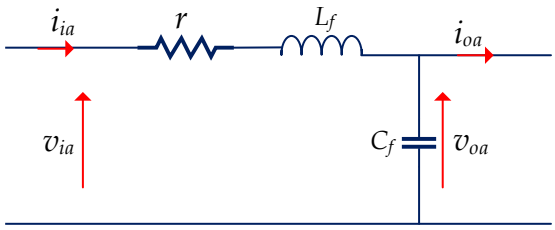

Fig. I.8. Per-phase equivalent circuit for LC filter

By applying Kirchhoff's current and voltage laws respectively on Fig. (I.8), the following current and voltage equations are derived:

$$C_f \frac{dv_{oabc}}{dt} = i_{iabc} - i_{oabc} \quad \text{(I.20)}$$

$$L_f \frac{dv_{iabc}}{dt} = v_{iabc} - ri_{iabc} - v_{oabc} \quad \text{(I.21)}$$

From (I.20), the differential equations of the three-phase filter output voltages are:

$$\frac{dv_{oabc}}{dt} = \frac{1}{C_f} i_{iabc} - \frac{1}{C_f} i_{oabc} \quad \text{(I.22)}$$

From (I.21), the differential equations of the three-phase filter output currents are:

$$\frac{di_{iabc}}{dt} = \frac{1}{L_f} v_{iabc} - \frac{r}{L_f} i_{iabc} - \frac{1}{L_f} v_{oabc} \tag{I.23}$$

The equations (I.22), (I.23) can be expressed as the following state space model in *abc* system.

$$\frac{d}{dt}\begin{bmatrix} v_{oa} \\ v_{ob} \\ v_{oc} \end{bmatrix} = \begin{bmatrix} 0 & 0 & 0 \\ 0 & 0 & 0 \\ 0 & 0 & 0 \end{bmatrix} \begin{bmatrix} v_{oa} \\ v_{ob} \\ v_{oc} \end{bmatrix} + \begin{bmatrix} \frac{1}{C_f} & 0 & 0 \\ 0 & \frac{1}{C_f} & 0 \\ 0 & 0 & \frac{1}{C_f} \end{bmatrix} \begin{bmatrix} i_{oa} \\ i_{ob} \\ i_{oc} \end{bmatrix} \tag{I.25}$$

$$\frac{d}{dt}\begin{bmatrix} i_{ia} \\ i_{ib} \\ i_{ic} \end{bmatrix} = \begin{bmatrix} \frac{-r}{L_f} & 0 & 0 \\ 0 & \frac{-r}{L_f} & 0 \\ 0 & 0 & \frac{-r}{L_f} \end{bmatrix} \begin{bmatrix} i_{ia} \\ i_{ib} \\ i_{ic} \end{bmatrix} + \begin{bmatrix} \frac{-1}{L_f} & 0 & 0 \\ 0 & \frac{-1}{L_f} & 0 \\ 0 & 0 & \frac{-1}{L_f} \end{bmatrix} \begin{bmatrix} v_{oa} \\ v_{ob} \\ v_{oc} \end{bmatrix} \tag{I.24}$$

The equations (I.24) and (I.25) can be combined as follows:

$$\frac{d}{dt}\begin{bmatrix} v_{oa} \\ v_{ob} \\ v_{oc} \\ i_{ia} \\ i_{ib} \\ i_{ic} \end{bmatrix} = \begin{bmatrix} 0 & 0 & 0 & \frac{1}{c_f} & 0 & 0 \\ 0 & 0 & 0 & 0 & \frac{1}{c_f} & 0 \\ 0 & 0 & 0 & 0 & 0 & \frac{1}{c_f} \\ -\frac{1}{L_f} & 0 & 0 & -\frac{r}{L_f} & 0 & 0 \\ 0 & -\frac{1}{L_f} & 0 & 0 & -\frac{r}{L_f} & 0 \\ 0 & 0 & -\frac{1}{L_f} & 0 & 0 & -\frac{r}{L_f} \end{bmatrix} \begin{bmatrix} v_{oa} \\ v_{ob} \\ v_{oc} \\ i_{ia} \\ i_{ib} \\ i_{ic} \end{bmatrix} + \begin{bmatrix} \frac{-1}{c_f} & 0 & 0 & 0 & 0 & 0 \\ 0 & \frac{-1}{c_f} & 0 & 0 & 0 & 0 \\ 0 & 0 & \frac{-1}{c_f} & 0 & 0 & 0 \\ 0 & 0 & 0 & \frac{1}{L_f} & 0 & 0 \\ 0 & 0 & 0 & 0 & \frac{1}{L_f} & 0 \\ 0 & 0 & 0 & 0 & 0 & \frac{1}{L_f} \end{bmatrix} \begin{bmatrix} i_{oa} \\ i_{ob} \\ i_{oc} \\ v_{ia} \\ v_{ib} \\ v_{ic} \end{bmatrix} \tag{I.26}$$

I.10.2. Model in $\alpha\beta$-Frame

In order to transform the LC filter model from *abc* frame to *αβo* frame, the following transformation is used:

$$x_{\alpha\beta o} = M x_{abc} \tag{I.27}$$

where M is the Clarke matrix transformation given by:

$$M = \frac{2}{3}\begin{bmatrix} 1 & -\frac{1}{2} & -\frac{1}{2} \\ 0 & \sqrt{\frac{3}{2}} & -\sqrt{\frac{3}{2}} \\ \frac{1}{2} & \frac{1}{2} & \frac{1}{2} \end{bmatrix} \tag{I.28}$$

Similarly, passing from *αβo* to *abc* needs the following transformation:

$$x_{abc} = M^{-1} v_{\alpha\beta o} \tag{I.29}$$

where M^{-1} is the inverse Clarke matrix transformation given by:

$$M^{-1} = \begin{bmatrix} 1 & 0 & \frac{1}{2} \\ -\frac{1}{2} & \sqrt{\frac{3}{2}} & \frac{1}{2} \\ -\frac{1}{2} & -\sqrt{\frac{3}{2}} & \frac{1}{2} \end{bmatrix} \tag{I.30}$$

By applying (I.30) on (I.22) and (I.23), it results:

$$\frac{d(M^{-1} v_{o\alpha\beta o})}{dt} = \frac{1}{C_f} M^{-1} i_{i\alpha\beta o} - \frac{1}{C_f} M^{-1} i_{o\alpha\beta o} \tag{I.31}$$

$$\frac{d(M^{-1} i_{i\alpha\beta o})}{dt} = \frac{1}{L_f} M^{-1} v_{o\alpha\beta o} - \frac{r}{L_f} M^{-1} i_{i\alpha\beta o} - \frac{1}{L_f} M^{-1} v_{i\alpha\beta o} \tag{I.32}$$

Multiply (I.31) and (I.32) by *M*:

$$M\frac{d(M^{-1}v_{o\alpha\beta o})}{dt}=MM^{-1}\frac{d(v_{o\alpha\beta o})}{dt}=\frac{1}{C_f}i_{i\alpha\beta o}-\frac{1}{C_f}i_{o\alpha\beta o} \tag{I.33}$$

$$M\frac{d(M^{-1}i_{i\alpha\beta o})}{dt}=MM^{-1}\frac{d(i_{i\alpha\beta o})}{dt}=\frac{1}{L_f}v_{o\alpha\beta o}-\frac{r}{L_f}i_{i\alpha\beta o}-\frac{1}{L_f}v_{i\alpha\beta o} \tag{I.34}$$

Finally, the model of the LC filter in *αβo* frame is given by:

$$\frac{d}{dt}\begin{bmatrix}v_{o\alpha}\\v_{o\beta}\\v_{oo}\end{bmatrix}=\frac{1}{C_f}\begin{bmatrix}i_{i\alpha}\\i_{i\beta}\\i_{io}\end{bmatrix}-\frac{1}{C_f}\begin{bmatrix}i_{o\alpha}\\i_{o\beta}\\i_{oo}\end{bmatrix} \tag{I.35}$$

$$\frac{d}{dt}\begin{bmatrix}i_{i\alpha}\\i_{i\beta}\\i_{io}\end{bmatrix}=\frac{1}{L_f}\begin{bmatrix}v_{i\alpha}\\v_{i\beta}\\v_{io}\end{bmatrix}-\frac{1}{L_f}\begin{bmatrix}v_{o\alpha}\\v_{o\beta}\\v_{oo}\end{bmatrix} \tag{I.36}$$

I.10.3. Model in *dq*-Frame

In the natural reference frame *abc* as well as in *αβo* frame, the phase quantities are sinusoidal. These variable quantities cannot be controlled easily using most traditional control methods designed to regulate direct quantities. However, if the referential frame is rotated synchronously at frequency f_{fun}, the phase quantities of the positive sequence become constant.

The model in *abc* system can be transformed to *dq0* system by the following transformation:

$$x_{abc}=T^{-1}x_{dqo} \tag{I.37}$$

where T, T^{-1} are Park matrix transformation and its inverse, respectively. The matrices are given by:

$$T=\frac{2}{3}\begin{bmatrix}\cos(\theta) & \cos(\theta-\frac{2\pi}{3}) & \cos(\theta+\frac{2\pi}{3})\\-\sin(\theta) & -\sin(\theta-\frac{2\pi}{3}) & -\sin(\theta+\frac{2\pi}{3})\\\frac{1}{2} & \frac{1}{2} & \frac{1}{2}\end{bmatrix} \tag{I.38}$$

$$T^{-1}=\begin{bmatrix} \cos(\theta) & -\sin(\theta) & \frac{1}{2} \\ \cos(\theta-\frac{2\pi}{3}) & -\sin(\theta-\frac{2\pi}{3}) & \frac{1}{2} \\ \cos(\theta+\frac{2\pi}{3}) & -\sin(\theta+\frac{2\pi}{3}) & \frac{1}{2} \end{bmatrix} \quad \text{(I.39)}$$

By applying (I.37, ((I.39) on (I.22) and (I.23), it results:

$$\frac{d(T^{-1}v_{odqo})}{dt}=\frac{1}{C_f}T^{-1}i_{idqo}-\frac{1}{C_f}T^{-1}i_{odqo} \quad \text{(I.40)}$$

$$\frac{d(T^{-1}i_{idqo})}{dt}=\frac{1}{L_f}T^{-1}v_{odqo}-\frac{r}{L_f}T^{-1}i_{idqo}-\frac{1}{L_f}T^{-1}v_{idqo} \quad \text{(I.41)}$$

Multiply (I.40) and (I.41) by T, it results:

$$T\frac{d(T^{-1}v_{odqo})}{dt}=T\frac{d(T^{-1})}{dt}v_{odqo}+TT^{-1}\frac{d(v_{odqo})}{dt}=\frac{1}{C_f}i_{idqo}-\frac{1}{C_f}i_{odqo} \quad \text{(I.42)}$$

$$T\frac{d(T^{-1}i_{idqo})}{dt}=T\frac{d(T^{-1})}{dt}i_{odqo}+TT^{-1}\frac{d(i_{odqo})}{dt}=\frac{1}{L_f}v_{odqo}-\frac{r}{L_f}i_{idqo}-\frac{1}{L_f}v_{idqo} \quad \text{(I.43)}$$

With:

$$T\frac{dT^{-1}}{dt}=\begin{bmatrix} 0 & -\omega & 0 \\ \omega & 0 & 0 \\ 0 & 0 & 0 \end{bmatrix}, \quad \omega=\frac{d\theta}{dt} \quad \text{(I.44)}$$

By substituting (I.44) into (I.42) and (I.43), it results:

$$\begin{bmatrix} 0 & -\omega & 0 \\ \omega & 0 & 0 \\ 0 & 0 & 0 \end{bmatrix}\begin{bmatrix} v_{od} \\ v_{oq} \\ v_{oo} \end{bmatrix}+\frac{d}{dt}\begin{bmatrix} v_{od} \\ v_{oq} \\ v_{oo} \end{bmatrix}=\frac{1}{C_f}\begin{bmatrix} i_{id} \\ i_{iq} \\ i_{io} \end{bmatrix}-\frac{1}{C_f}\begin{bmatrix} i_{od} \\ i_{oq} \\ i_{oo} \end{bmatrix} \quad \text{(I.45)}$$

$$\begin{bmatrix} 0 & -\omega & 0 \\ \omega & 0 & 0 \\ 0 & 0 & 0 \end{bmatrix}\begin{bmatrix} i_{id} \\ i_{iq} \\ i_{io} \end{bmatrix}+\frac{d}{dt}\begin{bmatrix} i_{id} \\ i_{iq} \\ i_{io} \end{bmatrix}=\frac{1}{L_f}\begin{bmatrix} V_{id} \\ V_{iq} \\ V_{io} \end{bmatrix}-\frac{r}{L_f}\begin{bmatrix} i_{id} \\ i_{iq} \\ i_{io} \end{bmatrix}-\frac{1}{L_f}\begin{bmatrix} v_{od} \\ v_{oq} \\ v_{oo} \end{bmatrix} \quad \text{(I.46)}$$

Finally, the state space model in *dq0* system is obtained as:

$$\frac{d}{dt}\begin{bmatrix} v_{od} \\ v_{oq} \\ v_{oo} \end{bmatrix} = \begin{bmatrix} 0 & -\omega & 0 \\ \omega & 0 & 0 \\ 0 & 0 & 0 \end{bmatrix}\begin{bmatrix} v_{od} \\ v_{oq} \\ v_{oo} \end{bmatrix} + \frac{1}{C_f}\begin{bmatrix} i_{id} \\ i_{iq} \\ i_{io} \end{bmatrix} - \frac{1}{C_f}\begin{bmatrix} i_{od} \\ i_{oq} \\ i_{oo} \end{bmatrix} \tag{I.47}$$

$$\frac{d}{dt}\begin{bmatrix} i_{id} \\ i_{iq} \\ i_{io} \end{bmatrix} = \begin{bmatrix} -\frac{r}{L_f} & -\omega & 0 \\ \omega & -\frac{r}{L_f} & 0 \\ 0 & 0 & -\frac{r}{L_f} \end{bmatrix}\begin{bmatrix} i_{id} \\ i_{iq} \\ i_{io} \end{bmatrix} + \frac{1}{L_f}\begin{bmatrix} v_{id} \\ v_{iq} \\ v_{io} \end{bmatrix} - \frac{1}{L_f}\begin{bmatrix} v_{od} \\ v_{oq} \\ v_{oo} \end{bmatrix} \tag{I.48}$$

I.11. Space-Vector Pulse-Width Modulation (SVPWM)

Space vector pulse width modulation (SVPWM) technique is widely used in inverter and rectifier controls [40],[41]. SVPWM is known to be suitable for digital implementation and can increase the obtainable maximum output voltage with maximum line voltage approaching 70.7% of the DC-link voltage (compared to 61.2% for SPWM) in the linear modulation range. Moreover, it can obtain a better voltage total harmonic distortion factor [42].

I.11.1 Principle of Space Vector PWM

SVPWM or simply Space vector modulation (SVM) is introduced based on the fact that there are only eight possible switching states for a three-phase inverter, as it is shown in Fig. (I.9). Among these, two states *(V_0, V_7)* correspond to a short circuit at the output, while the other six can be reasonable to establish space vectors in the *α-β* complex plane, as shown in Fig. (I.10); each space vector corresponds to a particular angular position. The magnitude of the vectors can be calculated from:

$V_{\max} = \frac{2}{3} v_{dc}$ where v_{dc} is the DC-bus voltage.

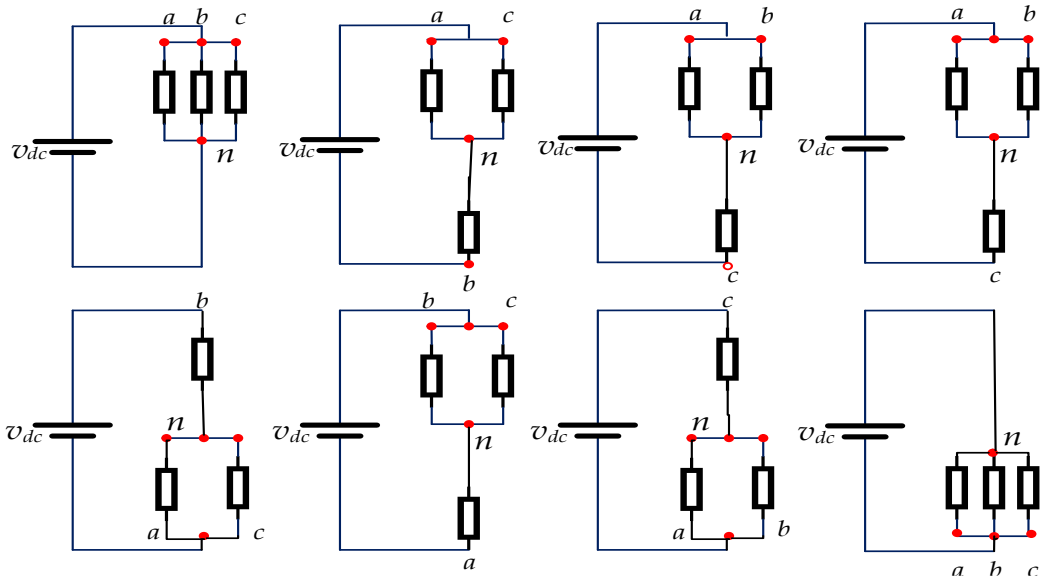

Fig. I.9. Possible switching states

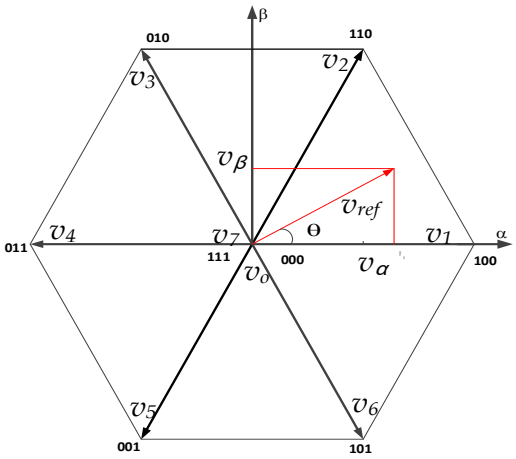

Fig. I.10. Converter voltage vectors diagram and reference voltage vector

Space vector during different existing switching states for S_1, S_2, S_3 are showed in the Table (I.1)

(S_1,S_2,S_3)	v_{an}	v_{bn}	v_{cn}	v_{ref}	*Vector*
000	0	0	0	0	$\vec{v}_0$
100	$\frac{2}{3}v_{dc}$	$-\frac{1}{3}v_{dc}$	$-\frac{1}{3}v_{dc}$	$\frac{2}{3}v_{dc}\angle 0^o$	$\vec{v}_1$
010	$-\frac{1}{3}v_{dc}$	$\frac{2}{3}v_{dc}$	$-\frac{1}{3}v_{dc}$	$\frac{2}{3}v_{dc}\angle 120^o$	$\vec{v}_3$

110	$\frac{1}{3}v_{dc}$	$\frac{1}{3}v_{dc}$	$-\frac{2}{3}v_{dc}$	$\frac{2}{3}v_{dc}\angle 60^{o}$	$\vec{v}_2$
001	$-\frac{1}{3}v_{dc}$	$-\frac{1}{3}v_{dc}$	$\frac{2}{3}v_{dc}$	$\frac{2}{3}v_{dc}\angle -120^{o}$	$\vec{v}_5$
101	$\frac{1}{3}v_{dc}$	$-\frac{2}{3}v_{dc}$	$\frac{1}{3}v_{dc}$	$\frac{2}{3}v_{dc}\angle -60^{o}$	$\vec{v}_6$
011	$-\frac{2}{3}v_{dc}$	$\frac{1}{3}v_{dc}$	$\frac{1}{3}v_{dc}$	$\frac{2}{3}v_{dc}\angle 180^{o}$	$\vec{v}_4$
111	0	0	0	0	$\vec{v}_7$

Table. I.1. Switching states and their phase voltages

I.11.2 Realization of Space Vector PWM

The SVM can be achieved by performing the following steps:

Step 1: Determination of the sector number

The reference voltage vector can be transformed in $\alpha\beta 0$ frame by applying Clarke transformation as follows:

$$\begin{bmatrix} v_{\alpha ref} \\ v_{\beta ref} \\ v_{oref} \end{bmatrix} = \begin{bmatrix} 1 & -\frac{1}{2} & -\frac{1}{2} \\ 0 & \sqrt{\frac{3}{2}} & -\sqrt{\frac{3}{2}} \\ \frac{1}{2} & \frac{1}{2} & \frac{1}{2} \end{bmatrix} \begin{bmatrix} v_{anref} \\ v_{bnref} \\ v_{cnref} \end{bmatrix} \tag{I.49}$$

The reference voltage space vector and its components in $\alpha\beta$ plane are shown in Fig. (I.11).

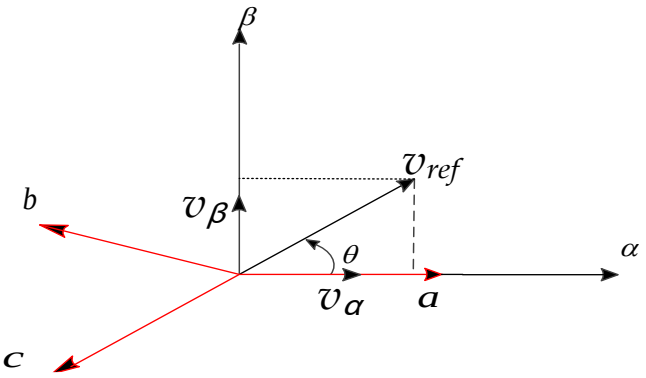

Fig. I.11. Reference voltage space vector and its components in (α, β) plane

The magnitude and the position of the reference voltage vector are determined from:

$$v_{ref} = \sqrt{v_{\alpha ref}{}^2 + v_{\beta ref}{}^2} \tag{I.50}$$

$$\theta = \tan^{-1}\left(\frac{v_{\beta ref}}{v_{\alpha ref}}\right) \tag{I.51}$$

Once the value of θ has been determined, the sector numbers are provided by:

$$i = ceil\left(\frac{3\theta}{\pi}\right) \in (1,2,3,4,5,6)$$

where *ceil* is a function that sets a given real number to an integer.

Step 2: Calculation of Time Duration

In the case where the reference vector is in the sector $i \in (1,2,3,4,5,6)$, the application duration of the adjacent vectors $\vec{v}_i$,$\vec{v}_{i+1}$ are denoted by t_i ,t_{i+1} and by t_o for the application duration of the null vectors. To ensure the equality of the average value of the voltage and its reference from an instant *t*, one must ensure that:

$$\frac{1}{T_s}\int_{t}^{t+T_s} \vec{v}_{ref}\,dt = \frac{1}{T_s}\left(\int_{t}^{t+t_1} \vec{v}_i dt + \int_{t+t_1}^{t+t_1+t_2} \vec{v}_{i+1} dt + \int_{t+t_1+t_2}^{t+T_s} \vec{v}_o dt\right) \tag{I.52}$$

Under very small sampling period T_s , the voltage $\vec{v}_{ref}$ is constant, the equation (I.52) can be simplified to:

$$\vec{v}_{ref} T_s = \vec{v}_1 t_1 + \vec{v}_2 t_2 + \vec{v}_O t_O \tag{I.53}$$

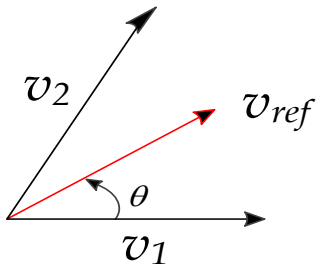

Fig. I.12. Reference vector as a combination of adjacent vectors in sector 1

From Fig. (I.12), the voltage vectors $\vec{v}_0, \vec{v}_1, \vec{v}_2$ and $\vec{v}_{ref}$ are defined by:

$$\vec{v}_{ref} = v_{ref} \angle \theta \tag{I.54}$$

$$\vec{v}_1 = \frac{2}{3} v_{dc} \angle 0^o \tag{I.55}$$

$$\vec{v}_2 = \frac{2}{3} v_{dc} \angle 60^o \tag{I.56}$$

By replacing (I.54), (I.55) and (I.56) in (I.53), it results:

$$(\vec{v}_{ref} \angle \theta) T_s = (\frac{2}{3} v_{dc} \angle 0^o) t_1 + (\frac{2}{3} v_{dc} \angle 60^o) t_2 + (0) t_0 \tag{I.57}$$

By equalizing the real and imaginary parts of this equality, we find:

$$v_{ref} \cos(\theta) T_s = \frac{2}{3} v_{dc} t_1 + \frac{1}{3} v_{dc} t_2 \tag{I.58}$$

$$v_{ref} \sin(\theta) T_s = \frac{1}{\sqrt{3}} v_{dc} t_2 \tag{I.59}$$

Furthermore, the vector application times must verify the following constraint.

$$t_1 + t_2 + t_0 = T_s \tag{I.60}$$

The application times of vectors $\vec{v}_1, \vec{v}_2, \vec{v}_0$ in the first sector are the solution of equations system (I.58), (I.59), and (I.60). These times are given by:

$$t_1 = \sqrt{3} T_s \frac{v_{ref}}{v_{dc}} \sin(60^o - \theta) \tag{I.61}$$

$$t_2 = \sqrt{3} T_s \frac{v_{ref}}{v_{dc}} \sin(\theta) \tag{I.62}$$

$$t_0 = T_s - t_1 - t_2 \tag{I.63}$$

For the other sectors, let define the following angle:

$$\theta' = \theta - 60^o\,(i\ -1) \tag{I.64}$$

Where i is the sector number.

The application times in any sector k are given by:

$$t_k = \sqrt{3}T_s \frac{v_{ref}}{v_{dc}} \sin(60^o - \theta') \tag{I.65}$$

$$t_{k+1} = \sqrt{3}T_s \frac{v_{ref}}{v_{dc}} \sin(\theta') \tag{I.66}$$

$$t_0 = T_s - t_k - t_{k+1} \tag{I.67}$$

Step 3: Pulses generation

The vectors to be implemented for different positions of the reference voltage vector are indicated in Fig. (I.12).

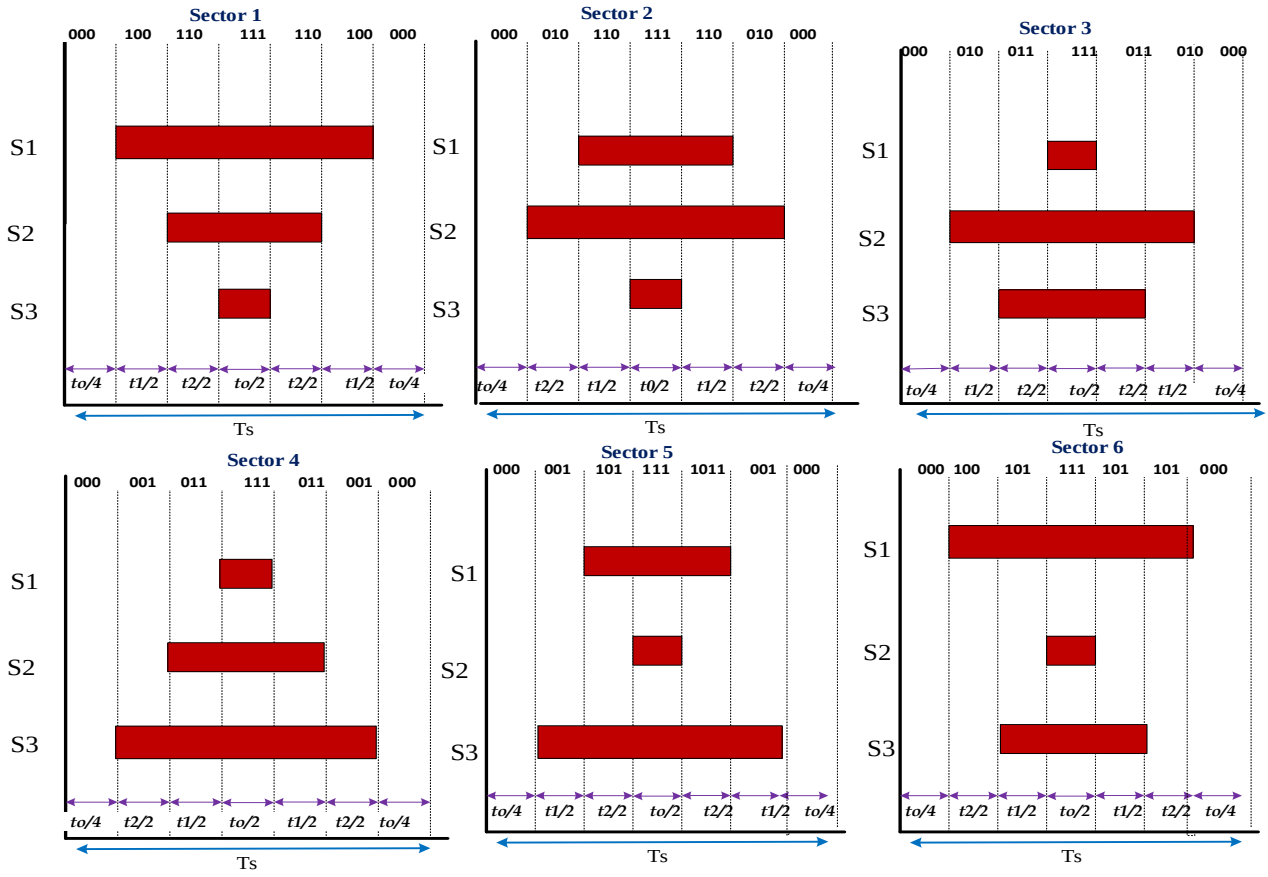

Fig. I.13. Distribution of voltage vectors to be applied in each sector

From Fig. (I.13), the ON-time means the switch is ON and OFF-time means the switch is OFF. The switching times are expressed as function of durations times in Table (I.2).

Sector	Switching ON Time	Switching OFF Time
1	$\begin{cases} t_{1ON} = t_1 + t_2 + \frac{t_0}{2} \\ t_{3ON} = t_2 + \frac{t_0}{2} \\ t_{5ON} = \frac{t_0}{2} \end{cases}$	$\begin{cases} t_{4OFF} = \frac{t_0}{2} \\ t_{6OFF} = t_1 + \frac{t_0}{2} \\ t_{2OFF} = t_1 + t_2 + \frac{t_0}{2} \end{cases}$
2	$\begin{cases} t_{1ON} = t_1 + \frac{t_0}{2} \\ t_{3ON} = t_1 + t_2 + \frac{t_0}{2} \\ t_{5ON} = \frac{t_0}{2} \end{cases}$	$\begin{cases} t_{4OFF} = t_2 + \frac{t_0}{2} \\ t_{6OFF} = \frac{t_0}{2} \\ t_{2OFF} = t_1 + t_2 + \frac{t_0}{2} \end{cases}$
3	$\begin{cases} t_{1ON} = \frac{t_0}{2} \\ t_{3ON} = t_1 + t_2 + \frac{t_0}{2} \\ t_{5ON} = t_2 + \frac{t_0}{2} \end{cases}$	$\begin{cases} t_{4OFF} = t_1 + t_2 + \frac{t_0}{2} \\ t_{6OFF} = \frac{t_0}{2} \\ t_{2OFF} = t_1 + \frac{t_0}{2} \end{cases}$
4	$\begin{cases} t_{1ON} = \frac{t_0}{2} \\ t_{3ON} = t_1 + \frac{t_0}{2} \\ t_{5ON} = t_1 + t_2 + \frac{t_0}{2} \end{cases}$	$\begin{cases} t_{4OFF} = t_1 + \frac{t_0}{2} \\ t_{6OFF} = t_1 + t_2 + \frac{t_0}{2} \\ t_{2OFF} = \frac{t_0}{2} \end{cases}$
5	$\begin{cases} t_{1ON} = t_2 + \frac{t_0}{2} \\ t_{3ON} = \frac{t_0}{2} \\ t_{5ON} = t_1 + t_2 + \frac{t_0}{2} \end{cases}$	$\begin{cases} t_{4OFF} = t_1 + t_2 + \frac{t_0}{2} \\ t_{6OFF} = t_2 + \frac{t_0}{2} \\ t_{2OFF} = \frac{t_0}{2} \end{cases}$

6	$\begin{cases} t_{1ON} = t_1 + t_2 + \frac{t_0}{2} \\ t_{3ON} = \frac{t_0}{2} \\ t_{5ON} = t_1 + \frac{t_0}{2} \end{cases}$	$\begin{cases} t_{4OFF} = \frac{t_0}{2} \\ t_{6OFF} = t_1 + t_2 + \frac{t_0}{2} \\ t_{2OFF} = t_2 + \frac{t_0}{2} \end{cases}$

Table I.2. Switching times as function of durations times

I.12. Conclusion

In this chapter, the centralized generation was first presented and the most important challenges it faces are highlighted. To overcome the centralized generation limitations, distributed generation was proposed and how it is one of the most important future ways to obtain higher efficiency and reliability is exhibited. Various definitions and control structures for the microgrid were also defined; including the microgrid hierarchical control and its operating modes. Finally, the detailed model of a single DG unit made up of an inverter connected to an LC filter is presented.

Chapter II

Droop Control of Parallel Inverters Based Islanded Microgrid

II.1. Introduction

Commonly, the microgrid control follows the hierarchical form with four levels. The levels zero and one are dedicated to control voltage and currents. The third level is devoted to the power sharing. Each unit of distributed generation DG has to be separately governed by these control levels. Hence, in each DG unit, the voltage should be regulated to take sinusoidal waveform with lesser THD. In literature, many control techniques have been applied. Amongst them, the classic PI based control is the most applied on such systems since it is considered as the best choice viewing to its simplicity. In this regard, this chapter will present detailed study of conventional control of two parallel inverters operating as part of an islanded microgird. In order to verify the performance of the PI facing disturbances, and system disparities, the control of two DG units using PI is simulated using Simulink.

II.2 Islanded Microgrid Topology

Fig. (II.1) illustrates the synoptic structure of an autonomous microgrid. It is composed of several distributed generators (DGs) units placed in parallel powering electric loads through LC-filter, in which every unit provides a part of the needed power.

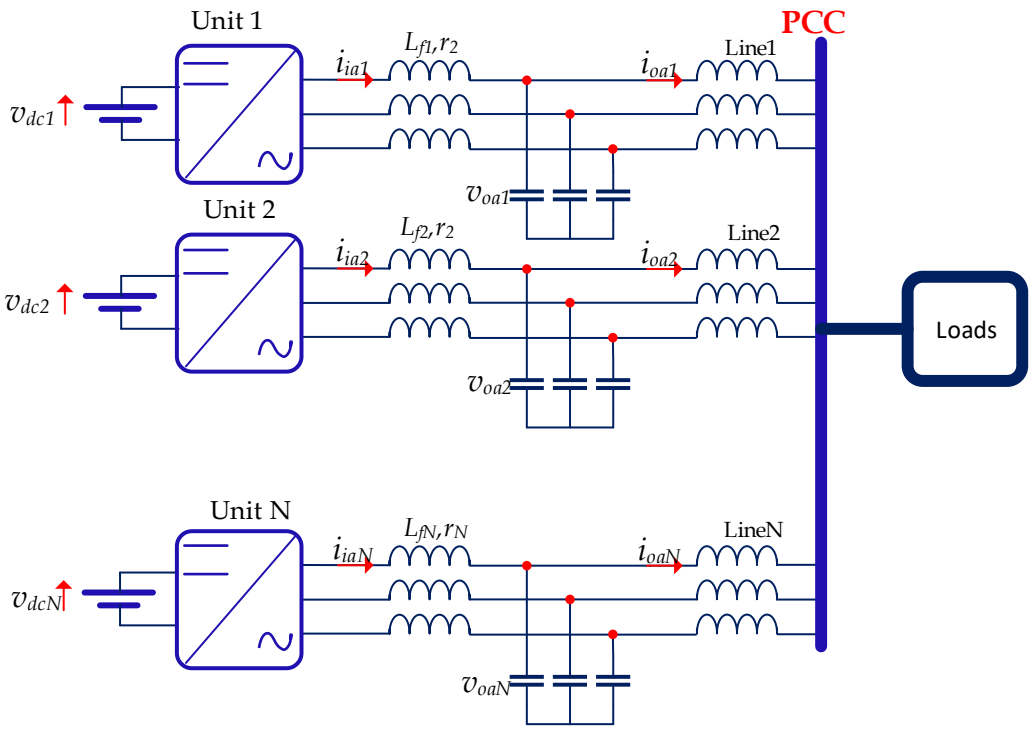

Fig. II.1. Islanded microgrid structure based on paralleled distributed generation units

Paralleling DGs allows increasing power capacity of the microgrid and also offers many advantages including [43]:

- Flexibility: because of modularity and distribution of different units; the microgrid can be easily re-configurated to include other new DGs or storage systems.
- Reliability: due to the availability of many DGs; the microgrid can ensure the continuity of the service in case of an expected failure.
- Efficiency: the power sharing amongst many units leads to reducing the size of components such as filters, which minimizes the power losses.

Due to the disparities in passive and active elements, employing such a system is risky and the system becomes unstable. Among many proposed solutions droop control is adopted to govern the power shared with the loads. Before moving to the detail of the power-sharing method, we should first introduce the lowest control level, which is dedicated to voltage and current regulation.

II.3. Voltage and Current Control

The control scheme, illustrated in Fig. (II.2), consists of an external voltage loop that provides the current reference and an internal current loop that provides the modulating signals; this type of control is referred as cascade control. This control approach is applied to each inverter unit among the cluster of autonomous microgrid [44].

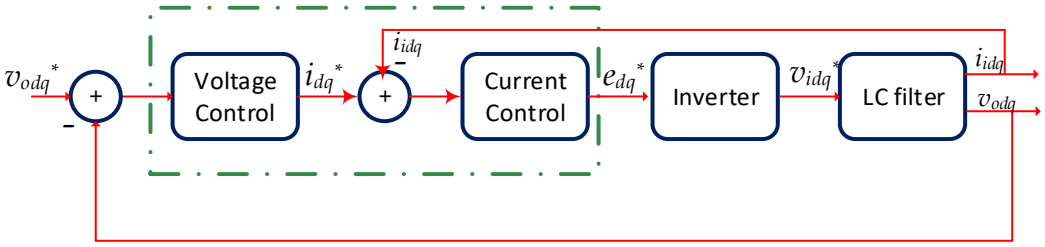

Fig. II.2 Cascade control scheme for an inverter unit

In this approach, the innermost loop has the fastest response and the higher bandwidth while the outer one is the slower one. In this chapter, the classic PI (proportional, integral) controller is chosen to regulate both voltage and current due to its simplicity and common use in industrial application [45].

II.2.1. Outer Voltage Controller

By applying Kirchhoff's current law to the LC filter, the following differential equations in three-phase frame can be established:

$$\begin{cases} C_f \dfrac{dv_{oa}}{dt} = i_{ia} - i_{oa} \\ C_f \dfrac{dv_{ob}}{dt} = i_{ib} - i_{ob} \\ C_f \dfrac{dv_{oc}}{dt} = i_{ic} - i_{oc} \end{cases} \quad \text{(II.1)}$$

By applying Clarke's transformation, the three equations (II.1) can be transformed in $\alpha\beta$-coordinate system as follows:

$$\begin{cases} C_f \dfrac{dv_{o\alpha}}{dt} = i_{i\alpha} - i_{o\alpha} \\ C_f \dfrac{dv_{o\beta}}{dt} = i_{i\beta} - i_{o\beta} \end{cases} \quad \text{(II.2)}$$

The above equation can be transformed from $\alpha\beta$-coordinate to dq-coordinate system resulting in:

$$\begin{cases} C_f \dfrac{dv_{od}}{dt} = i_{id} - i_{od} + C_f \omega v_{oq} \\ C_f \dfrac{dv_{oq}}{dt} = i_{iq} - i_{oq} - C_f \omega v_{od} \end{cases} \quad \text{(II.3)}$$

The equation (II.3) designates that the model of the VSI in the synchronous reference frame is a multiple input multiple-output, strongly coupled nonlinear system [46]. The transformed voltage equations of each axis have frequency induced term ($C_f \omega v_{oq}$ or $C_f \omega v_{od}$) that gives a cross coupling between the two axes. Thus, a close-loop voltage controller with decoupled voltage compensation and current feed-forward compensation is required to obtain a good control performance [47].

Fig. (II.3) shows the regulation of capacitor voltage loop by a PI controller.

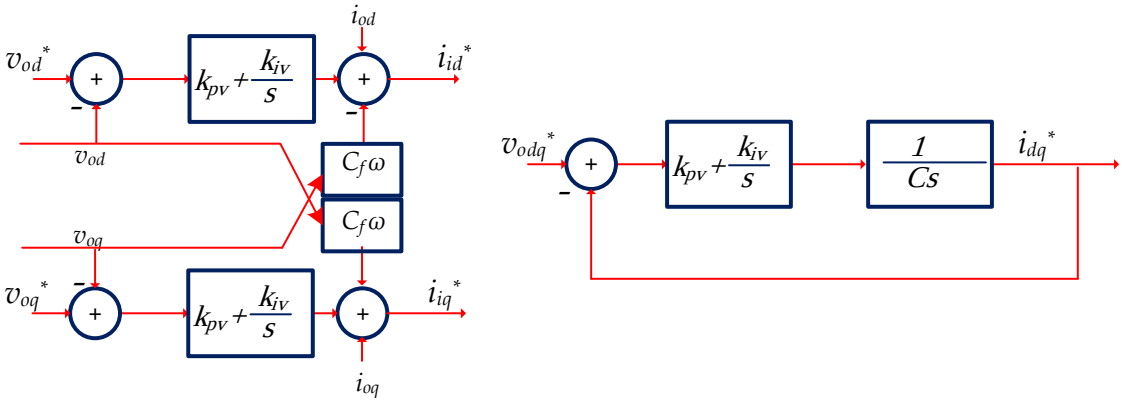

Fig. II.3. Outer capacitor voltage controller and voltage close loop control

The system closed-loop transfer function as presented in Fig.(II.4) is:

$$H(s) = \frac{1}{C_f} \frac{k_{pv}s + k_{iv}}{s^2 + \dfrac{k_{pv}}{C_f}s + \dfrac{k_{iv}}{C_f}} \quad \text{(II.4)}$$

The closed loop characteristic equation is compared to that of a desired second order system defined by:

$$G(s) = \frac{1}{s^2 + 2\xi\omega_n s + \omega_n{}^2} \tag{II.5}$$

The identification of the closed loop transfer function with that of a system of second order leads to:

$$\begin{aligned} k_{pv} &= 2\xi_v \omega_{nv} C_f \\ k_{iv} &= C_f \omega_{nv}{}^2 \end{aligned} \tag{II.6}$$

where ξ_v is the damping factor and ω_{nv} is the natural frequency.

II.2.2. Inner Current Controller

By applying Kirchhoff's voltage law on the LC-filter, the following differential equations for the three phases are obtained:

$$\begin{cases} L_f \dfrac{di_{ia}}{dt} = v_{ia} - v_{oa} - ri_{ia} \\ L_f \dfrac{di_{ib}}{dt} = v_{ib} - v_{ob} - ri_{ib} \\ L_f \dfrac{di_{ic}}{dt} = v_{ic} - v_{oc} - ri_{ic} \end{cases} \tag{II.7}$$

By applying Clarke's transformation, equations (II.7) can be written in the $\alpha\beta$-coordinate system as:

$$\begin{cases} L_f \dfrac{di_{i\alpha}}{dt} = v_{i\alpha} - v_{o\alpha} - ri_{i\alpha} \\ L_f \dfrac{di_{i\beta}}{dt} = v_{i\beta} - v_{o\beta} - ri_{i\beta} \end{cases} \tag{II.8}$$

By applying Park's transformation, equation (II.8) can be written in the dq-coordinate system as:

$$\begin{cases} L_f \dfrac{di_{id}}{dt} = v_{id} - v_{od} - L_f \omega i_{iq} - r i_{id} \\ L_f \dfrac{di_{iq}}{dt} = v_{iq} - i_{oq} + L_f \omega i_{id} - r i_{iq} \end{cases} \quad \text{(II.9)}$$

Fig (II.4) shows the regulation loop of the current by a PI controller.

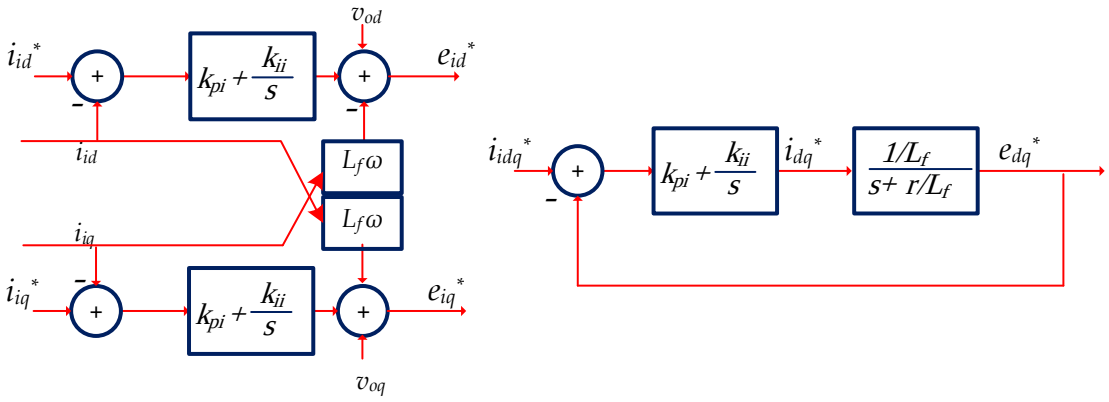

Fig. II.4. Inner current controller and current close loop control

The system closed-loop transfer function as presented in Fig.(II.4) is:

$$H(s) = \frac{1}{L_f} \frac{k_{pi} s + k_{ii}}{s^2 + \dfrac{k_{pi} + r}{L_f} s + \dfrac{k_{ii}}{L_f}} \quad \text{(II.10)}$$

By identifying the characteristic equation of the closed loop transfer function with the polynomial characteristic of a desired second order system, we find:

$$\begin{aligned} k_{pi} &= 2\xi_i \omega_{ni} L_f - r \\ k_{ii} &= L_f \omega_{ni}^2 \end{aligned} \quad \text{(II.11)}$$

where ξ_i is the damping factor and ω_{ni} is the natural frequency.

II.4. Droop Control and Output Impedance for DG Unit

Droop control strategy is the most used method for islanded mode control in order to share the total load demand to avoid DG overloads and to ensure stable operation of the microgrid. However, the output impedances of DG systems are generally different and

there exists a specific form of droop control adapted for each impedance, which can be resistive *(R)*, capacitive *(C)*, resistive capacitive *(RC)* or resistive-inductive *(RL)*. In the literature, it is reported that it is impossible to operate an inverter with inductive output in parallel with another inverter having a capacitive output [48]. In most cases, the output impedance is inductive *(L)* around the fundamental frequency. However, for a low-voltage microgrid, where the equivalent impedance between any two DG systems can be either resistive or inductive (with a DG coupling transformer or a grid side inductor), the impedance resistance *R* can no longer be neglected [49].

In the microgrid, each distributed generation unit is modeled by a Thévenin generator. A model composed of an ideal voltage source of amplitude *E* and internal angle ϕ in series with an output impedance *Z*. This output impedance includes the internal impedance of the generator, the impedance of the filter at the output as well as the line impedance ensuring the connection of each elementary DG unit to the microgrid common coupling point (PCC). Output voltages and currents of each distributed generator are denoted respectively by *V and I.*

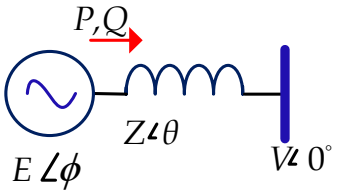

Fig. II.5. Equivalent of a DG unit connected to a common AC bus through an output impedance

From Fig. (II.5), it is easy to write:

$$\overline{V} = \overline{E} - \overline{Z}\,\overline{I} \qquad \text{(II.12)}$$

The determination of the expressions of the powers provided by each elementary DG to the loads locally installed on the PCC bus results from the expression of its complex apparent power given by:

$$\bar{S} = \bar{V}\,\bar{I}^{*} = P + jQ \tag{II.13}$$

From (II.12), the current is calculated by:

$$\bar{I} = \frac{\bar{E} - \bar{V}}{\bar{Z}} \tag{II.14}$$

By replacing the previous expression of the current in (II.13), it results:

$$\bar{S} = \bar{V}\left(\frac{\bar{E} - \bar{V}}{\bar{Z}}\right)^{*} \tag{II.15}$$

From Fig. (II.5) and using polar form of complex variables, the expression of complex apparent power can be rewritten as:

$$\bar{S} = V\left(\frac{Ee^{j\phi} - V}{Ze^{j\theta}}\right)^{*} = \frac{V}{Z}\left(\frac{Ee^{j\phi} - V}{e^{j\theta}}\right)^{*} \tag{II.16}$$

$$\begin{aligned}
\bar{S} &= \frac{V}{Z}\left(Ee^{j(\phi-\theta)} - Ve^{-j\theta}\right)^{*} = \frac{V}{Z}\left(E\cos(\phi-\theta) + jE\sin(\phi-\theta) - V\cos(-\theta) - jV\sin(-\theta)\right)^{*} \\
&= \frac{V}{Z}\left(E\cos\phi\cos\theta + E\sin\phi\sin\theta + jE\sin\phi\cos\theta - jE\sin\theta\cos\phi - V\cos\theta + jV\sin\theta\right)^{*} \\
&= \frac{V}{Z}\left((E\cos\phi\cos\theta - V\cos\theta + E\sin\phi\sin\theta) - j(E\sin\phi\cos\theta - E\sin\theta\cos\phi + V\sin\theta)\right)
\end{aligned} \tag{II.17}$$

By comparing (II.17) with (II.13), the active and reactive powers are expressed by:

$$P = \frac{V}{Z}\left((E\cos\phi - V)\cos\theta + \sin\phi\sin\theta\right) \tag{II.18}$$

$$Q = \frac{V}{Z}\left((E\cos\phi - V)\sin\theta - E\sin\phi\cos\theta\right) \tag{II.19}$$

II.4.1. Case 1: Pure Inductive Impedance $(\theta = 90°)$

By assuming that there is only an inductance *X* between the inverter and AC bus, it results:

$$X = \omega_o \sum L = \omega_o (L_f + L_T) \tag{II.20}$$

where L_f is the inductance of the filter, L_T is the output inductance, and ω_0 is the fundamental frequency.

By putting Z=X and $\theta = 90°$ in (II.18) and (II.19), it yields:

$$P = \frac{1}{X} EV \sin\phi \tag{II.21}$$

$$Q = \frac{1}{X}(EV\cos\phi - V^2) \tag{II.22}$$

If also the power angle ϕ is very small, then $\sin\phi \approx \phi$ and $\cos\phi \approx 1$, equations (II.21) (II.22) then become:

$$P = \frac{EV}{X}\phi \tag{II.23}$$

$$Q = \frac{V}{X}(E - V) \tag{II.24}$$

Differentials of (II.23), (II.24) are given by:

$$\begin{cases} \dfrac{\partial P}{\partial E} = \dfrac{V}{X}\phi \\ \dfrac{\partial P}{\partial \phi} = \dfrac{EV}{X} \end{cases} \quad \text{and} \quad \begin{cases} \dfrac{\partial Q}{\partial E} = \dfrac{V}{X} \\ \dfrac{\partial Q}{\partial \phi} = 0 \end{cases} \tag{II.25}$$

As seen in equation (II.25), the active power depends on the power angle ϕ and can be adjusted with the voltage angle ϕ, and reactive power depends on the output voltage E and can be regulated with voltage amplitude E separately. In order to realize power sharing between parallel inverters, we can use the traditional real power versus frequency ($P-\omega$) and reactive power versus voltage (Q-E) droop characteristics. The frequency and the amplitude of the inverter output voltage reference can be expressed as follows:

$$\omega = \omega_o - m_p(P - P^*) \tag{II.28}$$

$$E = E_o - n_q(Q - Q^*) \tag{II.29}$$

where ω is the system frequency, ω_o is the nominal frequency set point, m_p is the real power droop coefficient, E is the measured output voltage, E_o is the nominal voltage set point, and n_q is the reactive power droop coefficient.

The droop characteristics and block diagram of power control based on formulas (II.28) and (II.29) are shown in Figs. (II.6) and (II.7), respectively.

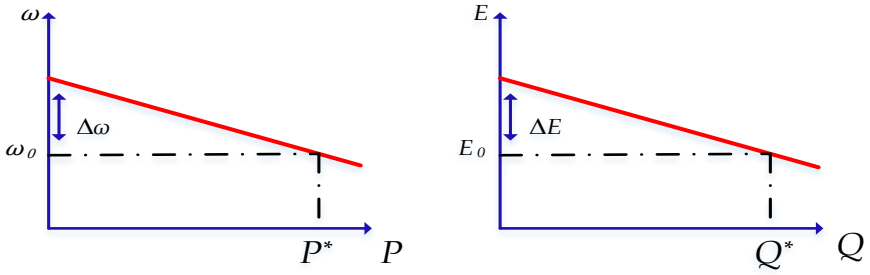

Fig.II.6. Droop characteristics for inductive output impedance

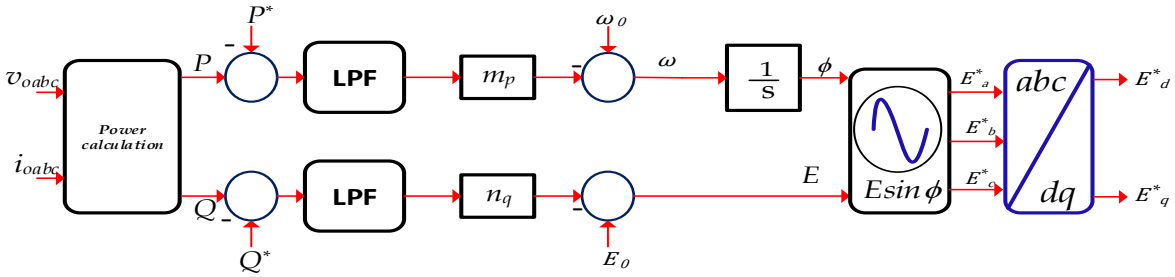

Fig. II.7. Block diagram of the droop control for inductive output impedance

II.4.2.Case 1: Pure Resistive Impedance ($\theta = 0°$)

In the case of a microgrid, the equivalent impedance between any two DG systems can be either resistive or inductive. The line impedance becomes resistive when the ratio R/X is higher. Thus, with $Z = R$ and θ=0°, the equations (II.18) and (II.19) can be written as follows:

$$P = \frac{1}{R}(EV\cos\phi - V^2) \tag{II.30}$$

$$Q = -\frac{1}{R}EV\sin\phi \tag{II.31}$$

In general, the power angle ϕ is normally small, so $\sin\phi \approx \phi$ and $\cos\phi \approx 1$. In this case, equations (II.30) and (II.31) become:

$$P = \frac{V}{R}(E - V) \tag{II.32}$$

$$Q = -\frac{EV}{R}\phi \tag{II.33}$$

Differentials of (II.32) (II.33) are given by:

$$\begin{cases} \dfrac{\partial P}{\partial E} = \dfrac{V}{R} \\ \dfrac{\partial P}{\partial \phi} = 0 \end{cases} \quad \text{and} \quad \begin{cases} \dfrac{\partial Q}{\partial E} = -\dfrac{V}{R}\phi \\ \dfrac{\partial Q}{\partial \phi} = -\dfrac{EV}{R} \end{cases} \tag{II.34}$$

As can be seen from the formulas (II.34), the active power *P* is controlled by the inverter voltage amplitude, and it is not affected by the power angle ϕ. The reactive power *Q* can be regulated by the power angle ϕ, and the change of inverter output-voltage amplitude *E* has little impact on it. In this case, *P-E* and *Q-ω* droop controls can be used to realize power sharing between parallel inverters. Thus, the reference of the frequency and inverter output voltage amplitude can be express as follows:

$$\omega = \omega_o + m_q(Q - Q^*) \tag{II.37}$$

$$E = E_o - n_p(P - P^*) \tag{II.38}$$

The droop characteristics and block diagram of power control based on formulas (II.37) and (II.38) are shown in Figs. (II.8) and (II.9), respectively.

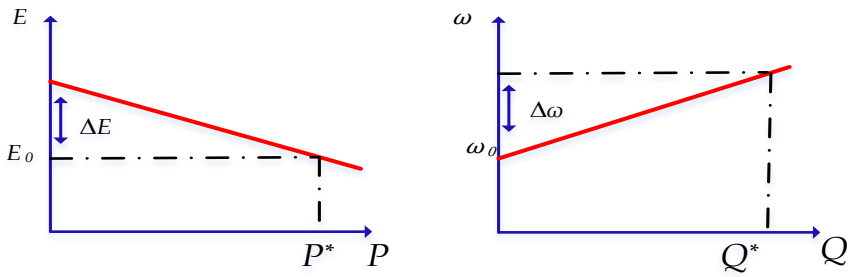

Fig. II.8. Droop characteristics for resistive output impedance

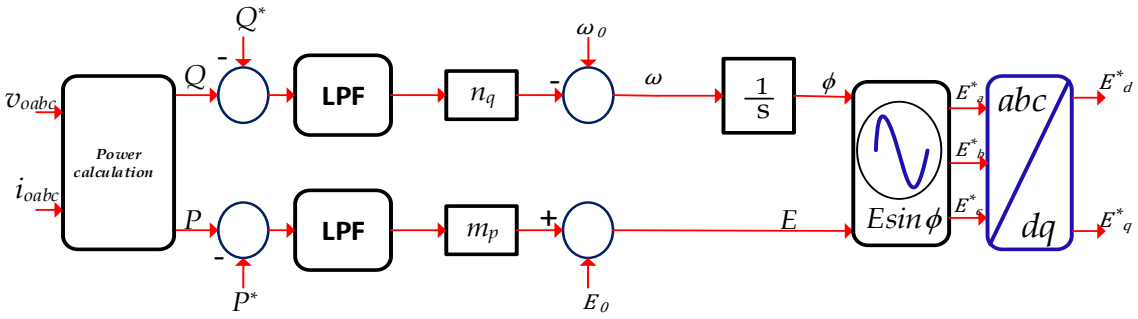

Fig. II.9. Block diagram of the droop control for a resistive output impedance

II.4.3. Droop Coefficients Calculation

In distributed generation microgrids, the droop equations (II.28), (II.29) or (II.37), (II.38) behave like a virtual communication agent that watches over the correct power sharing between the different distributed generators. To achieve this, the droop control must limit variations in the amplitude and frequency of the voltage at the output of each distributed generation unit. Controlled variations are limited by the IEEE Std 1547-2018 [50]. According to this standard, the percentage of tolerable voltage variation value is limited to ±5% of its nominal value, while that of the frequency is limited to ±1%. By following the requirements of the standards, it should be noted that the deviations in the amplitude of the output voltage and frequency must be limited within an acceptable range defined by [51].

$$\begin{cases} |\omega - \omega_o| \le \Delta\omega_{\max} \\ |E - E_O| \le \Delta E_{\max} \end{cases} \quad \text{(II.39)}$$

where $\Delta\omega_{\max}$ and $\Delta E_{\max}$ are the maximum acceptable limits in voltage and frequency variations.

From the standards and authorized limits, the droop coefficients can be calculated whether for a droop control *P-ω/Q-E* or *P-E/Q-ω*.

The droop coefficients for the *P-ω /Q-E* characteristic can be determined as follows:

$$m_p = \frac{\omega_{\max} - \omega_{\min}}{P_{\max} - P_{\min}} \quad \text{(II.40)}$$

$$n_q = \frac{E_{\max} - E_{\min}}{Q_{\max} - Q_{\min}} \quad \text{(II.41)}$$

In the case of droop, which follows the *P-E/Q-ω* characteristic, these parameters are determined as follows:

$$n_p = \frac{E_{\max} - E_{\min}}{P_{\max} - P_{\min}} \quad \text{(II.42)}$$

$$m_q = \frac{\omega_{\max} - \omega_{\min}}{Q_{\max} - Q_{\min}} \quad \text{(II.43)}$$

where $P_{\max}$ and $Q_{\max}$ are the maximum active and reactive powers, respectively; these values are often equal to the power ratings of each DG. $P_{\min}$ and $Q_{\min}$ are the minimum active and reactive powers of each DG often taken as zero. $\omega_{\max}, \omega_{\min}$ and $E_{\max}, E_{\min}$ are the maximum and minimum pulsations as well as the maximum and minimum amplitudes respectively authorized according to the international standards.

II.4.4. Output Impedance Design

The equations governing the dynamic of the LC filter are:

$$L_f \frac{di_i}{dt} = v_i - v_o - ri_i \tag{II.44}$$

$$C_f \frac{dv_o}{dt} = i_i - i_o \tag{II.45}$$

By multiplying the derivative of (II.45) by L_f, one can write:

$$L_f C_f \frac{d^2 v_o}{dt^2} = L_f \frac{di_i}{dt} - L_f \frac{di_o}{dt} \tag{II.46}$$

By using (II.44), it results:

$$L_f C_f \frac{d^2 v_o}{dt^2} = v_i - v_o - ri_i - L_f \frac{di_o}{dt} \tag{II.47}$$

By replacing the expression of i_i calculated from (II.45) into (II.47), it yields:

$$L_f C_f \frac{d^2 v_o}{dt} = v_i - v_o - rC_f \frac{dv_o}{dt} - ri_o - L_f \frac{di_o}{dt} \tag{II.48}$$

This equation can be rearranged as follows:

$$L_f C_f \frac{d^2 v_o}{dt} + rC_f \frac{dv_o}{dt} + v_o + L_f \frac{di_o}{dt} + ri_o = v_i \tag{II.49}$$

In order to achieve a good tracking of the output voltage we can derive the following controller expression

$$v_i = v_{ref} + k_p (v_{ref} - v_o) + k_i \int (v_{ref} - v_o) \tag{II.50}$$

By equalizing the derivatives of (II.49) and (II.50), the following expression can be obtained.

$$L_f C_f \frac{d^3 v_o}{dt} + rC_f \frac{d^2 v_o}{dt} + \frac{dv_o}{dt} + L_f \frac{d^2 i_o}{dt} + r \frac{di_o}{dt} = \frac{dv_{ref}}{dt} + k_p \frac{dv_{ref}}{dt} - k_p \frac{dv_o}{dt} + k_i v_{ref} - k_i v_o \tag{II.51}$$

By introducing Laplace transform, equation (II.51) becomes:

$$(L_f C_f s^3 + rC_f s^2 + (1+k_p)s + k_i) v_o + (L_f s^2 + rs) i_o = ((1+k_p)s + k_i) v_{ref} \tag{II.52}$$

where $v_{ref} = E \sin \omega t$ is the output-voltage reference.

By using (II.52), the closed-loop output voltage dynamic behavior takes the form:

$$v_o = \frac{(1+k_p)s + k_i}{L_f C_f s^3 + rC_f s^2 + (1+k_p)s + k_i} v_{ref} - \frac{L_f s^2 + rs}{L_f C_f s^3 + rC_f s^2 + (1+k_p)s + k_i} i_o \tag{II.53}$$

The inverter can be modeled through a model based on the two-terminal Thevenin equivalent circuit, as can be seen in Fig. (II.5).

$$v_o = F(s)v_{ref} - Z_o i_o(s) \tag{II.54}$$

where Z_o is the output impedance.

In order to allow a proper parallel operation, the closed loop output impedance of the inverter should be examined [52]. The frequency-domain behavior of the output impedance can be analyzed through the bode diagram shown in Fig. (II.10); from which, it can be seen that the impedance is inductive and resistive in same time.

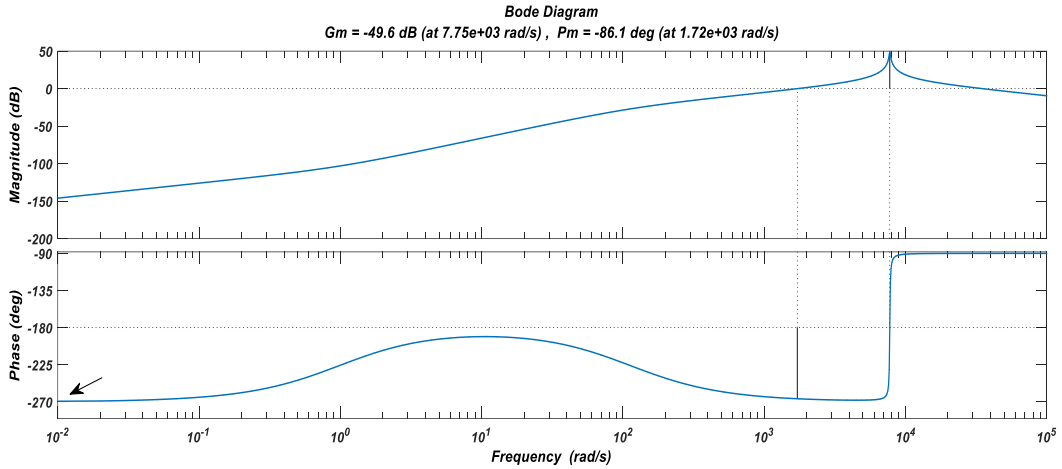

Fig. II.10. Bode diagram of the output impedance Z_o(s)

II.5. Virtual Impedance

Initially, the droop control has been implemented for transmission grids; afterwards, it was adapted for power electronic converters following the same assumptions, giving it great popularity in microgrid applications. However, in a microgrid this assumption does not always hold, because the line impedance may be resistive and the *R*/*X* ratio can be high, which results in the coupling and dynamic instability of the power control with the conventional *P*-ω and *Q*-*E* droop methods [53]. In order to overcome this problem and provide more design flexibility for the connection impedance seen by a DG inverter, the use of virtual impedance has been proposed for inverters operating in standalone parallel mode. This ensures a predominant inductive output impedance of paralleled inverter, which guarantees an active power determined by the power angle and the reactive power

determined by the voltage amplitude [54]. This additional virtual impedance Zv is incorporated into the converter control, which is a current feedback loop that adjusts the voltage reference as shown in Fig. (II.11). This concept results in the modification of the internal controller set points depending on the injected current. For instance, the voltage source based droop controls the voltage reference E^*, which can be altered in order to simulate a voltage drop across a virtual impedance [55].

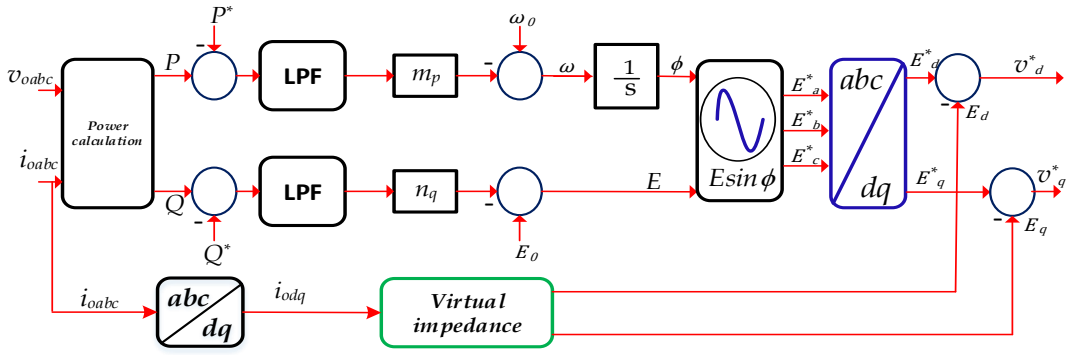

Fig. II.11. Droop control with virtual impedance

In the dq frame, the virtual impedance can be modeled as follows:

$$v_d^* = E_d^* + \omega L_f i_{oq} - R i_{od} \tag{II.55}$$

$$v_q^* = E_q^* - \omega L_f i_{od} - R i_{oq} \tag{II.56}$$

This concept offers the possibility of modifying the impedance seen by the connection of a generator distributed to a desired value without additional losses.

II.6. Power Calculation in Three-Phase Systems

In three-phase systems, the instantaneous active and reactive powers are defined as:

$$P(t) = v_a(t) i_a(t) + v_b(t) i_b(t) + v_c(t) i_c(t) \tag{II.57}$$

$$Q(t) = \frac{1}{\sqrt{3}} \left(v_{ab}(t) i_c(t) + v_{bc}(t) i_a(t) + v_{ac}(t) i_b(t) \right) \tag{II.58}$$

II.6.1. Instantaneous Powers in $\alpha\beta$ Frame

By considering balanced three-phase systems and by defining voltage and current phasors as:

$$\begin{cases} \overline{V}_{\alpha\beta} = V_\alpha + jV_\beta \\ \overline{I}_{\alpha\beta} = I_\alpha - jI_\beta \end{cases} \tag{II.59}$$

The apparent power expression in $\alpha\beta$-frame can be expressed as [56]:

$$\overline{S} = \overline{V}_{\alpha\beta}\overline{I}^*_{\alpha\beta} = (V_\alpha + jV_\beta)(I_\alpha - jI_\beta) \tag{II.60}$$

By rearranging equation (II.60), it is possible to express the active and reactive powers as functions of voltages and currents in the $\alpha\beta$-frame as follows:

$$\begin{aligned} P &= V_\alpha I_\alpha + V_\beta I_\beta \\ Q &= V_\alpha I_\beta - V_\beta I_\alpha \end{aligned} \tag{II.61}$$

II.6.2. Instantaneous Powers in *dq* Frame

Then the instantaneous active and reactive powers in the *dq* frame are given by:

$$\begin{aligned} P(t) &= \mathrm{Re}\left\{\vec{V}\,\vec{I}^{\,*}\right\} = \mathrm{Re}\left\{(V_d + jV_q)(I_d - jI_q)\right\} = V_q I_q + V_d I_d \\ Q(t) &= \mathrm{Im}\left\{\vec{V}\,\vec{I}^{\,*}\right\} = \mathrm{Im}\left\{(V_d + jV_q)(I_d - jI_q)\right\} = V_d I_q - V_q I_d \end{aligned} \tag{II.62}$$

I.7.Low Pass Filter

The instantaneous active and reactive power components P and Q are calculated from equations (II.62). The instantaneous power components are passed through second-order low-pass filters, given in (II.63), to obtain the real and reactive powers $\hat{P}$ and $\hat{Q}$ corresponding to the fundamental component. ω_c represents the cut-off frequency of low-pass filter and ξ represents its damping factor.

$$\hat{P} = \frac{\omega_c^2}{s^2 + 2\xi\omega_c s + \omega_c^2} P \qquad \hat{Q} = \frac{\omega_c^2}{s^2 + 2\xi\omega_c s + \omega_c^2} Q \tag{II.63}$$

The cut-off frequency characterizing these filters is obtained by equation (II.64). For better attenuation of harmonics associated with switching power switches, this frequency must be between 1/3 and 1/2 from frequency switching while ensuring sufficient phase bandwidth control [57].

$$f_c = \frac{1}{2\pi\sqrt{LC}} \tag{II.64}$$

The cut-off frequency can be calculated by drawing the bode diagram using transfer function (II.63), as shown in Fig. (II.12).

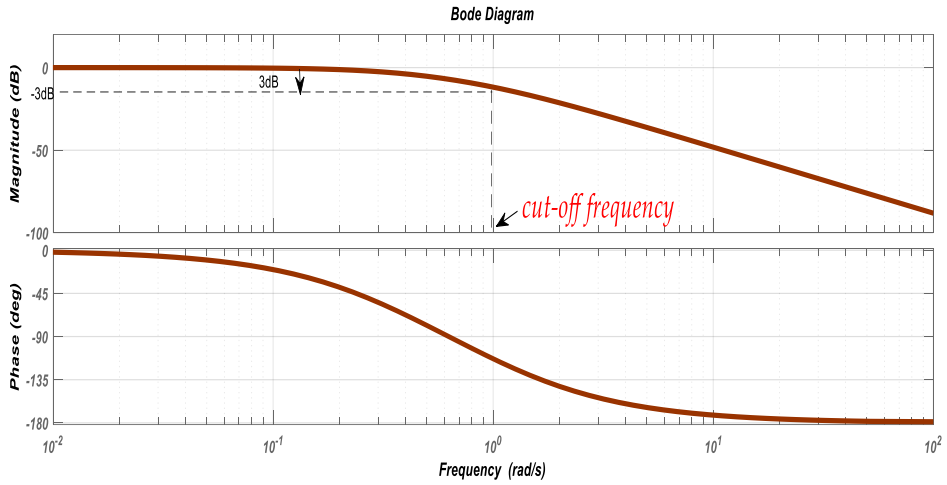

Fig. II.12. Cut-off frequency calculation

II.8. Simulation Results and Discussions

To verify the proposed control strategy, two DG units powered an AC three-phase load through an LC-filter have been built using Simulink environment. The coupling inductances of the two inverters are different. In the following, the system control is tested at both single DG unit and two DG units.

II.8.1 Primary Control of a Single DG Unit

Simulation results of single unit are presented in order to show the feasibility of the proposed droop control illustrated in Fig. (II.13). The control consists of nested voltage and current loops and it is implemented using the selected control parameters listed in APPENDIX A.

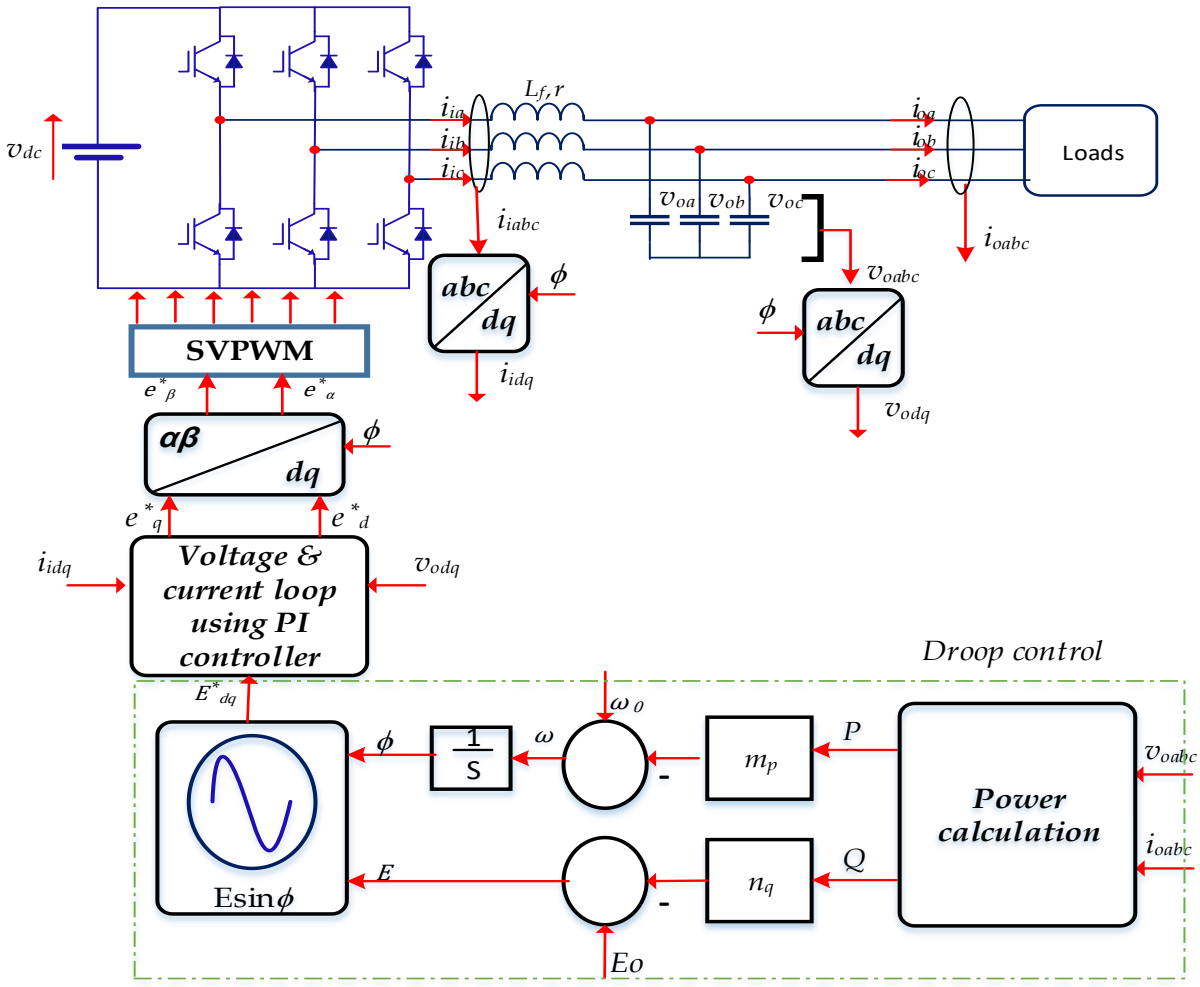

Fig. II.13. Structure of primary control of single DG unit based microgrid using PI controller

Steady state analysis

This section aims to test the performance of the PI control in steady state. As shown in Fig. (II.14), the controller is able to track the reference to regulate the voltage keeping the tracking error percentage near zero. The wave form of the voltage is sinusoidal, and the

ratio of Total Harmonic Distortion THD is 0.41% as see in Fig. (II.15), which is within the MG standards.

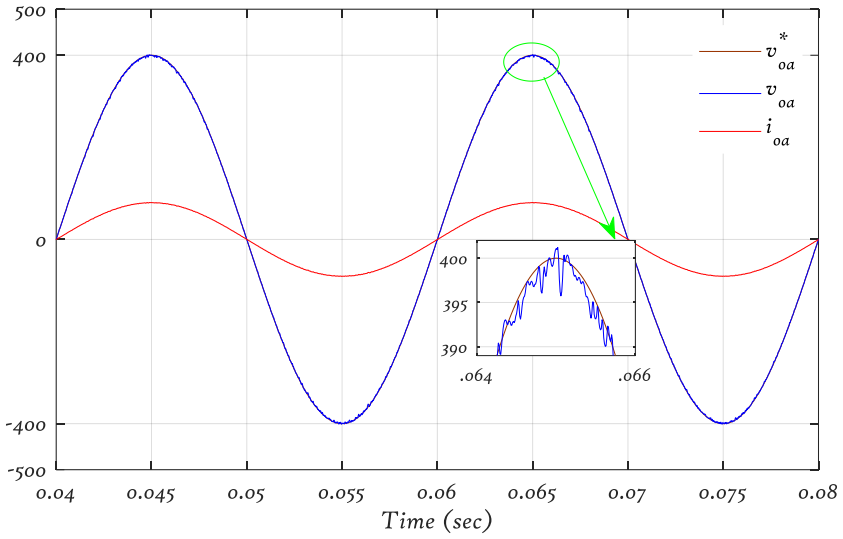

Fig. II.14. Line current and voltage with its reference

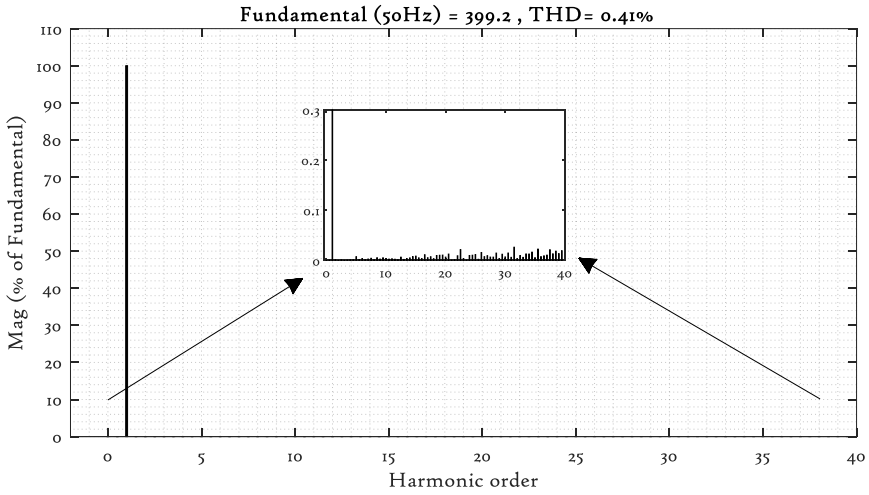

Fig. II.15. Line voltage harmonic spectrum

Transient response analysis

In this test, the performance of PI controller is tested when a step change occurred in the voltage reference. Indeed, at t=0.04 s, the controlled output reference signal of the voltage is increased from 200 V to 400 V.

The obtained results are illustrated in Fig. (II.16), which depicts the evolution of three-phase voltages as well their RMS value. It is remarked that the controller rejects the disturbance and continue tracking the reference within considered time. Also, we noted the settling time for that the signals recover after the disturbance is 12ms, more, and the overshoot exceeds 10%.

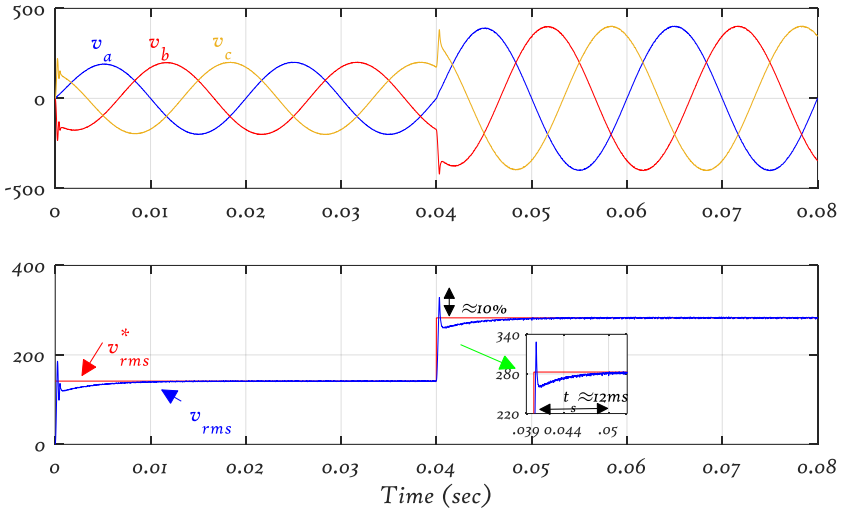

Fig. II.16. Three-phase voltage for reference step change and its RMS value

II.8.2 Droop Control Without Virtual Impedance of Parallel DG Units

The general structure of droop control based islanded microgrid without virtual Impedance is illustrated in Fig. (II.17). Each DG unit provides a part of active and reactive power demanded by loads. In fact, the physical disparities between MG elements will emerge circulating power and currents flowing through the autonomous microgrid. These currents will lead to the improper operation and the instability of the MG [58].

This phenomenon can be easily simulated with the absence of the virtual impedance. Fig (II.17) shows the general view of two DGs composing the adopted MG controlled by the droop control. A simple difference between the parameters of DGs cause large disturbances and the system become instable. This is articulated in the emerged circulating current and power presented in Fig (II.18) and Fig (II.19)

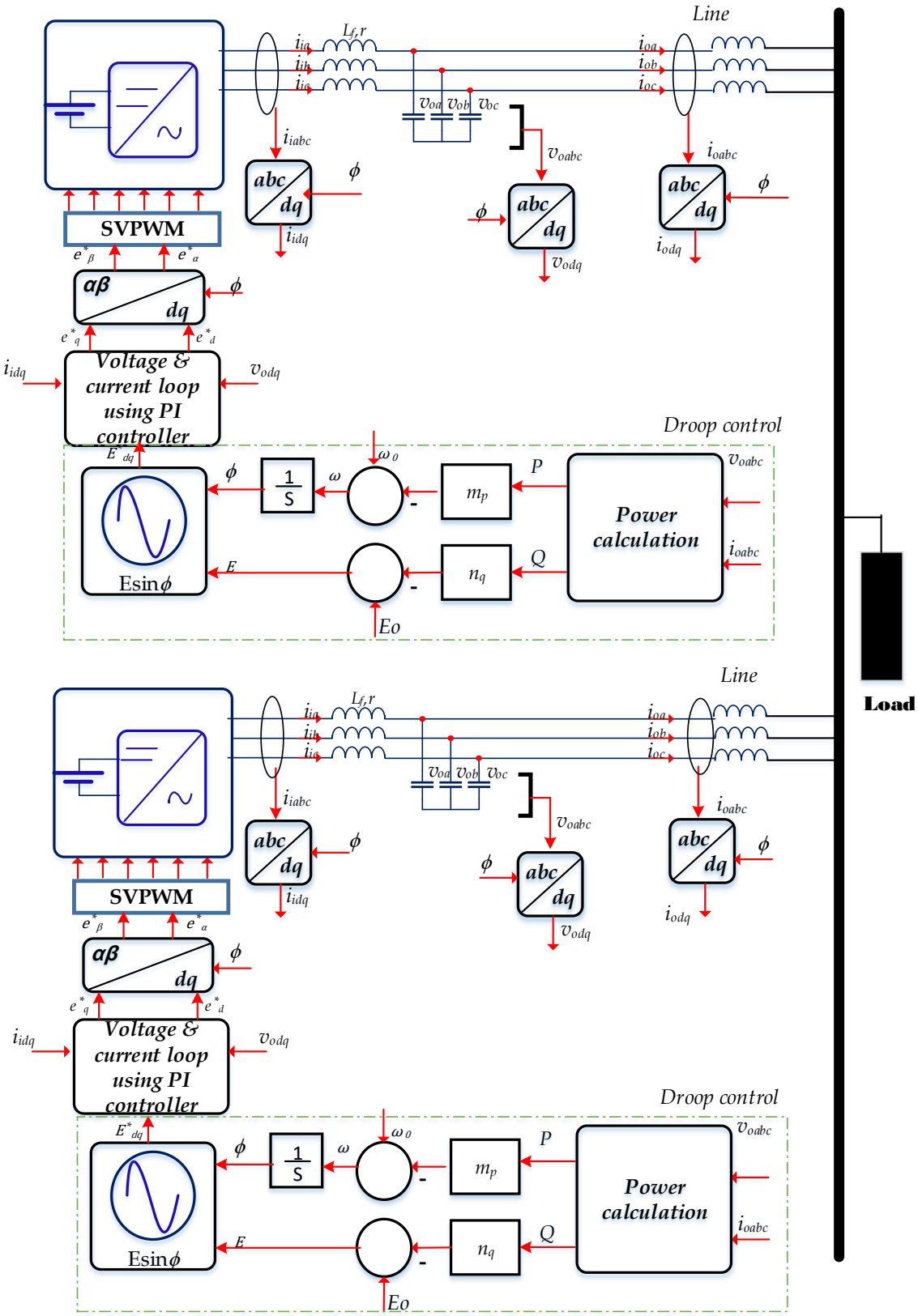

Fig. II.17. Structure of primary control of two DG units without virtual impedance based microgrid using PI controller

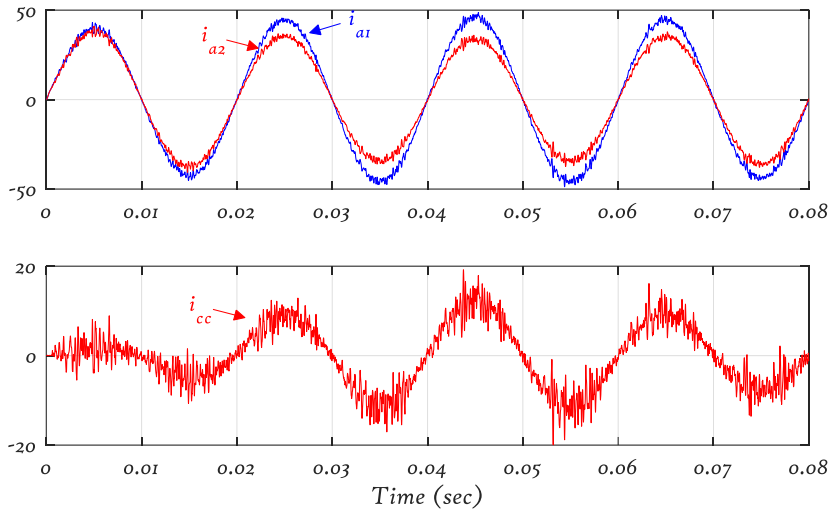

Fig. II.18. Current waveforms and circulating current of two DGs

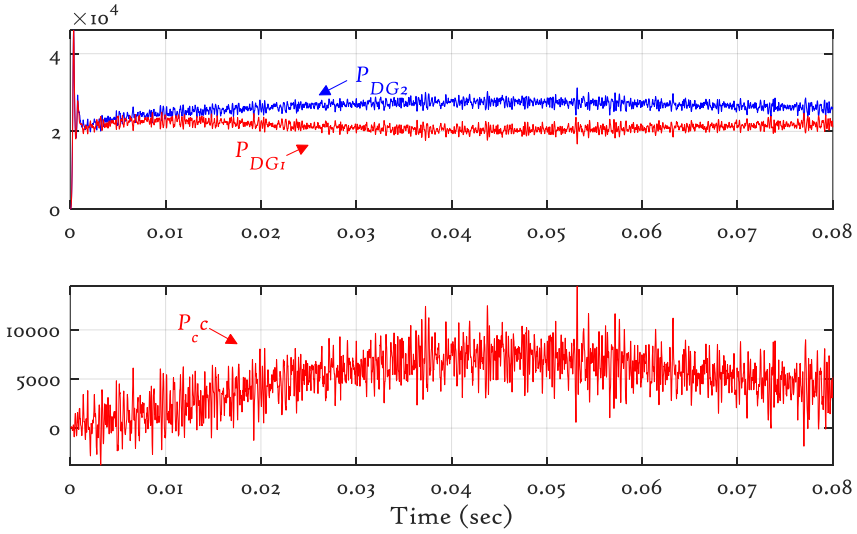

Fig. II.19. Active power sharing of the two DGs

This system needs an appropriate control to control the shared power, which is usually droop control method, in the way of making the system stable and operating properly as in next scenario.

II.8.3 Droop Control With Virtual Impedance of Parallel DG Units

In order to face risks that circulating current can cause, the droop control method is adopted to control the power delivered to the load among two DG units. Fig. (II.20)

illustrates the general view of two DGs composing a MG and controlled by droop control with virtual impedance.

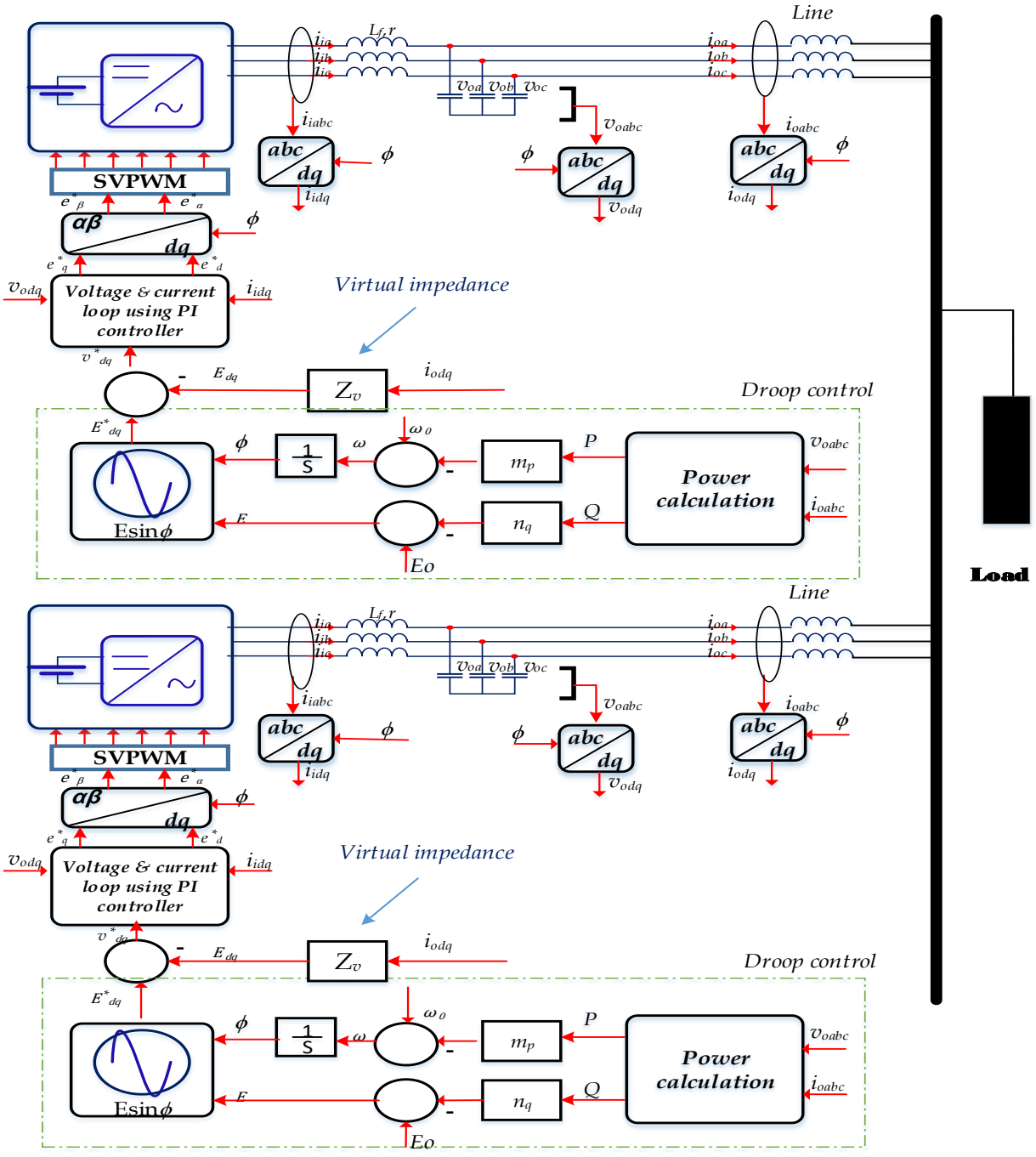

Fig. II.20. Structure of droop control of two DG units with virtual impedance based microgrid using PI controller

Fig (II.21) shows that the power is well shared to the load even in the presence of different impedances where each unit exports half of the total amount. This confirms that the adopted strategy ensures the elimination of circulating currents. By using classic PI control, it is remarked that even though the shared power is well shared, it is yet surrounded by some ripples, and the rate of overshoot is considered.

Fig. (II.22) shows that the circulating current is reduced, which makes the line currents of both inverters balanced. It is worth to mention that the droop control method drops the three-phase voltage in order to make the set of inverter and line impedances similar as well as to eliminate the circulating currents.

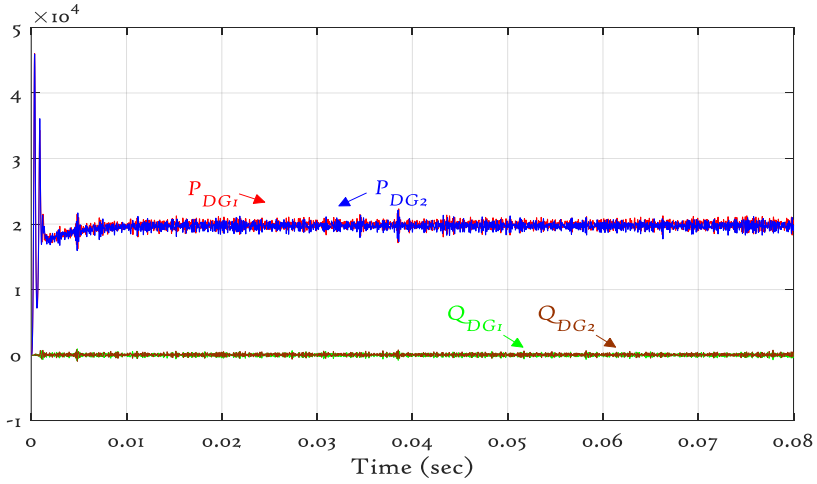

Fig. II.21. Active and reactive power sharing of two DGs controlled by droop control-virtual impedance

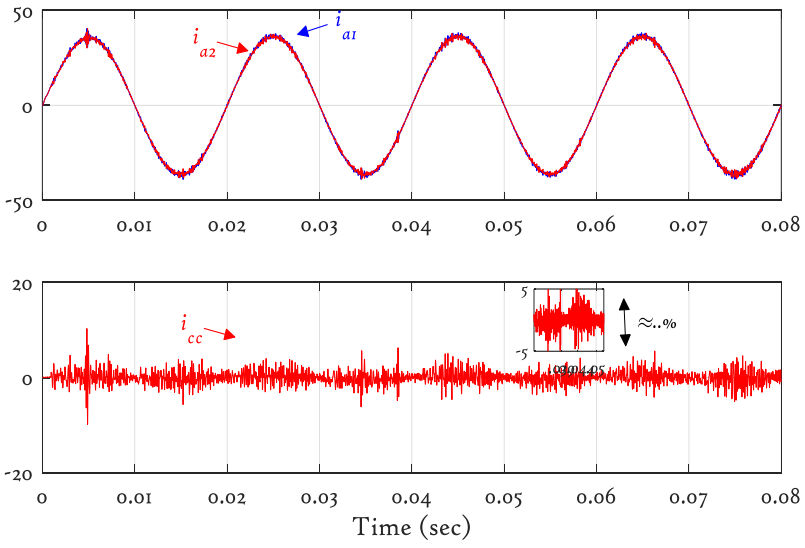

Fig. II.22. Current waveforms of two DGs controlled by droop control-virtual impedance

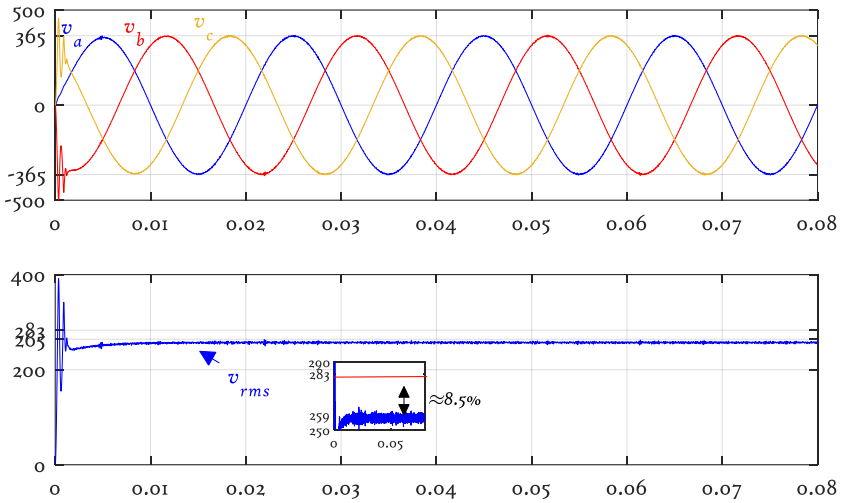

Fig.II. 23.Three-phase voltage and its RMS value

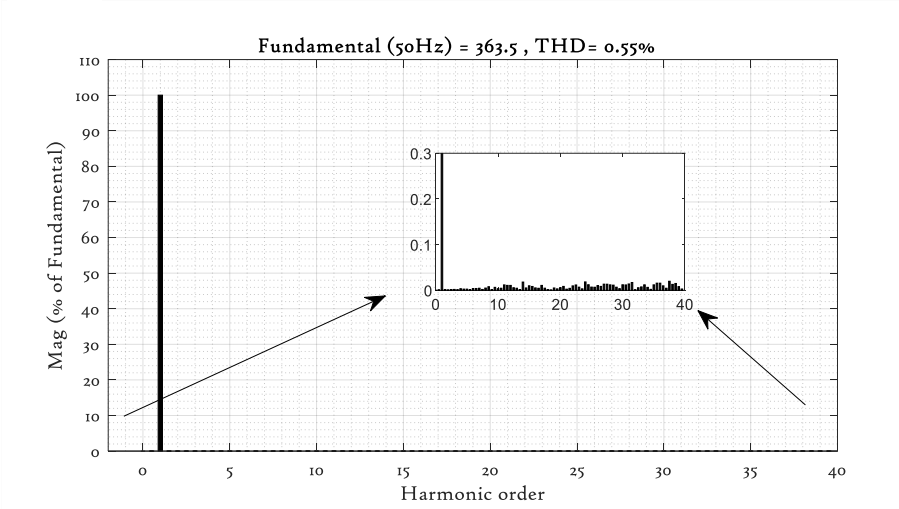

Fig. II.24. Line voltage harmonic spectrum

As can be seen the three phase voltage generated in Fig (II.23), after short transient periods the waveform of the voltage is almost sinusoidal, which depicts the evolution of three-phase voltages as well their RMS. In this test, the amplitude is decrease from 400 V to 365V compared to the single unit.

In Fig (II.24), when the virtual impedance is enabled, the THD drops to only 0.55%.

II.10. Conclusion

In this study, based on the mathematical model of VSI, PI controllers are used to ensure primary control of two parallel DGs units forming a microgrid. The simulation results demonstrate that the PI controller is effective and suitable for improving the time domain characteristics of system response, such as settling time and overshoots.

Also, the droop control method of multiple voltage source converters based an autonomous microgrid is introduced. The power sharing of the DGs sources and the basic principle of virtual impedance is studied. Moreover, the control strategy of virtual impedance is introduced by observing the change of system output characteristics. The power coupling problem caused by the impedance of the resistive line is weakened by controllable virtual impedance. Simulation results prove that the droop control with virtual impedance can significantly improve the uneven output power of inverter caused by different transmission line impedance.

Chapter III

LQR Control of Parallel Inverters Based Islanded Microgrid

III.1. Introduction

As we have previously seen, the control of distributed generator in autonomous MG requires an adequate control of the voltage in a manner to ensure sinusoidal form with lesser THD ratio. The controller should remain robust when the input power changes due to the intermittency of renewable energy sources (RESs) and electrical loads proliferation. In previous chapter, the classical PI controller was adopted to control each DG unit in MG system, even though the control was well-established to regulate the delivered power to loads, it is still fragile against input variations where its rejection was not fast enough and the overshoot rate was considerable even in simple variation. This demonstrates the need to find another advanced control to face these difficulties and constraints.

In literature, there are a lot of control strategies that can be implemented on a distributed generator unit in a microgrid. Amongst them, a control strategy based on linear quadratic regulator (LQR) is largely used since it allows optimizing the control objectives. In this subject, a control based on optimal control equipped with integral action is proposed. The use of LQR with integral action (LQR-I) is motivated by its proprieties that allow optimizing the cost objectives with guaranteeing system stability of the closed loop giving

high power quality of the output voltage with lesser THD ratio, and helping in ensuring optimal load sharing with reduced ripple on both controlled power and minimized circulating current. In point of fact, this control enables to design a feedback gain matrix that will optimally control dynamic systems such as MG. This is based on minimizing the cost function making the error between the output the reference objectives close zero, which means better transient response, reduced tracking error, and reduced power and current ripples. As this approach help remedying problems related power quality in a single distributed generator unit, this will also contribute to solve issues in distributed generator in autonomous microgrid. Because the LQR-I will reduce power and circulating current ripples, by analogy, this will contribute to effectively enhance the power sharing and reduce ripples on suppressed circulating current component. This controller is designed to meet certain robustness facing rapid change of power loads. This chapter presents as the first step the mathematical detail needed to design the LQR with integral action. The stability of closed loop is analyzed and verified, and then the simulation using Simulink is built to validate the effectiveness of the proposed LQR-I and compare its performance with that of classical PI.

III.2. State-Space Representation of Dynamic Systems

III.2.1. VSI State Space Model

In continuous time

The general form of state space presentation of disturbed system is as follows:

$$\begin{cases} \dot{x}(t) = Ax(t) + Bu(t) + Ed(t) \\ y(t) = Cx(t) + Du(t) \end{cases} \quad \text{(III.1)}$$

where *u(t)* is the input vector, *x(t)* is the state vector, *y(t)* is the output vector, *d(t)* is the disturbance vector, *A* is the state or system matrix, *B* is the input matrix, *C* is the output matrix, *D* is the direct transmission matrix, and *E* is the exogenous matrix.

The block diagram for a linear system described by state-space system (III.1) is illustrated in Fig. (III.1).

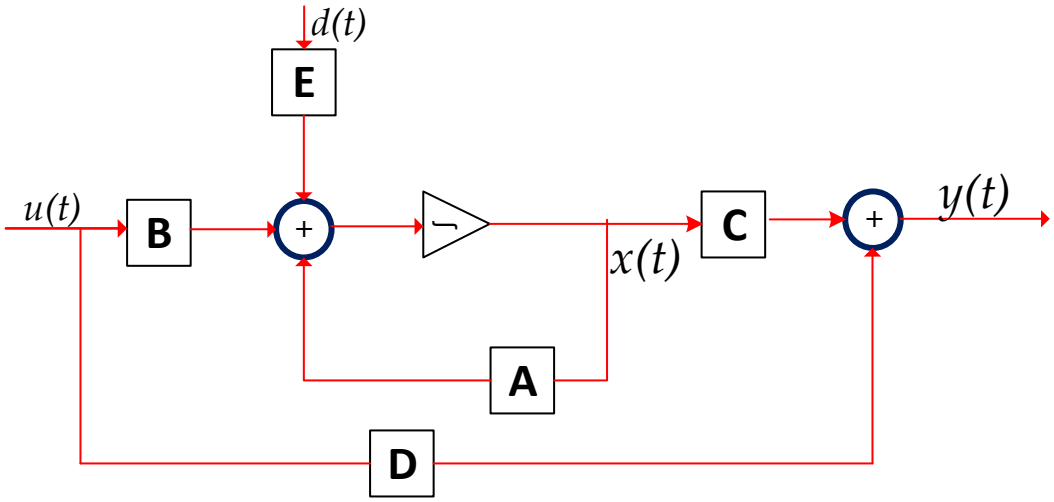

Fig. III.1. State space representation of general linear continuous system

By rewriting (II.20) and (II.21) to fit (III.1) it yields:

- State space of voltage loop

$$\begin{bmatrix} \dot{v}_{od} \\ \dot{v}_{oq} \end{bmatrix} = \begin{bmatrix} 0 & -\omega \\ \omega & 0 \end{bmatrix} \begin{bmatrix} v_{od} \\ v_{oq} \end{bmatrix} + \frac{1}{C_f} \begin{bmatrix} i_{id} \\ i_{iq} \end{bmatrix} - \frac{1}{C_f} \begin{bmatrix} i_{od} \\ i_{oq} \end{bmatrix} \tag{III.2}$$

- State space of current loop

$$\begin{bmatrix} \dot{i}_{id} \\ \dot{i}_{iq} \end{bmatrix} = \begin{bmatrix} -\frac{r}{L_f} & \omega \\ -\omega & -\frac{r}{L_f} \end{bmatrix} \begin{bmatrix} i_{id} \\ i_{iq} \end{bmatrix} + \frac{1}{L_f} \begin{bmatrix} v_{id} \\ v_{iq} \end{bmatrix} - \frac{1}{L_f} \begin{bmatrix} v_{od} \\ v_{oq} \end{bmatrix} \tag{III.3}$$

We can rewrite (III.2) and (III.3) on the same state space as:

$$\frac{d}{dt}\begin{bmatrix} v_{od} \\ v_{oq} \\ i_{id} \\ i_{iq} \end{bmatrix} = \overbrace{\begin{bmatrix} 0 & \omega & \frac{1}{c_f} & 0 \\ -\omega & 0 & 0 & \frac{1}{c_f} \\ -\frac{1}{L_f} & 0 & -\frac{r}{L_f} & \omega \\ 0 & -\frac{1}{L_f} & -\omega & -\frac{r}{L_f} \end{bmatrix}}^{A} \overbrace{\begin{bmatrix} v_{od} \\ v_{oq} \\ i_{id} \\ i_{iq} \end{bmatrix}}^{x(t)} + \overbrace{\begin{bmatrix} 0 & 0 \\ 0 & 0 \\ \frac{1}{L_f} & 0 \\ 0 & \frac{1}{L_f} \end{bmatrix}}^{B} \overbrace{\begin{bmatrix} i_{id} \\ i_{iq} \\ v_{id} \\ v_{iq} \end{bmatrix}}^{u(t)} - \overbrace{\begin{bmatrix} \frac{1}{C_f} & 0 \\ 0 & \frac{1}{C_f} \\ \frac{1}{L_f} & 0 \\ 0 & \frac{1}{L_f} \end{bmatrix}}^{E} \overbrace{\begin{bmatrix} v_{od} \\ v_{oq} \\ i_{od} \\ i_{oq} \end{bmatrix}}^{d(t)} \quad \text{(III.4)}$$

In discreet time

The discrete-time model of a linear continuous-time system can be written in terms of a recursive formula by using linear matrix difference equations as:

$$\begin{aligned} \dot{x}_d(k+1) &= A_d x(k) + B_d u(k) + E_d d(k) \\ y_d(k) &= C_d x(k) + D_d u(k) \end{aligned} \quad \text{(III.5)}$$

It is easy to calculate an approximate discrete model using Euler's method, in which the state space matrix in discrete time can be written as:

$$A_d = I + T_s A = \begin{bmatrix} 1 & T_s\omega & \frac{T_s}{c_f} & 0 \\ -T_s\omega & 1 & 0 & \frac{T_s}{c_f} \\ -\frac{T_s}{L_f} & 0 & -\frac{T_s r}{L_f} & T_s\omega \\ 0 & -\frac{T_s}{L_f} & -T_s\omega & -\frac{T_s r}{L_f} \end{bmatrix} \quad \text{(III.6)}$$

$$B_d = T_s B = \begin{bmatrix} 0 & 0 \\ 0 & 0 \\ \frac{T_s}{L_f} & 0 \\ 0 & \frac{T_s}{L_f} \end{bmatrix} \quad \text{(III.7)}$$

$$E_d = T_s E = \begin{bmatrix} -\frac{T_s}{C_f} & 0 \\ 0 & -\frac{T_s}{C_f} \\ -\frac{T_s}{L_f} & 0 \\ 0 & -\frac{T_s}{L_f} \end{bmatrix} \quad \text{(III.8)}$$

$$\text{and} \quad C_d = \begin{bmatrix} 1 & 0 & 0 & 0 \\ 0 & 1 & 0 & 0 \end{bmatrix} \quad \text{(III.9)}$$

The schematic of a discrete of state space representation is shown below:

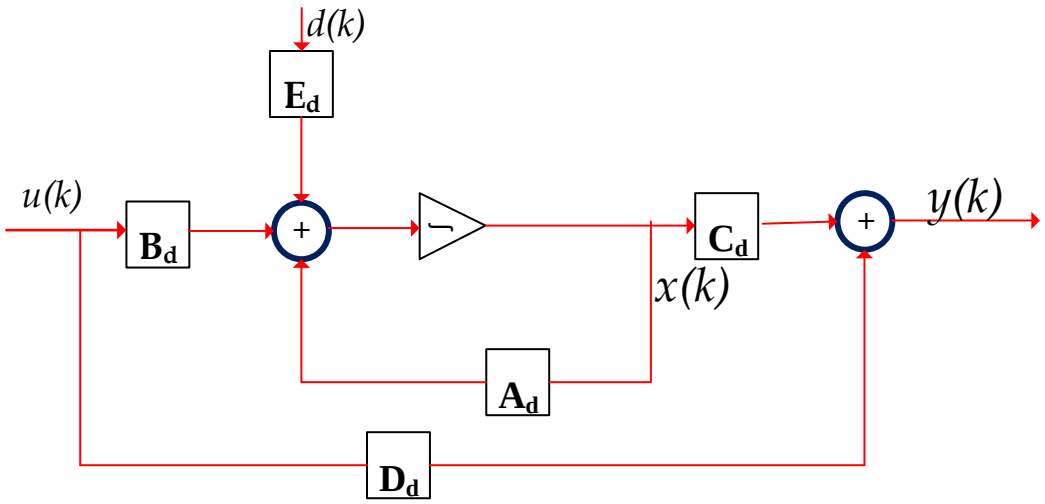

Fig. III.2. State space representation of general discrete time linear system

In what follows, the impact of the disturbances is neglected and the load is assumed to be linear.

III.3. General Format of State Feedback with Pole Placement

To complete state feedback design, the gain matrix *G* need to be specified.

The linear control law is given by:

$$u = -Gx \quad \text{(III.10)}$$

where *G* is a constant gain matrix.

For single input system (SISO), *G* is given by:

$$G = \begin{bmatrix} G_1 & G_2 & \dots & G_n \end{bmatrix} \tag{III.11}$$

For multi-input system (MIMO), *G* is given by:

$$G = \begin{bmatrix} G_{11} & G_{12} & \dots & G_{1n} \\ G_{21} & G_{22} & \dots & G_{2n} \\ \vdots & \vdots & \ddots & \vdots \\ G_{m1} & G_{m2} & \dots & G_{mn} \end{bmatrix} \tag{III.12}$$

The closed-loop equation is

$$\dot{x} = (A - BG)x \tag{III.13}$$

In order to ensure that the closed-loop system to be asymptotically stable the closed-loop dynamics matrix *A-BG* must have its characteristic roots in the left half-plane. If the system is controllable, this can be accomplished by a suitable choice of the gain matrix poles of the closed loop system.

$$roots \ \det(SI - (A - BG)) \tag{III.14}$$

- Pole-placement method

The gain matrix *G* is chosen such that the poles of the closed-loop systems are in specified positions. More precisely, suppose that the desired locations are $s_1, s_2, ..., s_n$, which are either real or complex conjugated pairs, the matrix *G* is chosen so that the characteristic equation verify the following equality:

$$\alpha_c(s) = \det(SI - (A - BG)) = (s - s_1)(s - s_2)....(s - s_n) \tag{III.15}$$

The system stability is ensured by moving its poles into the interior of the left half of the *S* plane as depicted in Fig. (III.3).

To apply the pole placement design method, the following steps should be performed.

1- check the system controllability $M_c = \begin{bmatrix} B & BA & BA^2 \end{bmatrix}$

2- obtain the desired characteristics equation

3 –obtain the determinant of matrix $SI - (A - BG)$

4- comparing coefficient of (1) and (2)

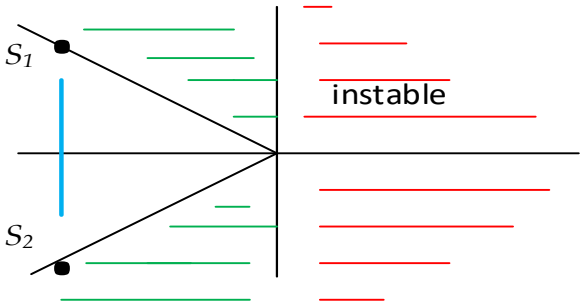

Fig. III.3. Pole placement plan region

III.4. State Feedback with Integral Control

Normally, the use of state feedback controller by exploiting solely the pole-placement can engender steady-state errors. To overcome this drawback, an additional integral action is added to the controller [59]. Fig. (III.4) shows the control diagram with integral control.

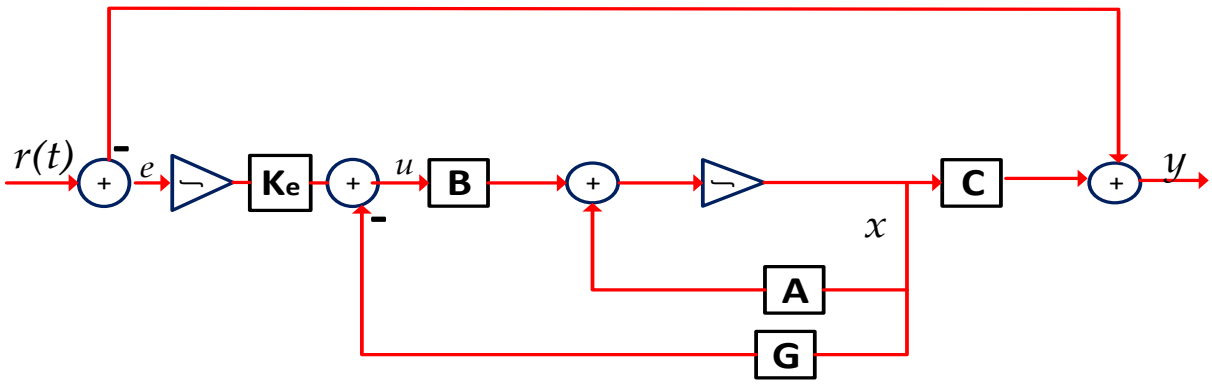

Fig. III.4. Detailed block diagram of system with state feedback and integral control

From the block diagram above, let define the system state space model with integral control as follows [60]:

$$\begin{bmatrix} \dot{x}(t) \\ \dot{\varepsilon}(t) \end{bmatrix} = \begin{bmatrix} A & 0 \\ -C & 0 \end{bmatrix} \begin{bmatrix} x(t) \\ \varepsilon(t) \end{bmatrix} + \begin{bmatrix} B \\ 0 \end{bmatrix} u(t) + \begin{bmatrix} 0 \\ 1 \end{bmatrix} r(t) \tag{III.16}$$

and

$$y(t) = \begin{bmatrix} C & 0 \end{bmatrix} \begin{bmatrix} x(t) \\ \varepsilon(t) \end{bmatrix} \tag{III.17}$$

From Fig. (III.5), the control law is expressed by:

$$u(t) = -Gx(t) + K_e \varepsilon(t) = -\begin{bmatrix} G & K_e \end{bmatrix} \begin{bmatrix} x(t) \\ \varepsilon(t) \end{bmatrix} \tag{III.18}$$

III.4.1. Feed-Forward Gain Design

The closed loop transfer function matrix is given by:

$$H_{clp}(s) = C(sI - A + BG)^{-1} BK_e \tag{III.19}$$

The steady state response of the system is:

$$y_{ss} = H_{clp}(s = 0) r_{ss} = -C(A - BG)^{-1} BK_e r_{ss} \tag{III.20}$$

The following equation needs to be solved in continuous time.

$$-C(A - BG)^{-1} BK_e = I \Rightarrow K_e = -(C(A - BG)^{-1} B)^{-1}$$

(III.21)

In case of SISO system, equation (III.19) can be simplified to:

$$K_e = \frac{1}{c(A - bG)^{-1} b} \tag{III.22}$$

III.5. Optimal Control

The main objective of optimal control is to determine the control signals that will drive a system to satisfy certain physical constraints and at the same time maximize or minimize a chosen performance criterion (performance index or cost function). We are interested in finding an optimal control law *u(t)*, which will drive the system *S* to go from the initial state to a given final state with certain constraints on the control signals and states and at the same time maximizing or minimizing the given performance index *J* [61].

The formulation of the optimal control problem requires [62]:

1. A mathematical model of the process to be controlled,

2. A specification of the performance index,

3. Accuracy of boundary conditions and physical constraints on states and/or commands.

III.5.1. Quadratic Optimal Regulator

An advantage of the quadratic optimal control method over the pole-placement method is that the former provides a systematic way of computing the state feedback control gain matrix.

The LQR controller uses an optimal control algorithm to minimize a cost function. The cost function involves the states and the system inputs along with the Q and R matrices [63]; the *Q* and *R* matrices represent the weights assigned to the states and inputs. By varying the values of these two matrices, the total value of the cost function can be adjusted according to the desired output. The two main quantities that need to be optimized for the system model are the power consumption and time response. For a faster response of the controller, the *Q* matrix values need to be appropriately chosen, whereas for minimizing

the power consumption while achieving the desired set point without focusing on the time response, the *R* matrix values need to be adequately selected [64] .

Let now consider the optimal regulator problem that, for a given linear system presented by:

$$\dot{x} = Ax + Bu \tag{III.23}$$

The task is to determine the matrix *G* of the following optimal control vector:

$$u(t) = -Gx(t) \tag{III.24}$$

so that the following performance index is minimized:

$$J = \int_0^\infty (x^T Qx + u^T Ru)dt \tag{III.25}$$

where Q is a positive-definite (or positive-semi-definite) Hermitian or real symmetric matrix and R is a positive-definite Hermitian or real symmetric matrix. Note that the second term on the right-hand side of equation (III.25) accounts for the expenditure of the energy of the control signals. The matrices *Q* and *R* determine the relative importance of the error and the expenditure of this energy. In this problem, control vector *u(t)* is assumed to be unconstrained. As will be seen later, the linear control law given by equation (III.24) is the optimal control law. Therefore, if the unknown elements of the matrix *G* are determined to minimize the performance index, then *u(t)=–Gx(t)* is optimal for any initial state *x (0).*

Now let us solve the optimization problem by substituting equation (III.24) into equation (III.23), which results in:

$$\dot{x} = Ax - BGx = (A - BG)x \tag{III.26}$$

In equation (III.26), the matrix *A-BG* is assumed to be stable, which means that the eigenvalues of *A-BG* have negative real parts.

Substituting equation (III.24) into equation (III.25) yields

$$J = \int_0^\infty (x^T Qx + x^T G^T RGx)dt$$
$$= \int_0^\infty x^T (Q + G^T RG)xdt \quad \text{(III.27)}$$

Let us set

$$x^T (Q + G^T RG)x = -\frac{d}{dt}(x^T Sx) \quad \text{(III.28)}$$

where S is a positive-definite Hermitian or real symmetric matrix. Then (III.28) becomes:

$$x^T (Q + G^T RG)x = -\dot{x}^T Sx - x^T S\dot{x} = -x^T \left[(A - BG)^T S + S(A - BG) \right] x \quad \text{(III.29)}$$

Comparing both sides of this last equation and noting that this equation must hold for any x, we require that:

$$(A - BG)^T S + S(A - BG) = -(Q + G^T RG) \quad \text{(III.30)}$$

It can be proved that if A-BG is a stable matrix, there exists a positive-definite matrix S that satisfies equation (III.30) [65].

Hence our procedure is to determine the elements of *S* from equation (III.30) and see if it is positive or definite; note that more than one matrix *S* may satisfy this equation. If the system is stable, there always exists one positive-definite matrix *S* to satisfy this equation. This means that, if we solve this equation and find one positive-definite matrix *S*, the system is stable. Other *S* matrices that satisfy this equation are not positive definite and must be discarded [66].

The performance index *J* can be evaluated as:

$$J = \int_0^\infty x^T (Q + G^T RG)xdt = -x^T Sx\Big|_0^\infty = -x^T(\infty)Sx(\infty) + x^T(0)Sx(0) \quad \text{(III.31)}$$

Since all eigenvalues of *A-BG* are assumed to have negative real parts, we have $x(\infty) \to 0$

Therefore, we obtain:

$$J = x^T(0)Sx(0) \quad \text{(III.32)}$$

Thus, the performance index *J* can be obtained in terms of the initial conditions *x (0)* and *S*.

To obtain the solution to the quadratic optimal control problem, we proceed as follows: Since *R* has been assumed to be a positive-definite Hermitian or real symmetric matrix, we can write:

$$R = T^T T \tag{III.33}$$

where *T* is a nonsingular matrix. Then equation (III.30) can be written as:

$$(A^T - G^T B)S + S(A - BG) + Q + G^T T^T TG = 0 \tag{III.34}$$

which can be rewritten as follows:

$$A^T S + SA + \left[TG - (T^T)^{-1} B^T S\right]^T \left[TG - (T^T)^{-1} B^T S\right] - SBR^{-1} B^T S + Q = 0 \tag{III.35}$$

The minimization of *J* concerning *G* requires the minimization of (III.36) concerning *G*.

$$x^T \left[TG - (T^T)^{-1} B^T S\right]^T \left[TG - (T^T)^{-1} B^T S\right] x \tag{III.36}$$

Since this last expression is nonnegative, the minimum occurs when it is zero, or when

$$TG = (T^T)^{-1} B^T S \tag{III.37}$$

Hence,

$$G = T^{-1}(T^T)^{-1} B^T S = R^{-1} B^T S \tag{III.38}$$

Equation (III.38) gives the optimal matrix *G*. Thus, the optimal control law to the quadratic optimal control problem when the performance index is given by equation (III.24) is linear and is given by:

$$u(t) = -Gx(t) = -R^{-1} B^T S x(t) \tag{III.39}$$

The matrix *G* in equation (III.28) must satisfy Equation (III.30) or the following reduced equation:

$$SA + A^T S - SBR^{-1} B^T S + Q = 0 \tag{III.40}$$

Equation (III.40) is called the reduced-matrix Riccati equation. The design steps may be stated as follows:

1. Solve equation (III.40), the reduced-matrix Riccati equation, for the matrix *S*. (If a positive definite matrix *S* exists (certain systems may not have a positive definite matrix *S*), the system is stable, or matrix *A-BG* is stable.

2. Substitute this matrix *S* into equation (III.40); the resulting matrix *G* is the optimal matrix.

Finally, note that if the performance index is expressed in terms of the output vector rather than the state vector, that is,

$$J = \int_0^\infty (y^T Q y + u^T R u) dt \tag{III.41}$$

then the index can be modified by using the following output equation $y = Cx$ to:

$$J = \int_0^\infty (x^T C^T Q C x + u^T R u) dt \tag{III.42}$$

and the design steps presented in this section can be applied to obtain the optimal matrix *G*.

Noted: the gain in the presence of exogenous variables can also be written as:

$$G_o = -R^{-1} B^T (A_c^T)^{-1} S, \quad \text{with} \quad A_c = A - BG \tag{III.43}$$

In MATLAB, the command $lqr(A, B, Q, R)$ solves the continuous-time, linear, quadratic regulator problem and the associated Riccati equation. This command calculates the optimal feedback gain matrix *G*.

Another command $[K, E, P] = lqr(A, B, Q, R)$ returns the gain matrix *K*, eigenvalue vector *E*, and matrix *P* from Riccati equation.

III.5.2. Cascade Loops Control Based LQR Controller

Control scheme presented in Fig. (III.5) consists of an external voltage loop that provides the current reference and an internal current loop that provides the modulating signals. In this case, LQR controller is used to regulate the output voltage and current of the voltage source converter.

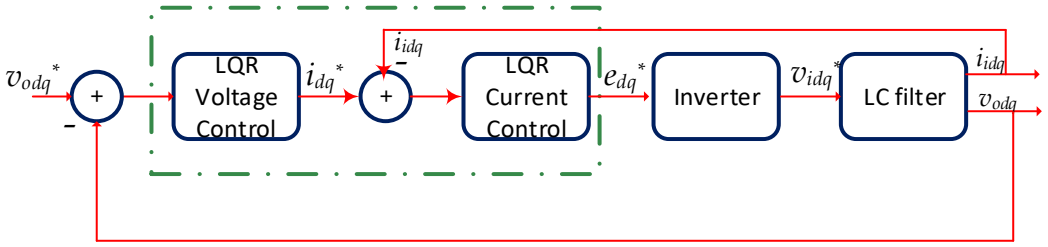

Fig. III.5. Cascaded control loop using LQR controllers

To verify that the tuning is stable, a Root locus of the closed loop transfer function (state space (III.2),(III.3)) for voltage and current are shown in Figs. (III.7), (III.8), (III.9) and (III.10), respectively. The Root locus plot shows that two poles coincide and become complex conjugates. The different colored markers show the trajectory of each eigenvalue and from the figure we can say this is a stable solution.

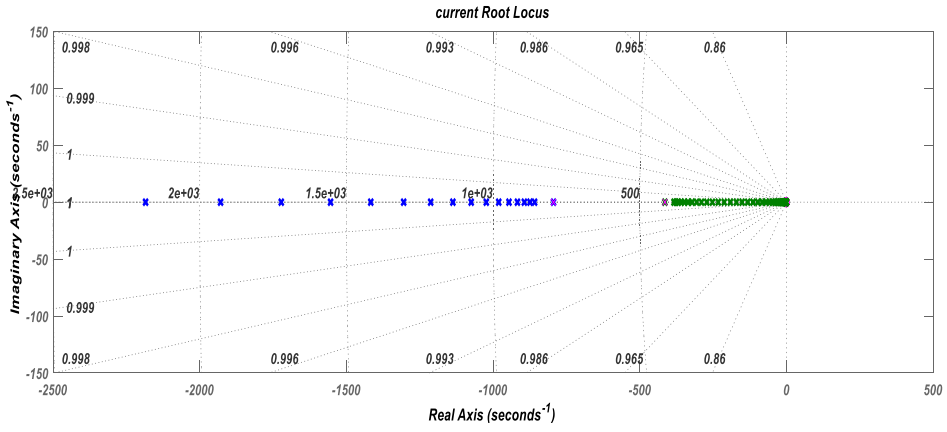

Fig. III.5. Root locus plot for the voltage control by applying the pole placement method

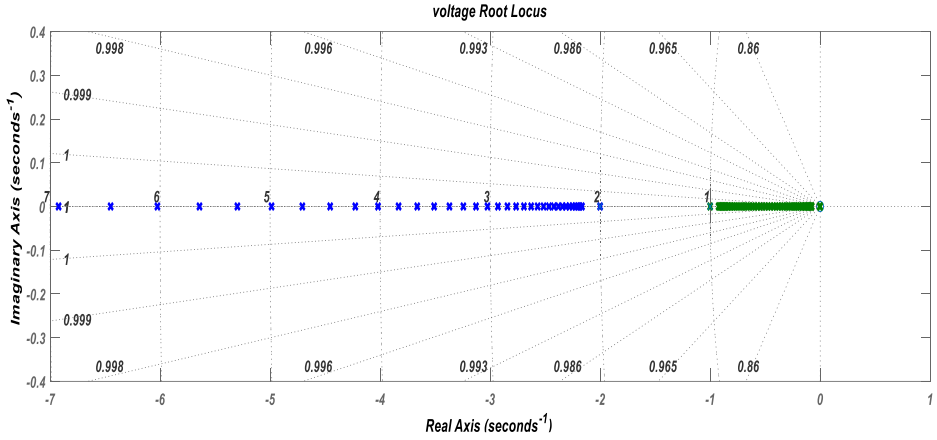

Fig. III.6. Root locus plot for the voltage control by applying the pole LQR method

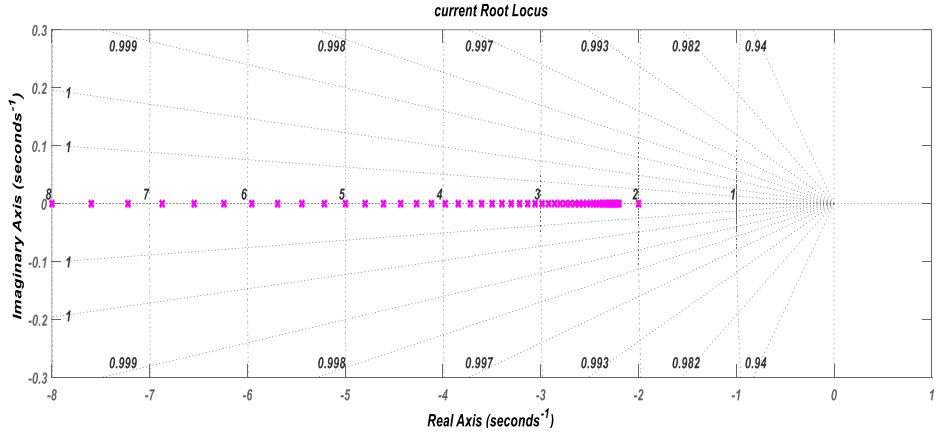

Fig. III.9. Root locus plot for the current control by applying the pole placement method

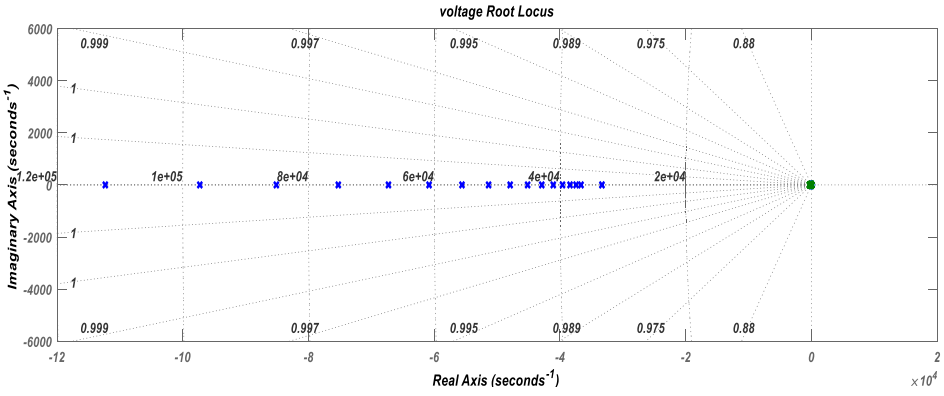

Fig. III.10. Root locus plot for the current control by applying the LQR method

III.6. Simulation Results and Discussion

In the first part we study the effect and the difference between two famous controllers, PI and LQR controllers on a single unit, then in second part we see the effect of the LQR

controller on the droop control with/without virtual impedance and how is the better controller.

III.6.1. LQR of a Single DG Unit

In order to validate the performance of LQR based control of VSI system, the system was implemented in Simulink/Matlab environment using the same parameters given in Appendix A.

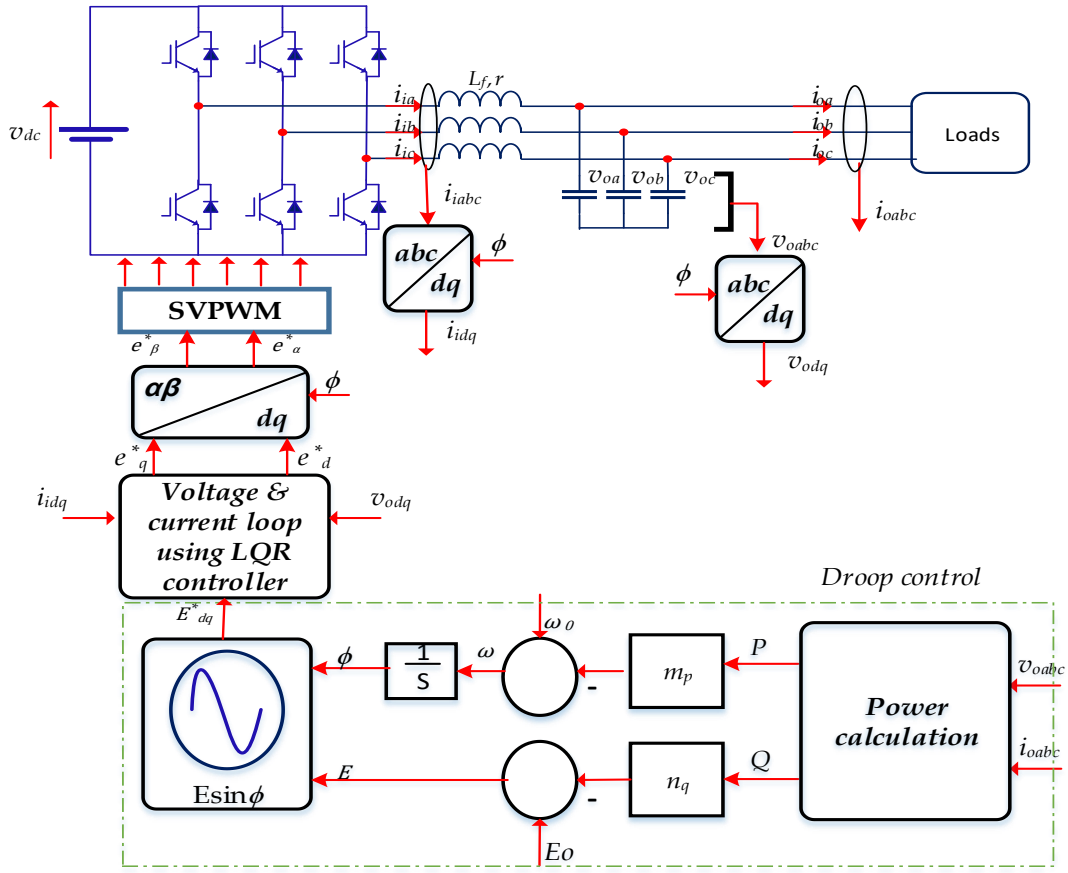

Fig. III.7. Structure of primary control of single DG unit based microgrid using LQR controller

Steady state analysis of a single DG unit

In this test, the performance of the LQR control is evaluated and compared to that of PI control. As shown in Fig. (II.12), the controller is properly tracking the reference to regulate the voltage making the error zero, which is slightly better than that using PI. The voltage

waveform is almost sinusoidal, and the ratio of Total Harmonic Distortion is THD=0.36%, as in Fig. (II.13), which is in accordance with the MG code.

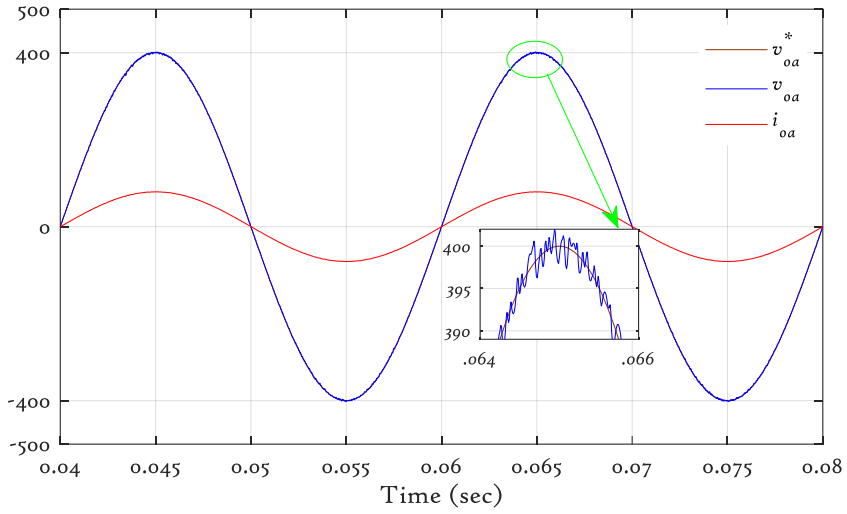

Fig. III.8. Line current and voltage with its reference

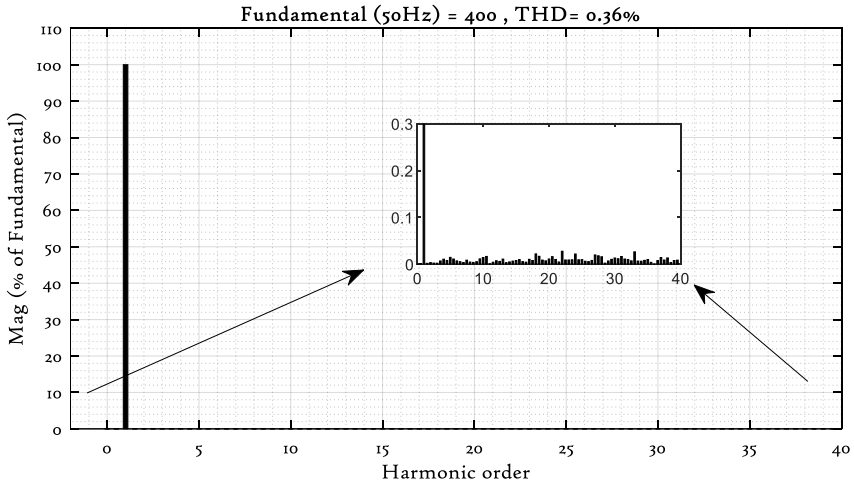

Fig. III.9. Line voltage harmonic spectrum

Transient response analysis of a single DG unit

In this section, the performance of LQR controller is tested when a step-change in the voltage reference is implemented. The evolutions of three-phase voltages as well as its RMS value are illustrated in Fig. (III.14). It can be seen that the LQR controller rejects the disturbance better than PI, where there is no overshoot. The recovering time using LQR is 1.5ms, which is better than that obtained by the classic PI controller.

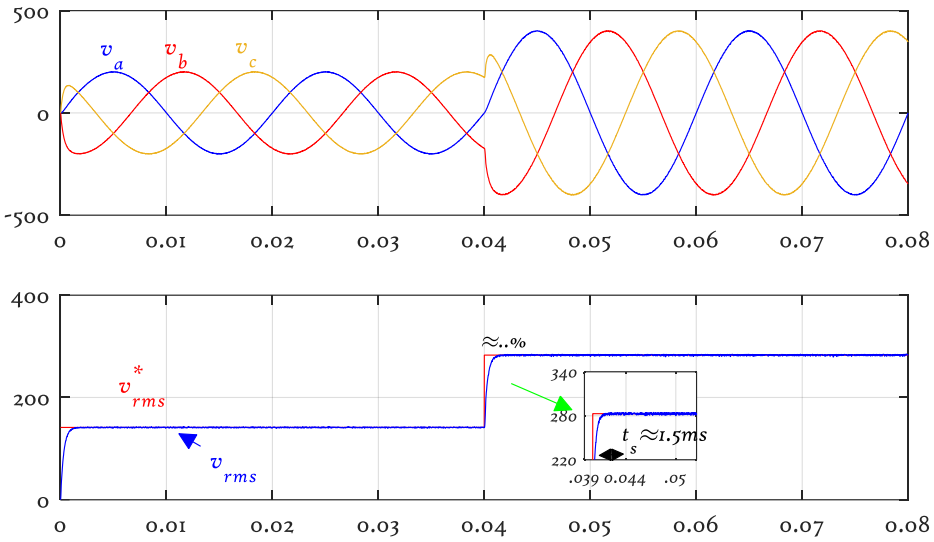

Fig. III.10. Three-phase voltages for a reference step change and their RMS value

III.6.2. Droop Control Without Virtual Impedance of Two Parallel DG Units Using LQR Controllers

As it is well established, the use of parallel DGs will help in sharing load power among several units. This fact will increase the reliability of the microgrid, and enable the continuity of providing power even in case of failure or maintenance. However, due to the physical and the control disparities between MG elements, a large amount of circulating power and currents will emerge and flow through the autonomous microgrid, which leads to the improper operation and the instability of the MG.

This phenomenon can be easily simulated in the absence of the droop control. Fig. (II.17) shows the general view of droop control of two DGs composing an islanded MG. A simple difference between the parameters of DGs causes large disturbances and the system becomes unstable. This is articulated in the emerged circulating current and power in Fig. (III.15) and Fig. (III.16).

This system needs an appropriate control to ensure power sharing, which is usually the droop control method, in the way of making the system stable and operating properly as in the next scenario.

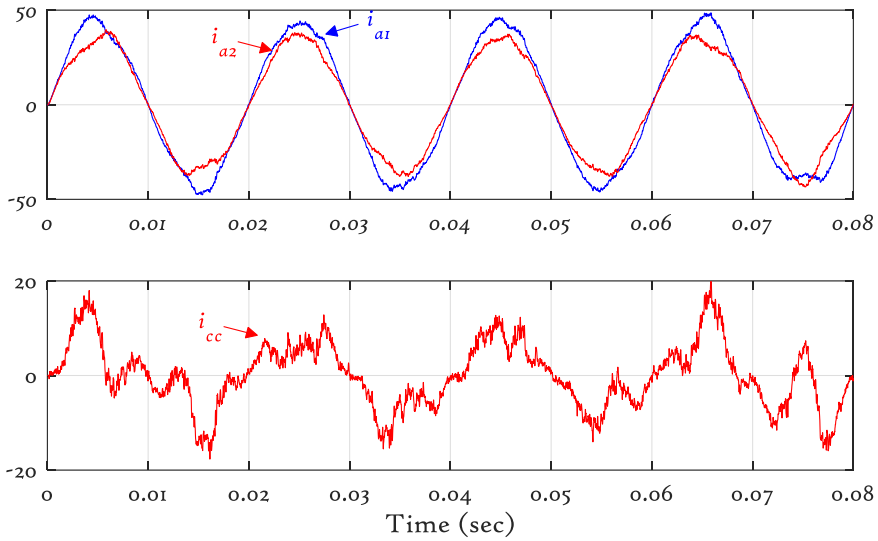

Fig. III.11. Current waveforms of two DGs and their circulating current

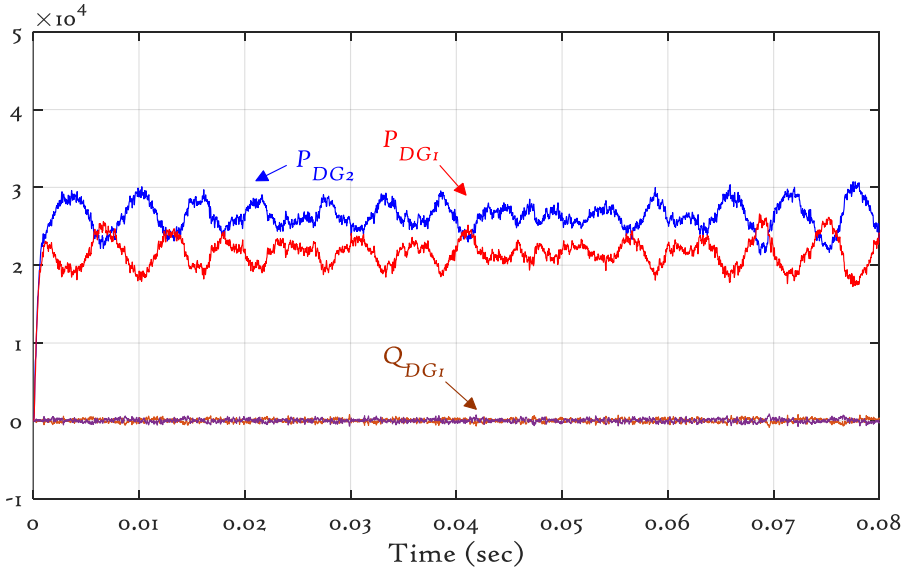

Fig. III.16. Active and reactive powers of the two DGs

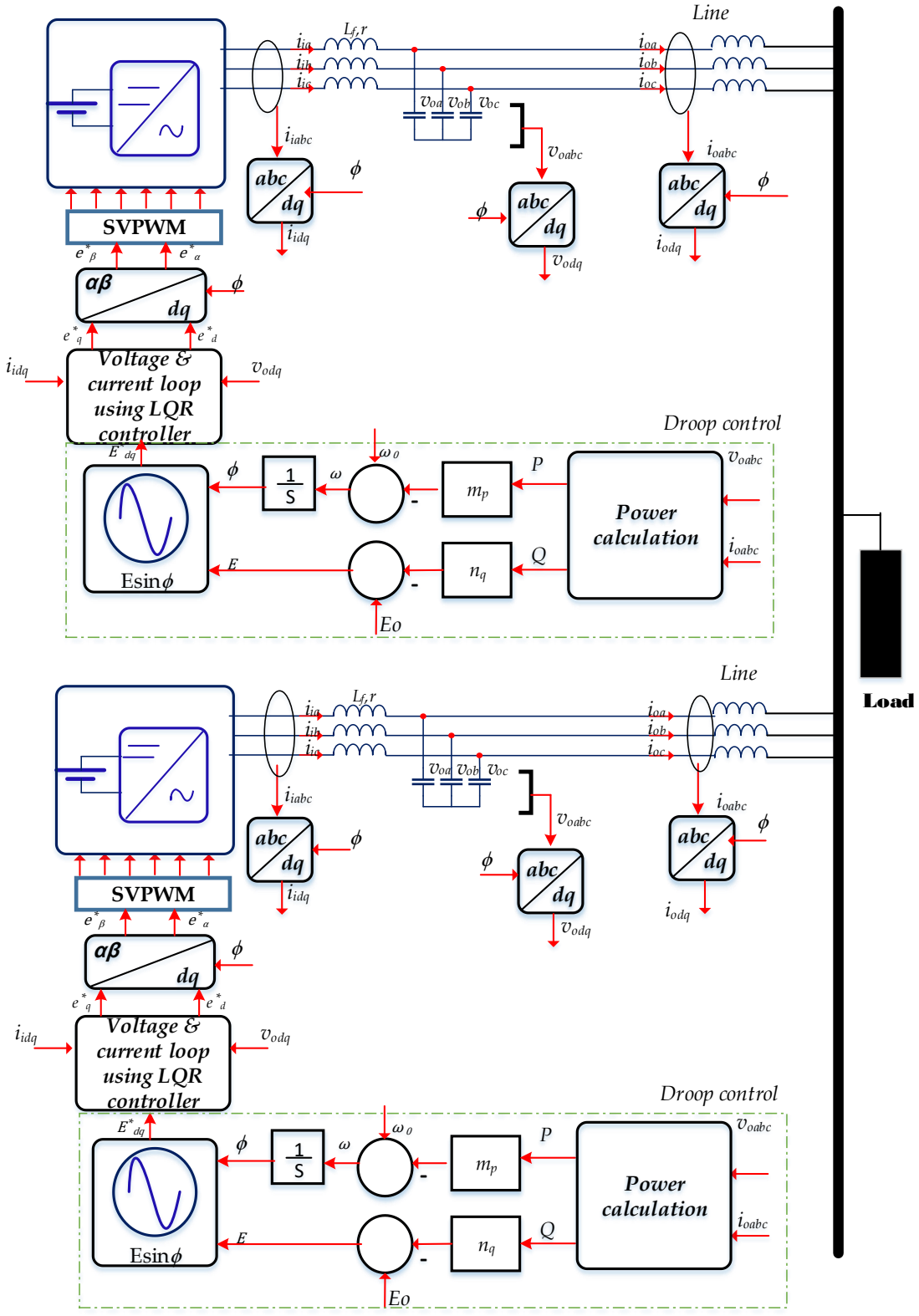

Fig. III.17. Structure of primary control of two DG units without virtual impedance based microgrid using LQR controllers

III.6.1. Droop Control With Virtual Impedance of Two Parallel DG Units Using LQR Controllers

In the way to limit risks that circulating current will cause, we have adopted droop-based control to share the power among two DG units. Fig. (III.18) shows that the power is well shared to the load even in the presence of a difference in line impedances where each unit exports half of the total amount. This confirms that the adopted strategy ensures the elimination of circulating currents. It is remarked that by using LQR control, the component of ripples on the shared power is lesser than that produced using PI.

Fig. (III.20) shows that the circulating current is reduced, which makes the line currents of both inverters balanced. It is worth mentioning that the droop control method drops the three-phase voltage in order to make the set of inverter and line impedances identic as well as to eliminate the circulating currents.

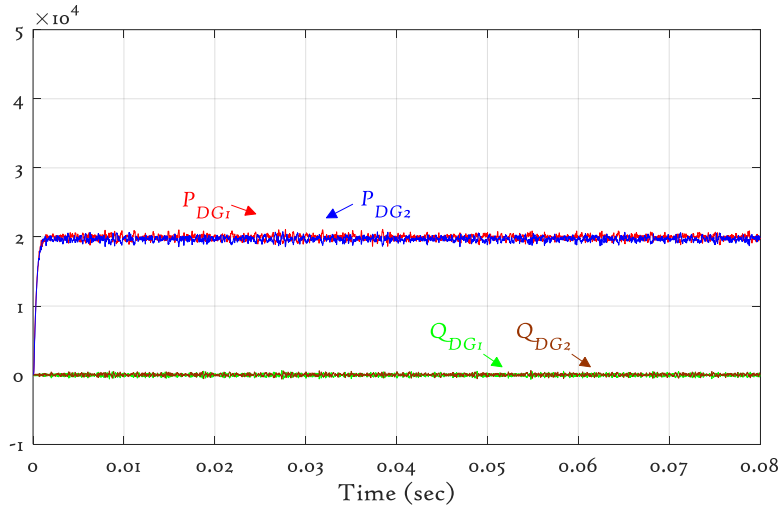

Fig. III.18. Active and reactive powers sharing of two DGs controlled by droop control with virtual impedance

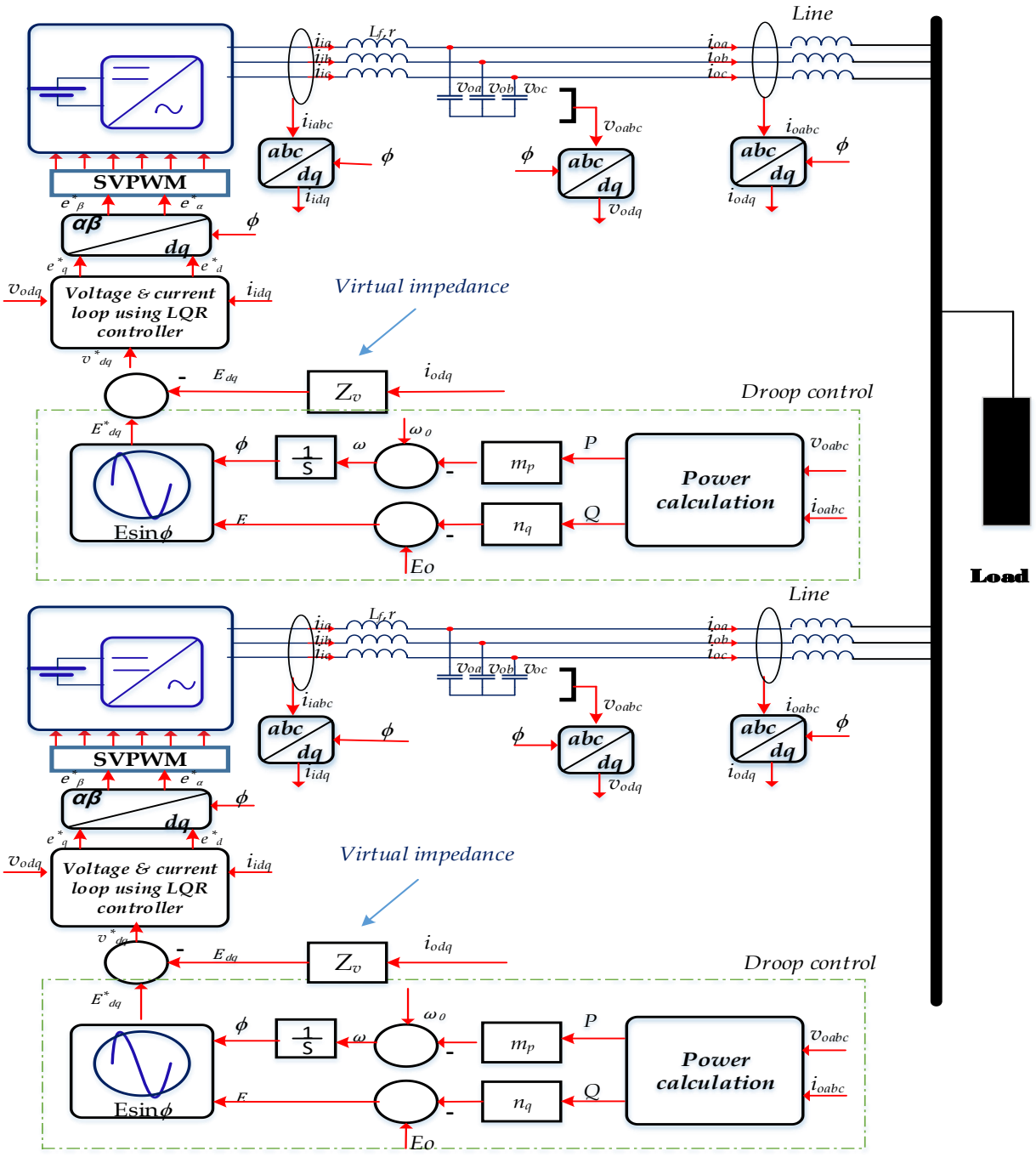

Fig.III. 19. Structure of droop control of two DG units with virtual impedance based microgrid using PI controller

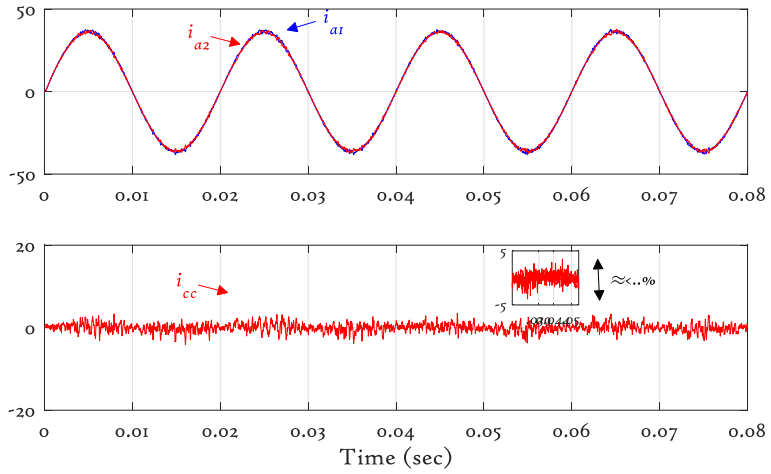

Fig. III.12. Current waveforms of two DGs controlled by droop control with virtual impedance

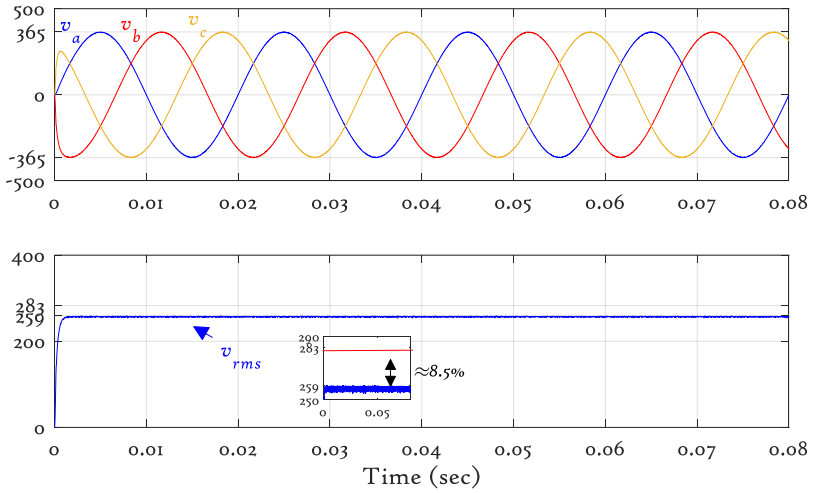

Fig. III.13. Three-phase voltages and their RMS value

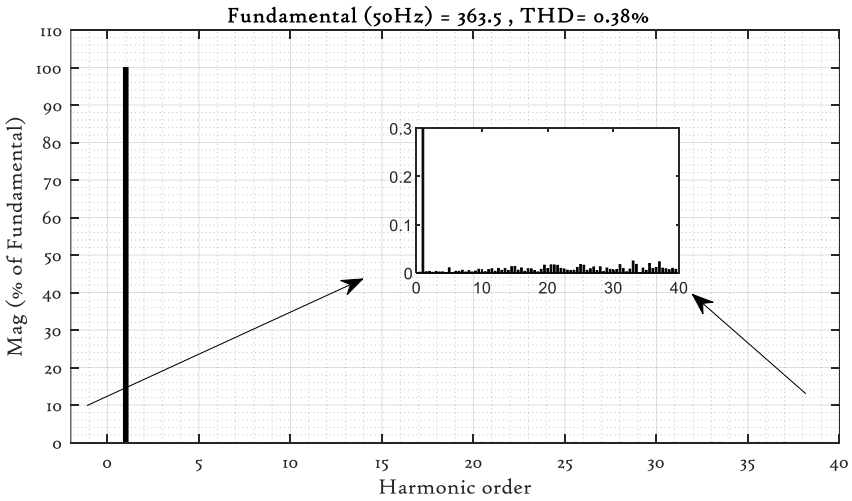

Fig. III.14. Line voltage harmonic spectrum

As can be seen the three phase voltage generated in Fig (II.21), the waveform of the voltage is almost sinusoidal, which depicts the evolution of three-phase voltages as well their RMS. In this test, the amplitude is decrease from 400 V to 365V compared to the single unit.

In Fig (II.23), when the virtual impedance is enabled, the THD drops to only 0.38%.

Discussion

Table (III.1) shows the summary of the performance characteristics of the step response of the VSI system using both LQR with integral action and PI controller. It shows that the LQR control method has better performance as compared to the PI control method. From Table (III.1), it can see that LQR has the fastest rising time (T_r) of 1ms while PI has the rising time of 1.3 ms. In addition, PI has a larger value of settling time (T_s) of 12ms compared to the value of settling time for the LQR controller which is 1.5ms. From both of these characteristics, one can say that the LQR controller can respond faster than the PI controller. Furthermore, for the percent overshoot (%OS), LQR has 0% overshoots while the PI controller has a larger percent overshoot of 10%. The last characteristic is the steady-state error, (e_{ss}), where the both controllers have same performance.

	LQR	PI
THD	0.36	0.41
Overshoot	0	10%
Rising time	1ms	2.3ms
Settling-time	1.5ms	12ms
Static error %	0	≈0

Table III.1. Summary of the performance characteristics two DG units based islanded MG

All this means that the PI controller shows less performance as compared to the LQR controller. Secondly, the PI controller parameters need to be tuned to obtain an efficient response, which makes it tedious work whereas only 2 matrices need to be tuned in the case of the LQR controller. PID controller requires four feedback loops making the

computation more complex than the single control loop in the case of an LQR controller [63]. Thus, it can be concluded that the LQR controller has a better performance compared to the PI controller in controlling the proposed two parallel DG units.

III.7. Conclusion

In the first part of this chapter, linear state space model was established for two parallel DG units forming a microgrid in continuous time and discrete time and how to move between them. Then, based on continuous time system state-space representation, two methods namely pole placement and LQR, were detailed and were designed for two parallel DG units forming an islanded microgrid; the effect of integral action addition to the LQR is also studied.

Simulation results show that both controllers are capable to control the proposed microgid successfully. However, the LQR is able to produce better responses compared to the PI controller in terms of output, complexity, and, computation time.

Chapter IV

PIL Simulation of LQR Control of Parallel Inverters Based Islanded Microgrid

IV.1. Introduction

This chapter aims to present processor-in-the-loop (PIL) validation of LQR-I based control technique applied on autonomous microgrid. Processor-in-the-loop co-simulation is an essential stage that can be adopted either to check possible errors or to verify the feasibility and the performance of the generated code. This approach leads to test the numerical equivalence between the model and real computation, which is helpful in predicting the real behavior using just simple simulation. Hence, PIL is an effective technique that should be performed before passing to real time test due to some features including [67]-[68].

1. This technique allows designer to investigate specific problems with the algorithm execution in the embedded environment. In a way of example, it can be used to test whether the control algorithm fits within the execution time on the embedded processor;
2. Perform code execution profiling: this testing technique is useful to identify the most demanding operations inside the control loop;

3. PIL simulations may be performed to gain confidence and to check that the control algorithm performs as expected once it is physically running on the microcontroller unit (MCU);

4. Reprogramming without costly hardware repetition.

In this chapter, PIL concept will be used to validate the developed LQR algorithm for the adopted islanded microgrid. First, STM32F407 Discovery board will be introduced with some necessary definitions as well as the different stages necessary to co-simulate a given control system. Finally, the results of the LQR control simulation will be presented and commented on.

IV.2. STM32F4 DISCOVERY Board

The STM32F4DISCOVERY board is a low-cost and easy-to-use development kit that allows users to easily develop applications with the STM32F407VG high-performance microcontroller with the ARM® Cortex®-M4 32-bit core. It includes everything required either for beginners or for experienced users to get quickly started. Based on STM32F407VG, it includes an ST-LINK/V2 or ST-LINK/V2-A embedded debug tool, two ST-MEMS digital accelerometers, a digital microphone, one audio DAC with integrated class D speaker driver, LEDs, pushbuttons and a USB OTG micro-AB connector. For more specifications, refer to the STM32F4DISCOVERY and STM32F407VGT6 datasheets [69]-[70].

IV.3. PC Serial Communication Configuration

In order to power the board, the power is supplied by the USB connection with the PC using a USB cable 'type A to Mini-B'. It can also be powered for external application with a 5 V source.

The USB type A to Mini-B cable wished is USB TTL-232 cable - TTL-2303HX 3.3V (serial communication for STM32F4-Discovery board),

The microcontroller must be connected via USB and the use of the USB to TTL adapter is highly recommended. Without the serial adapter, the PIL data will be collected by the ST-LINK interface, which is much slower than the serial communication and makes it impractical.

For started the experience Follow the hardware setup instructions below:

Connect the ground pin of the TTL-2303HX cable to one of the GND pins on the STM32F4-Discovery board. then Connect the RX pin of the TTL-2303HX cable to the PA8 pin on the STM32F4-Discovery board after that Connect the TX pin of the TTL-2303HX cable to the PA9 pin on the STM32F4-Discovery board.

- Connect the USB side of the TTL-2303HX cable to your host computer, and power on your board by connecting the USB type A to Mini-B cable to the STM32F4-Discovery board.

Fig (IV.1) summarizes these instructions.

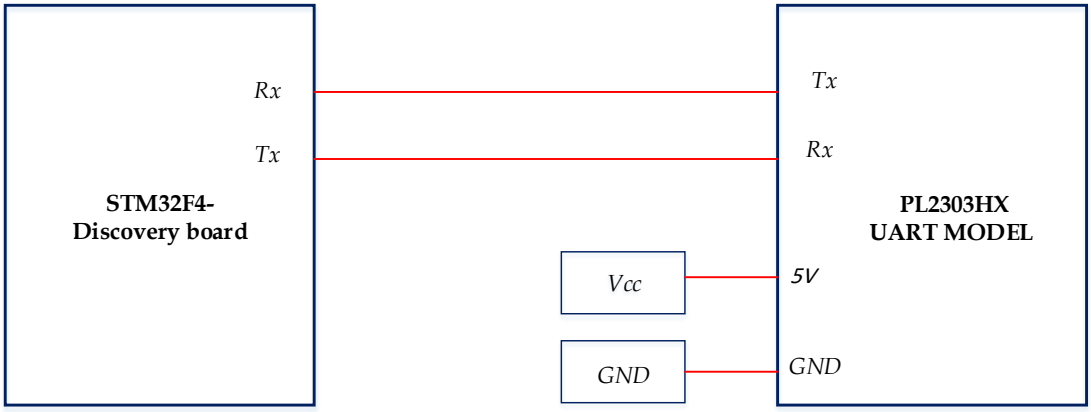

Fig. IV. 1. Hardware setup instructions

Finally, after changing the baud rate make sure to press the reset button on the STM32F4 Discovery board.

IV.4. Model Configuration for Code Generation

To install the package, execute the *install_waijung* MATLAB script file that is located inside the folder. Make sure the STM32F4 ST LINK is properly installed. Anyway, a warning message will be shown saying that the STM32F4 ST LINK could not be found. Just continue with the installation process, that message is an application bug.

The basic arrangement for a model that is planned to be executed on the STM32F4 consists of configuring the target and the Simulink solver. First, consolidation of all control algorithms of the VSI system in a subsystem simulation then open a blank Simulink model add UART setup, UART RX, UART TX and drop a Target Setup block from STM32F4 target. The parameters can be modified by double clicking on it also make sure to select the correct microcontroller unit and clock configuration. For this microcontroller, the configuration should look like Fig (IV.2).

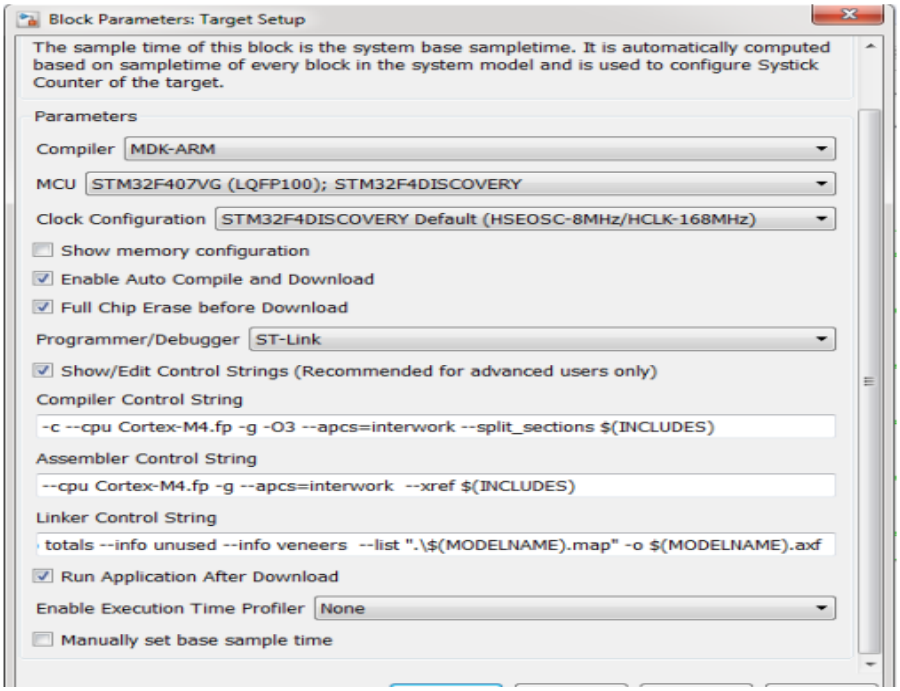

Fig. IV.2. Target setup configuration

IV.5. USART Communication Configuration

The STM32F4 has 4 USARTs and 2 UARTs. In this project, the communication with the microcontroller is always made through the USART1, which uses pins PB8 and PB9 for transmitting and receiving, respectively. The first step is the USART1 configuration as shown in Fig. (IV.3). Drag a USART Setup block into a configured model for code generation and select the module number 1.

Simulink will ask to close the window and reopen it to go on with the configuration. The baud rate has been set to 115200 bps, which is an acceptable speed for the sample time that is being managed [71].

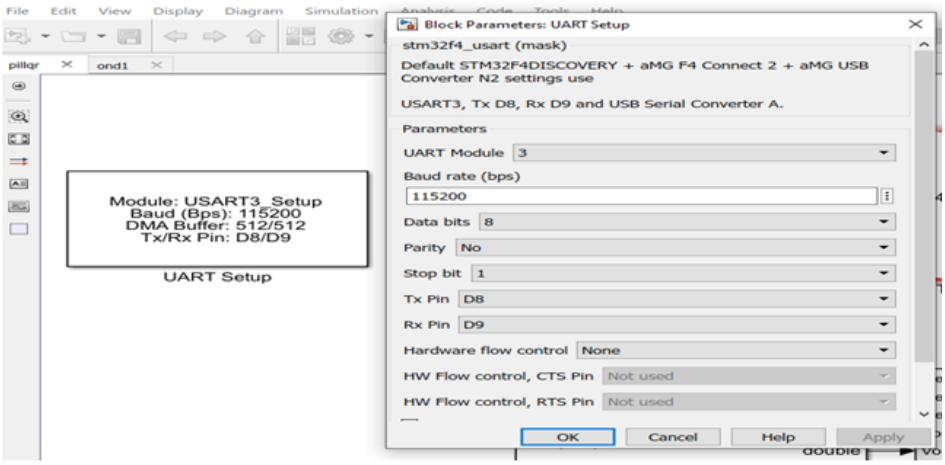

Fig. IV.3. USART Setup block configuration for using USART1 (Tx/Rx: D8/D9)

The software configuration for PC communication is very similar to USART communication. The main difference is that this algorithm will be executed on the PC, so another Simulink model will be needed. This model will not be compiled onto the board, so a default blank Simulink model will be used. The used blocks are found under the block group *Waijung Blockset*>> *Communication*>> *Host Serial Port*. They appear listed as in Fig (IV.4).

Fig. IV.4. Blocks for PC serial communication

Double click on the UART Tx and Rx and set the same UART model chosen before further set the Pocket mode to Binary and set the Number of data port to your need as displayed in Fig (IV.5).

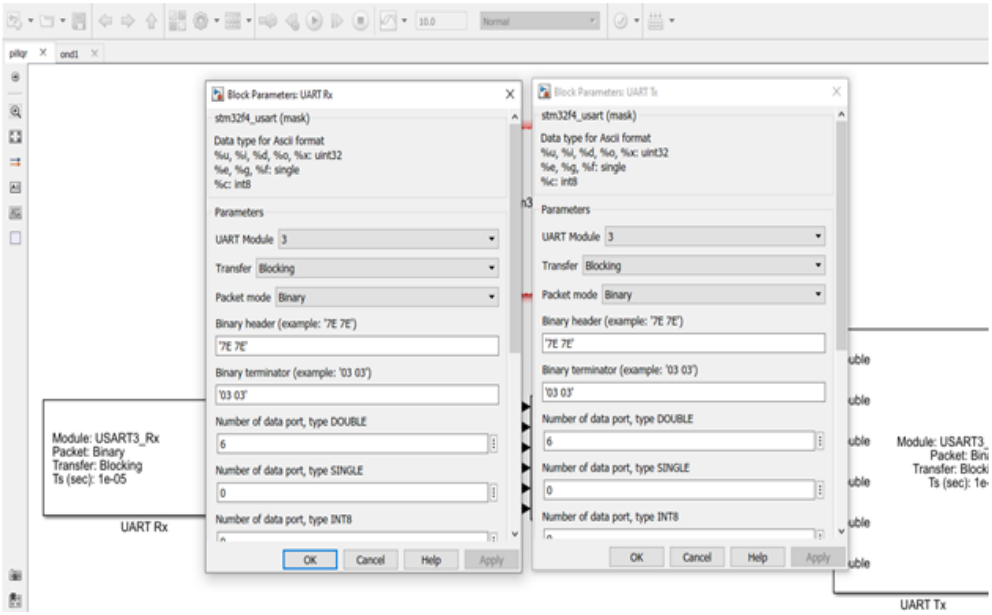

Fig. IV.5. UART Tx and Rx blocks configurations

The setup for these three blocks is analogous to the USART blocks. The only additional action is that the Host Serial Setup block must be configured to work with the corresponding port. To identify the port number of the serial adapter connected to the PC, open the device manager and look for the name of the device under PORTS (COM & LPT). The port number will appear in brackets at the end of the device as shown in Fig (IV.6).

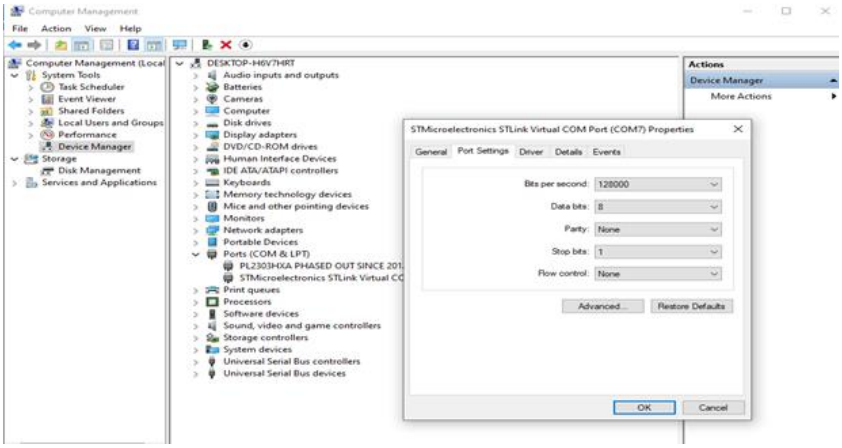

Fig. IV.6. Device manager showing that the USB-TTL adapter has been assigned the COM8

We will try to summarize all of the above in five steps by applying all this to VSI system based LQR controller on single unit and two units based microgrid.

IV.6. PIL Simulation Steps

IV.6.1. First Step: Testing the Model in MATLAB/Simulink

Model plant and its control are created and simulated in the same Matlab/Simulink environment as shown in Fig (IV.7).

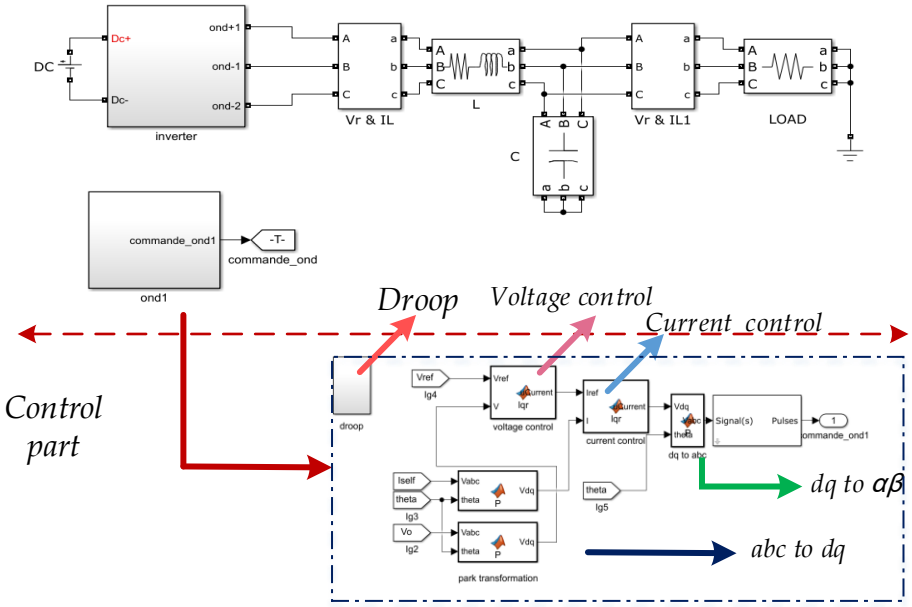

Fig. IV.7. Simulink model of VSI single unit based on LQR controllers

IV.6.2. Second Step: Dividing the Model into Two Parts

Taking the power part as target included in Matlab, while taking the control part as host included in the STM32F407 board. Fig. (IV.8) shows the model divided into two main parts in two-separated Simulink model: Control and power parts.

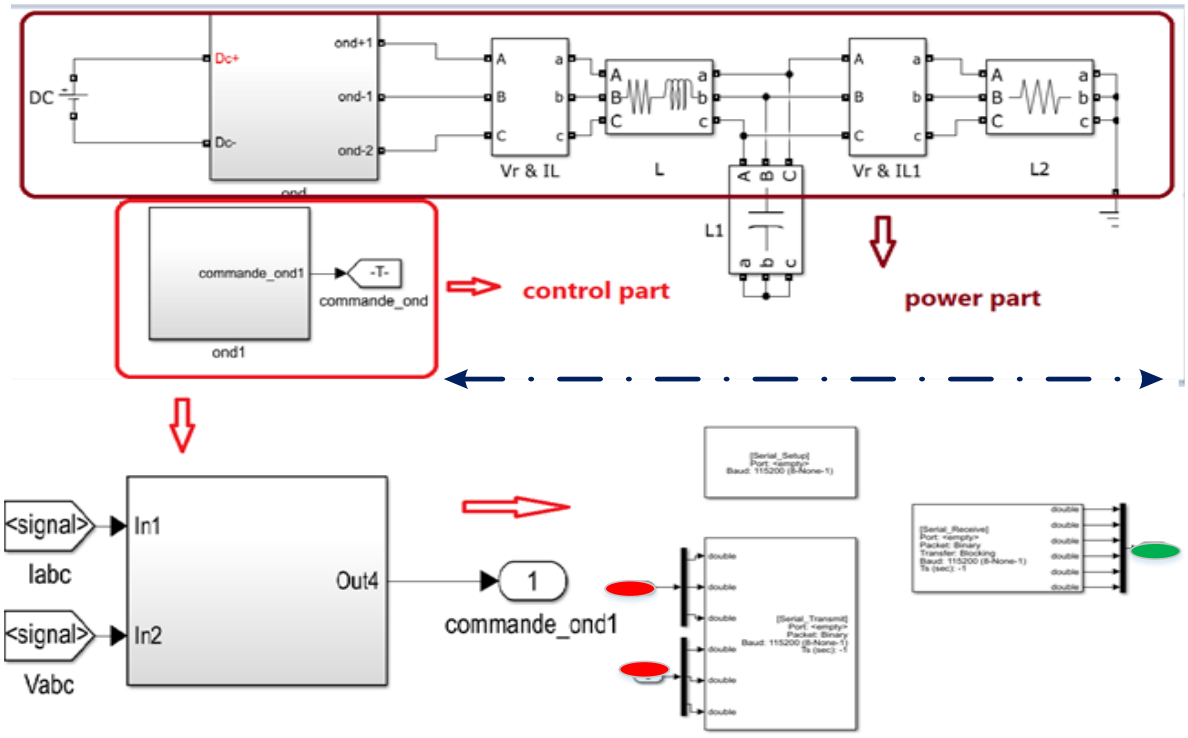

Fig. IV.8. Simulink model divided in two parts, power part and control part

- **Power part**: inverter, LC filter, and load.
- **Control part**: LQR controller.

The output-ports of the power part, which are the input-ports of the control part and which represents:

- The red ports are connected to UART RX block ports and green ports are connected to UART TX blocks ports in the Simulink Target part, respectively. Inversely, these red ports are connected to Host Serial TX block ports and blue ports are connected to Host Serial RX Block ports in the Simulink host part, respectively.

- The STM32F407 board, which contains the controller model, is connected to computer, which contains the plant model. This plant model behaves as if it is in a real environment and send the following values: I_{iabc}, V_{oabc}

IV.6.3. Third Step: UART Configuration of the Control Part in Simulink and Generating C Code

Fig (IV.9) shows the configuration of the system control part (target). The generated C code is implemented on the STM32F407 board. The UART/Rx block is configured to receive the values from the controls part (target), and UART/Tx Block is configured to send the instruction to it.

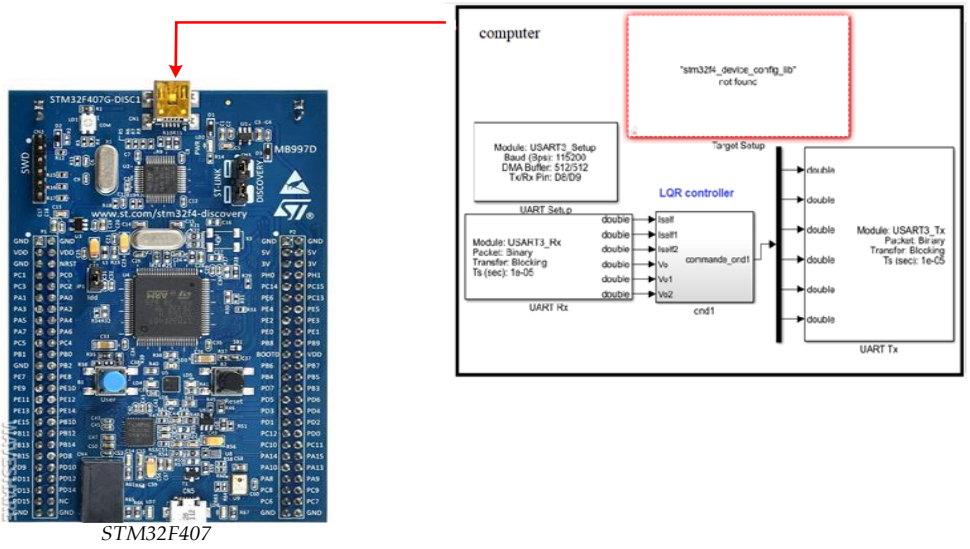

Fig. IV.9. UART configuration of the control part in Simulink

IV.6.3.1. Waijung Track Build Process

• To generate the C code of both controllers from the control part as well its implementation on the STM32F407-VG board, it is simply required to click on the build process button available on Simulink. The Waijung track building process window is then displayed as shown in Fig (IV.10).

• From Fig (IV.10), the Waijung Track Build process indicates the result of each operation.

All green indicates "success"; all red indicates "Failure." It should be pointed out that this Simulink window with all related configuration is needed just for the generation of the C code as well as its implementation on the embedded board. This Simulink window will no longer be necessary in the rest of PIL testing steps, and it can be switched off.

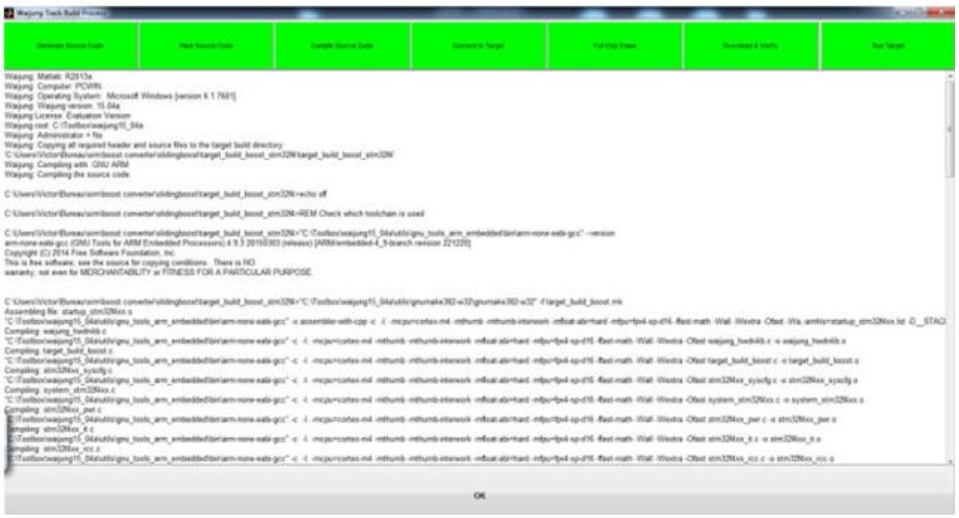

Fig. IV.10. Build process window

IV.6.4. Fourth Step: Host Serial Configuration of the Power Part in Simulink and Connection Layout

• The TTL-2303HX USB/UART converter board is proposed as an external communication interface instead of the ST-LINK communication interface.

• The both boards are connected from their USB (type Mini B) to the computer USB (type A) as shown in Fig (IV.11).

• Pin D8/D9 (which are set at Tx/Rx) of the STM32F407 board is connected to Rx/Tx of the TTL-2303HX board, respectively. GND pins of both boards are connected together as shown in Fig (IV.11).

• Host Serial Tx Block is configured to receive the values from plant (host).

• Host Serial Rx Block is configured to send the instruction to it.

• The C code is implemented on STM32F407 board that acting as controller.

- Simulation is run from Simulink (Host PC)

If any glitches occur during the PIL testing, it will easily go back to controllers for making necessary changes, before generating the C code and implementing it again on the embedded board. This operation can be repeated many times until simulation results are satisfying [72].

IV.6.5. Fifth Step: Running the Co-Simulation

- Running the plant model on MATLAB/SIMULINK as usual. The host computer is connected to the target controller.

- The embedded controller interacts with the plant Simulink model through various I/O channels.

- A sample time value should be chosen accurately so as not to diverge the simulation. The co-simulation results are displayed on Simulink scopes

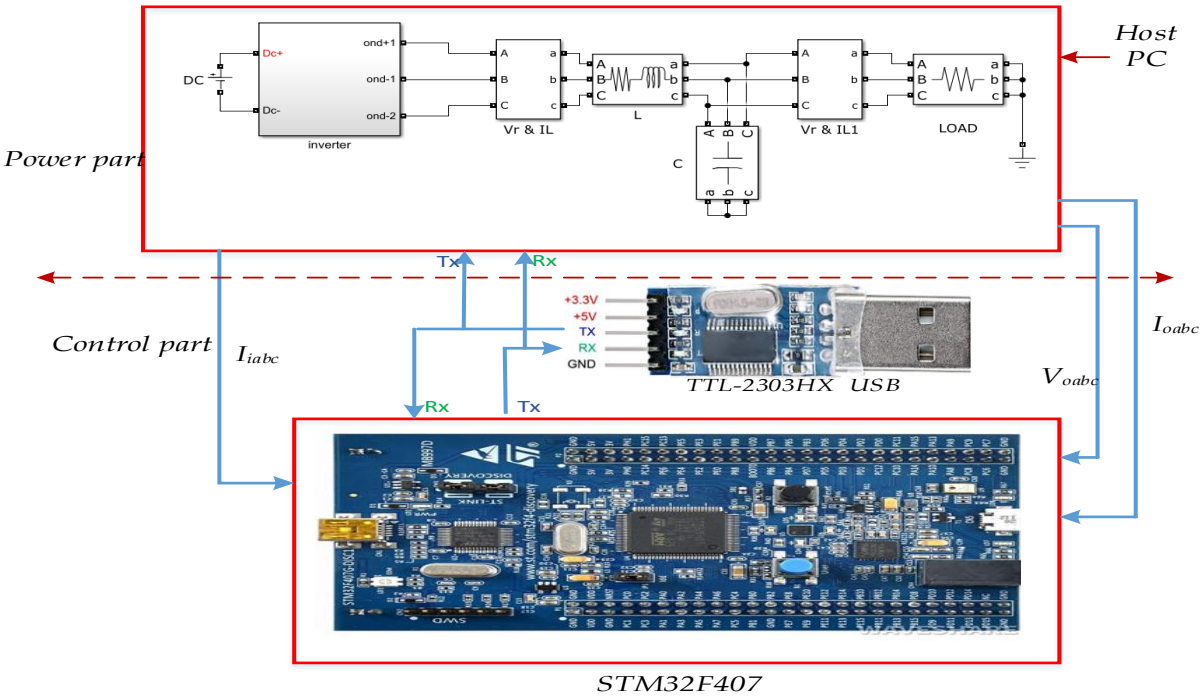

Fig. IV.11. Host serial configuration of the power part in Simulink and Connection Layout between STM32F407 and TTL-2303HX boards

IV.7.PIL Simulation Results and Discussions

IV.7.1.PIL Control of a Single DG Unit

In the following, the system control is tested at both single DG unit and two DG units. The co-simulation is performed using the same parameters listed in Appendix A.

Fig. (IV.11) presents the block diagram of process in the loop simulation of LQR control of single unit VSI system based microgrid.

The first scenario is aimed to test the performance of the LQR control using PIL simulation in steady state. As shown in Fig. (IV.12,) the controller is able to track the voltage reference keeping the tracking error percentage near to zero. The waveform of the voltage is sinusoidal, and the ratio of Total Harmonic Distortion THD is 0.80% as seen in Fig. (II.13), which is within the MG standards.

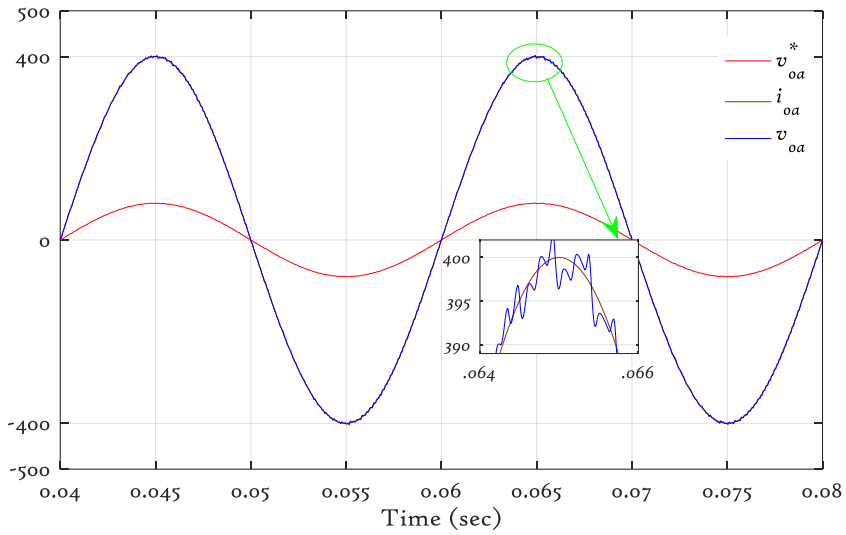

Fig. IV.12. Line current and voltage with its reference

The second scenario is aimed to test the performance of the LQR control using PIL simulation when a step-change in the voltage reference is implemented. The evolution of three-phase voltages as well as their RMS value is illustrated in Fig. (IV.14). It can be seen that the LQR controller rejects the disturbance and continue tracking the reference within

considered time. The settling time in which the signals recover after the disturbance is 7ms, and it is noticeable that there is no overshoot.

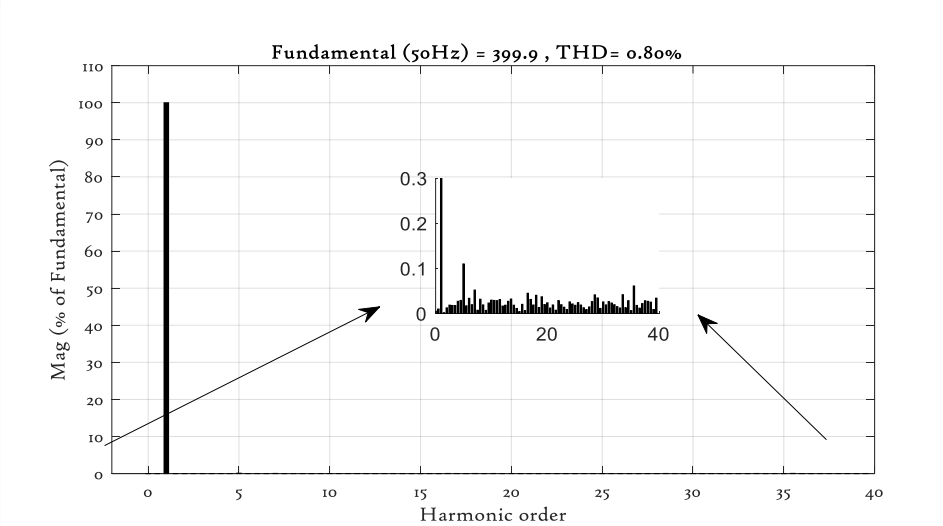

Fig. IV.13. Line voltage harmonic spectrum

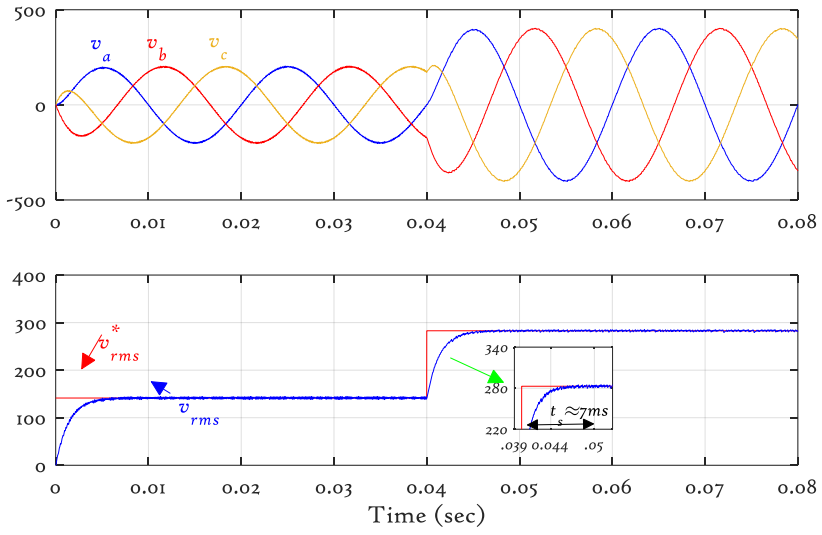

Fig. IV.14. Three-phase voltage for a reference step change and its RMS value

IV.7.2. Droop Control Without Virtual Impedance of Parallel DG Units

Fig. (IV.15) shows the block diagram of process in the loop simulation of the droop control of two parallel unit VSI system based microgrid. A simple difference between the parameters of DGs causes large disturbances and the system become instable. Fig (IV.16)

shows the shared active and reactive powers of the two DGs. Fig (IV.17) gives an idea about the emerged circulating current and its effect on inverters' currents.

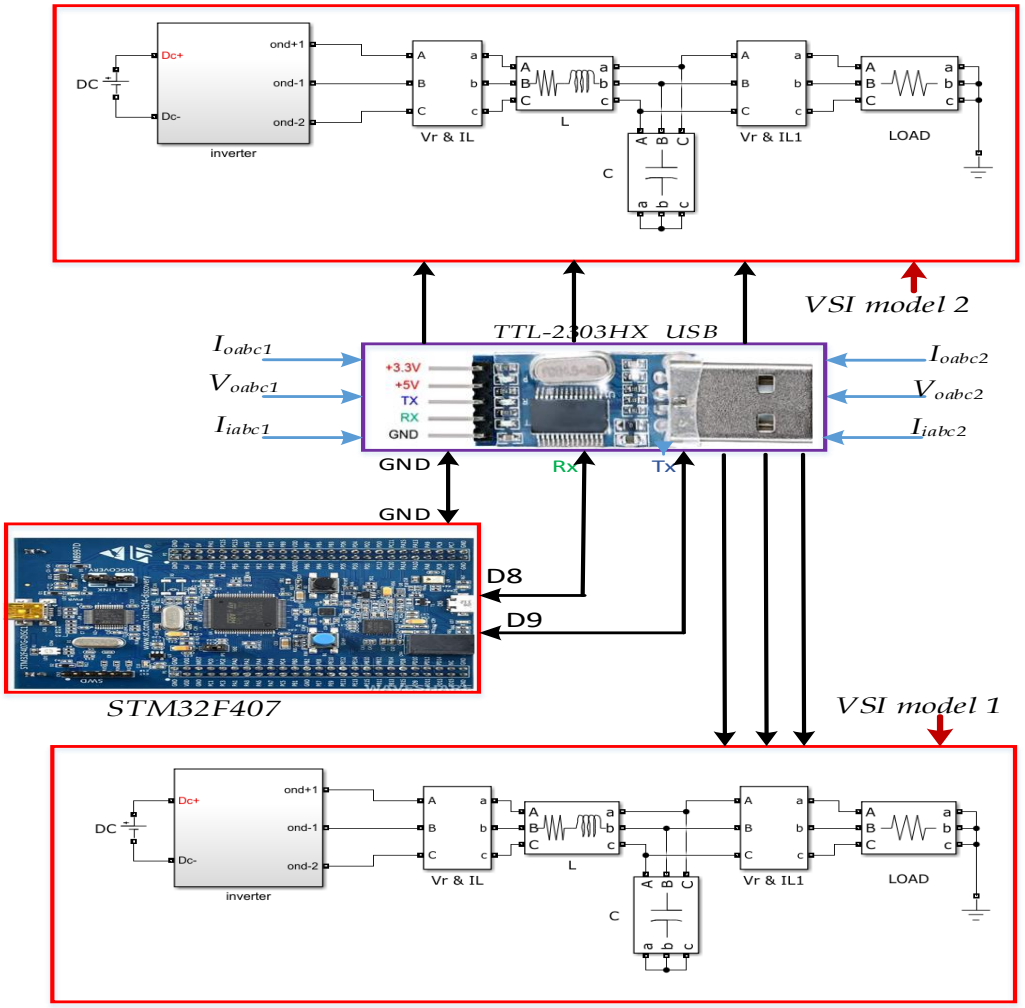

Fig. IV.15. PIL simulation of two DGs units based microgrid

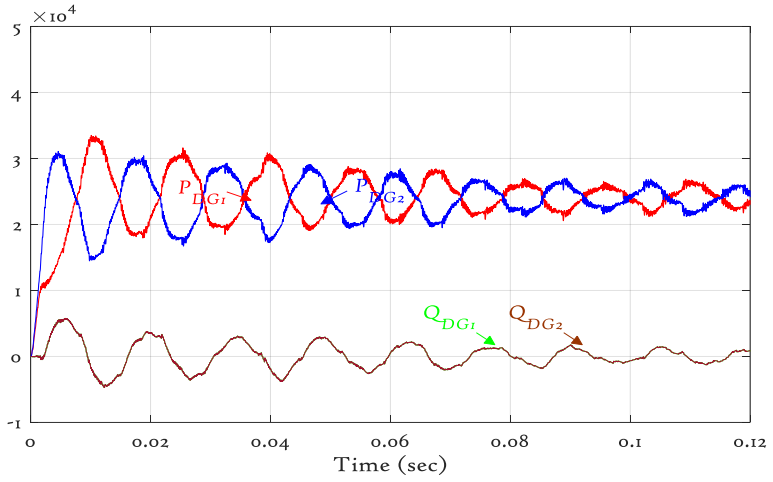

Fig. IV.16. Two DGs active and reactive powers sharing

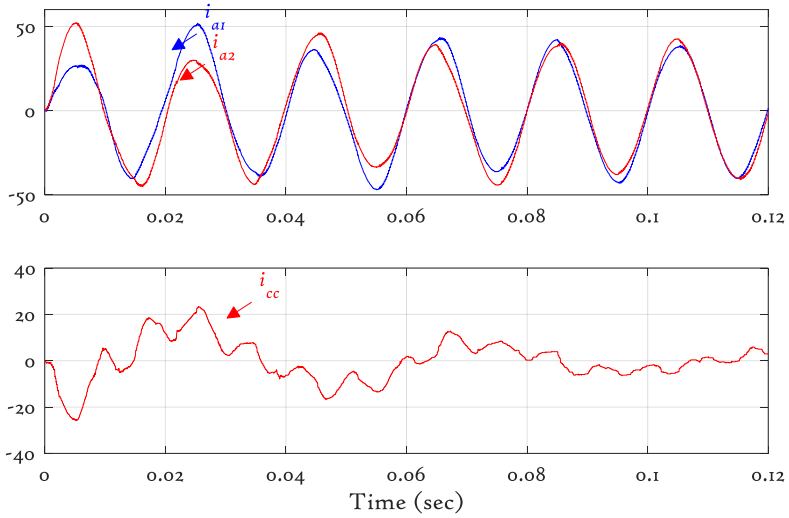

Fig. IV.17. Current waveforms of two DGs and the resulting circulating current

IV.7.3. Droop Control With Virtual Impedance of Parallel DG Units

Fig. (IV.18) shows that the power is well shared even in the presence of a difference in impedances, where each unit exports half of the total power amount. It can be seen that even though the shared power is well shared, it is yet surrounded by much ripples.

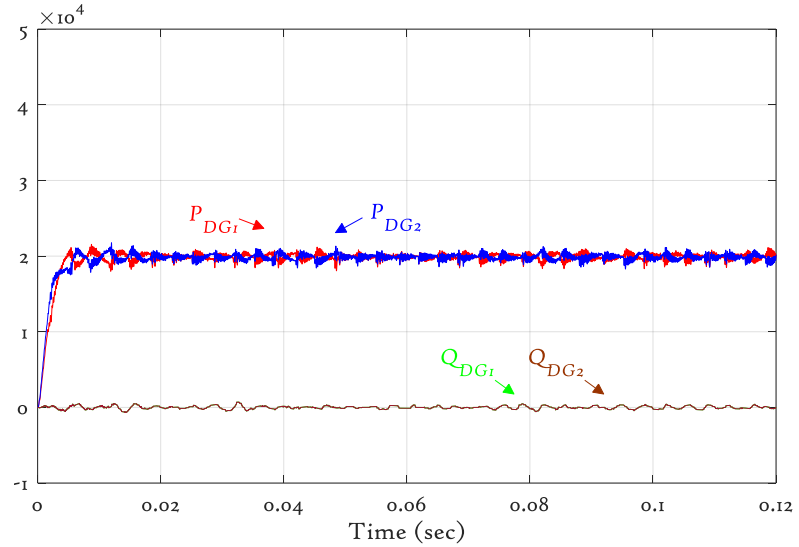

Fig. IV.18. Active and reactive powers sharing between the two DGs controlled by droop control with virtual impedance

Fig. (IV.19) confirms that circulating current is reduced, which makes the line currents of

both inverters balanced. It is worth mentioning that the droop control with virtual impedance method drops the three-phase voltage in order to eliminate the circulating currents.

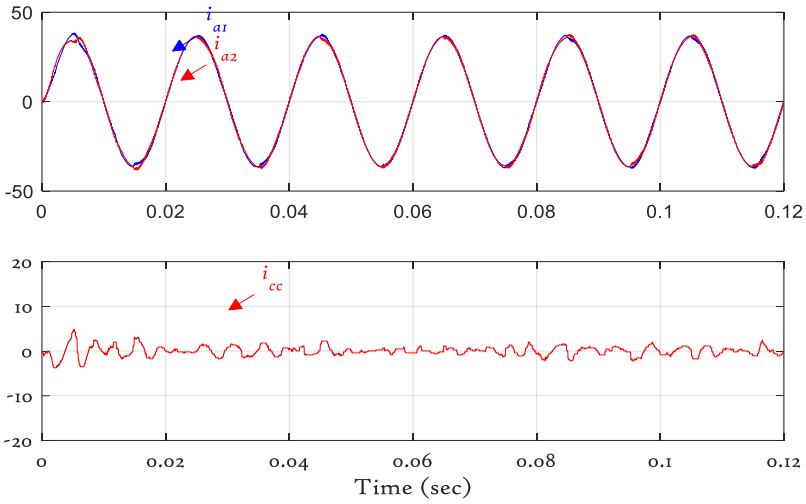

Fig. IV.19. Current waveforms of the two DGs controlled by droop control with virtual impedance

Fig. (IV.20) illustrates the three-phase voltages obtained by PIL simulation. From this figure and after a short transient period, the voltages waveforms are almost sinusoidal. This figure depicts also the evolution of the voltage RMS, in which the amplitude is decreased from 400 V to 365 V compared to the single unit.

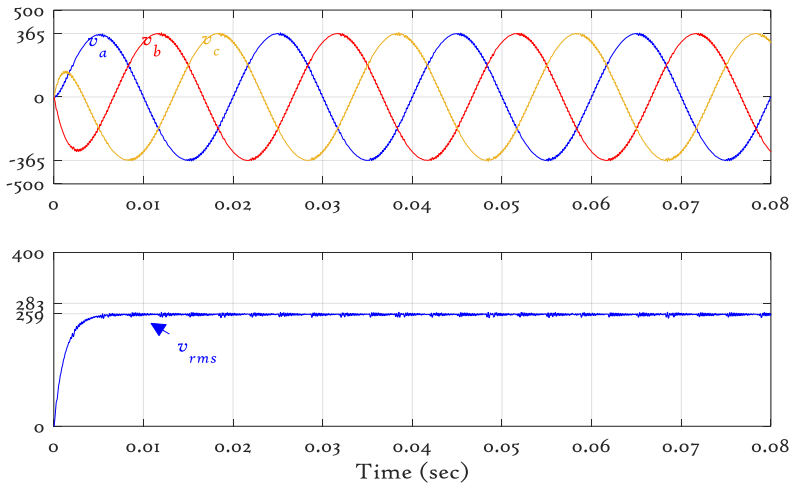

Fig. IV.20. Three-phase voltage and its RMS value

From Fig. (IV.21), with the incorporation of virtual impedance in the control action the THD dropped to 1.48%.

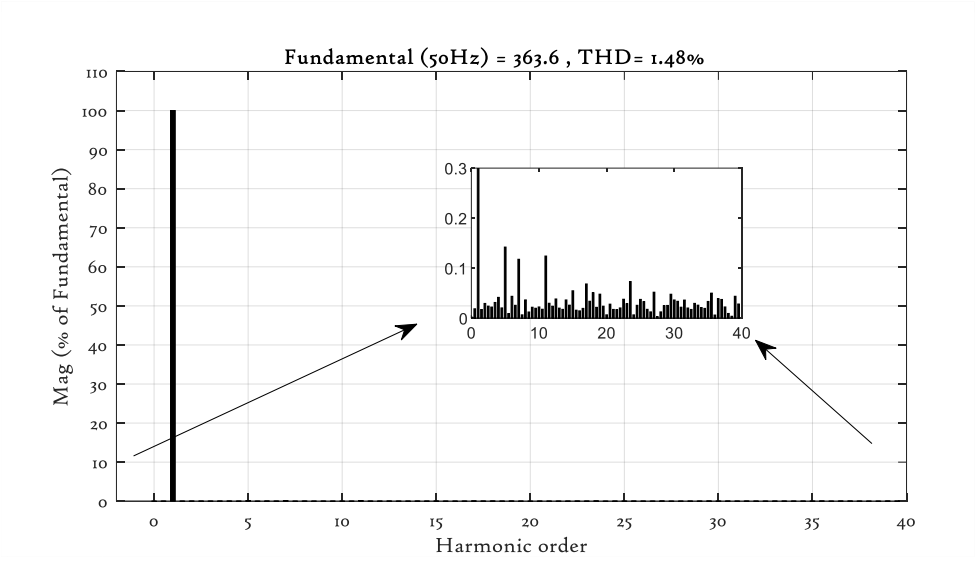

Fig. IV.21. Line voltage harmonic spectrum

The interesting finding is that the results of LQR control of two parallel VSIs based islanded microgrid co-simulation using PIL are in great consistency with simulation results.

IV.8. Conclusion

In this chapter, the co-simulation of LQR control of two parallel VSIs feeding an islanded load is presented. For this, the different steps to perform a PIL co-simulation with MATLAB using the STM32F4 development board are deeply detailed. After that, the PIL simulation is used to validate and check the performance of one VSI and two parallel VSIs controlled by LQR approach. The obtained results confirm that there is no significant difference in performance between running simulation in normal mode and PIL simulation. In addition to that, it can be concluded that the LQR approach is able to control the parallel VSIs system based microgrid in real time implementation.

General Conclusion

The main purpose of this work is to propose an effective LQR control of parallel inverters system based islanded microgrid. In this context, droop control with or without virtual impedance was studied and investigated, and validated by PIL co-simulation tools using the STM32F407VG discovery board. Also, the effectiveness of the proposed control method was highlighted trough a comparative study with conventional PI controller.

In the first chapter, we provide an overview of the different control techniques applied to Decentralized generating units in a microgrid. Conventional central generation systems were introduced before turning to distributed generation. Distributed generating units make up the effect of the appropriate solution to meet the energy requirements effectively and make it face the economic and environmental obstacles imposed by electricity production. These units can operate in island mode to supply a range of local loads or in connected mode to support the main grid for this, hierarchical control is often implemented. This control includes a zero-level control, a Primary control, secondary control, and tertiary control,

In the second chapter a droop control based on PI controllers was proposed to control two parallel inverters based islanded microgrid. Theoretical analysis and simulation were presented to clarify the effectiveness of the proposed control method and to show the behavior of the classical control facing disturbances. From this, it concluded that the droop control can significantly improve the asymmetric power sharing caused by different transmission line impedances. But this control in the absence of virtual impedance does not make it possible to ensure good power-sharing Thus, adding it has contributed to the stability of the system

In the third chapter, a droop control based on LQR controllers with integral action was adopted to control the proposed autonomous microgrid composed of two parallel distributed generation units. Compared to the PI controller, the LQR with integral action gives a better performance by reducing the steady-state error and minimizing the overshoot and gives high power quality of the output voltage with lesser ratio of THD. it makes the error between the output and the reference objectives close to zero, which means better transient response, reduced tracking error, and reduced power and current ripples. This approach help remedy problems related power quality in a single distributed generator unit

In the fourth chapter, a PIL simulation of the LQR control of two parallel inverters was performed using the STM32F407VG discovery board. The obtained co-simulations result of the two VSIs based islanded microgrids confirm the ability of the linear optimal control in enhancing the overall system performance. From this finding, one can infer that the proposed controller is ready to be implemented in real-time situation.

There are many possibilities and courses in which this work could guide to. Suggestions for future works include:

- Investigation of other control strategies such as predictive control and nonlinear control,
- Expansion of the microgrid to include renewable energy resources, like solar and wind power in addition to the batteries,
- Develop droop control strategies to ensure power-sharing between different distributed generators,
- Develop a systems stabilization strategy in distributed generation systems, including autonomous microgrids

APPENDIX A

Parameter	Value
DC voltage	1000 V
Load resistor	5 Ω
Filter inductance	500 μH
Filter capacitor	$365.5\mu F$
Filter resistor	0.001 Ω
Voltage reference	400 V
Frequency	50 Hz
PI voltage gains K_{pv}, K_{iv}	0.8 ; 600
PI current gains K_{pi}, K_{ii}	10 ; 2000
Switching frequency	10 kHz

Table (A.1): VSI System Parameters

Bibliography

[1] C. Ralvenius, "Development of Wind Power Laboratory Setup," *CODEN LUTEDXTEIE*, 2011.

[2] F. Blaabjerg, Z. Chen, and S. B. Kjaer, "Power electronics as efficient interface in dispersed power generation systems," *IEEE Trans. Power Electron.*, vol. 19, no. 5, pp. 1184–1194, 2004.

[3] M.A. DERICHE1, A. HAFAIFA2, K. MOHAMMEDI1, "Overview of PV Power Plants Projects in Algeria".

[4] P. Kanjiya and V. Khadkikar, "Enhancing power quality and stability of future smart grid with intermittent renewable energy sources using electric springs," 2013, pp. 918–922.

[5] E. J. Coster, J. M. Myrzik, B. Kruimer, and W. L. Kling, "Integration issues of distributed generation in distribution grids," *Proc. IEEE*, vol. 99, no. 1, pp. 28–39, 2010.

[6] F. Z. Peng, "Editorial special issue on distributed power generation," *IEEE Trans. Power Electron.*, vol. 19, no. 5, pp. 1157–1158, 2004.

[7] J. Wang, X. Li, and X. Qiu, "Review on the research of power system containing distributed generation device," *Autom. Electr. Power Syst.*, vol. 24, pp. 90–97, 2005.

[8] W. R. Issa, M. A. Abusara, and S. M. Sharkh, "Control of transient power during unintentional islanding of microgrids," *IEEE Trans. Power Electron.*, vol. 30, no. 8, pp. 4573–4584, 2014.

[9] J. C. Vasquez Quintero, *Decentralized control techniques applied to electric power distributed generation in microgrids*. Universitat Politècnica de Catalunya, 2009.

[10] A. Colmenar-Santos, C. Reino-Rio, D. Borge-Diez, and E. Collado-Fernández, "Distributed generation: A review of factors that can contribute most to achieve a

scenario of DG units embedded in the new distribution networks," *Renew. Sustain. Energy Rev.*, vol. 59, pp. 1130–1148, 2016.

[11] N. Khefifi, "Élaboration de stratégies de contrôle-commande basées sur la passivité pour le pilotage d'un micro-réseau de génération décentralisée de type AC en mode autonome," 2021.

[12] "E. I. Amoiralis, M. A. Tsili, et A. G. Kladas, « Power Transformer Economic Evaluation in Decentralized Electricity Markets », IEEE Transactions on Industrial Electronics, vol. 59, no 5, p. 2329-2341, mai 2012, doi: 10.1109/TIE.2011.2157291".

[13] P. Kanjiya and V. Khadkikar, "Enhancing power quality and stability of future smart grid with intermittent renewable energy sources using electric springs," 2013, pp. 918–922.

[14] Y.-S. Kim, E.-S. Kim, and S.-I. Moon, "Frequency and voltage control strategy of standalone microgrids with high penetration of intermittent renewable generation systems," *IEEE Trans. Power Syst.*, vol. 31, no. 1, pp. 718–728, 2015.

[15] A. Muhammad, A. Kalwar, and K. Mekhilef, "Review: uninterruptible power supply (UPS) system," *Renew. Sustain. Energy Rev.*, vol. 58, pp. 1395–1410, 2016.

[16] S. Abdelhakim, "Docteur 3ème Cycle en Automatique".

[17] Z. Yang, C. Wang, and Y. Che, "A small-scale microgrid system with flexible modes of operation," *Autom. Electr. Power Syst.*, vol. 33, no. 14, pp. 89–92, 2009.

[18] T. L. Vandoorn, B. Meersman, J. D. De Kooning, and L. Vandevelde, "Analogy between conventional grid control and islanded microgrid control based on a global DC-link voltage droop," *IEEE Trans. Power Deliv.*, vol. 27, no. 3, pp. 1405–1414, 2012.

[19] A. Micallef, M. Apap, C. Spiteri-Staines, and J. M. Guerrero, "Secondary control for reactive power sharing in droop-controlled islanded microgrids," 2012, pp. 1627–1633.

[20] C. Marinescu and I. Serban, "Robust frequency control for a wind/hydro autonomous microgrid," 2011, pp. 1–6.

[21] N. Intharasomchai and K. Chayakulkheeree, "Steady State Primary Frequency Estimation for Microgrid Transferring Mode Using Distributed Slack Bus Load Flow Analysis," 2020, pp. 101–104.

[22] P. Piagi and R. H. Lasseter, "Autonomous control of microgrids," 2006, pp. 8-pp.

[23] N. Pogaku, M. Prodanovic, and T. C. Green, "Modeling, analysis and testing of autonomous operation of an inverter-based microgrid," *IEEE Trans. Power Electron.*, vol. 22, no. 2, pp. 613–625, 2007.

[24] J. M. Guerrero, "Microgrids: Integration of distributed energy resources into the smart-grid," 2010, pp. 4281–4414.

[25] J. M. Guerrero, J. C. Vásquez, J. Matas, J. L. Sosa, and L. G. De Vicuña, "Parallel operation of uninterruptible power supply systems in microgrids," 2007, pp. 1–9.

[26] J. C. Vasquez Quintero, *Decentralized control techniques applied to electric power distributed generation in microgrids*. Universitat Politècnica de Catalunya, 2009.

[27] "Y.-S. Kim, E.-S. Kim, et S.-I. Moon, « Frequency and Voltage Control Strategy of Standalone Microgrids With High Penetration of Intermittent Renewable Generation Systems », IEEE Transactions on Power Systems, vol. 31, no 1, p. 718-728, janv. 2016, doi: 10.1109/TPWRS.2015.2407392."

[28] J. M. Guerrero, J. C. Vasquez, J. Matas, M. Castilla, and L. G. de Vicuña, "Control strategy for flexible microgrid based on parallel line-interactive UPS systems," *IEEE Trans. Ind. Electron.*, vol. 56, no. 3, pp. 726–736, 2008.

[29] K. Visscher and S. W. H. De Haan, "Virtual synchronous machines (VSG's) for frequency stabilisation in future grids with a significant share of decentralized generation," 2008, pp. 1–4.

[30] A. Bidram, V. Nasirian, A. Davoudi, and F. L. Lewis, *Cooperative synchronization in distributed microgrid control*. Springer, 2017.

[31] A. E. M. Bouzid, "Élaboration d'une méthode de contrôle pour améliorer la robustesse d'un micro réseau électrique," 2017.

[32] P. C. Loh, M. J. Newman, D. N. Zmood, and D. G. Holmes, "A comparative analysis of multiloop voltage regulation strategies for single and three-phase UPS systems," *IEEE Trans. Power Electron.*, vol. 18, no. 5, pp. 1176–1185, 2003.

[33] W. I. S. Qutaina, "Modeling and Control of Shunt Active Power Filter in Medium Voltage applications." May 2019.

[34] A. Ovono Zue, "Conception et simulation de systèmes d'interfacage de l'énergie photovoltaique au réseau de distribution opérationnels 24 h par jour," 2007.

[35] "R. MUSA, 'Improving the safety operation of three-phase shunt active filter', PhD Thesis, École de technologie supérieure, 2017.".

[36] "S. Ponnaluri and A. Brickwedde. 'Generalized system design of active filters.' Power Electronics Specialists Conference, 2001. PESC. 2001 IEEE 32nd Annual. Vol. 3. IEEE, 2001.".

[37] J. Xu, S. Xie, L. Huang, and L. Ji, "Design of LCL-filter considering the control impact for grid-connected inverter with one current feedback only," *IET Power Electron.*, vol. 10, no. 11, pp. 1324–1332, 2017.

[38] K. Chatterjee, B. Fernandes, and G. K. Dubey, "An instantaneous reactive volt-ampere compensator and harmonic suppressor system," *IEEE Trans. Power Electron.*, vol. 14, no. 2, pp. 381–392, 1999.

[39] F. Sadeque, J. Benzaquen, A. Adib, and B. Mirafzal, "Direct phase-angle detection for three-phase inverters in asymmetrical power grids," *IEEE J. Emerg. Sel. Top. Power Electron.*, vol. 9, no. 1, pp. 520–528, 2020.

[40] B. Wang and J. J. Cathey, "DSP-controlled, space-vector PWM, current source converter for STATCOM application," *Electr. Power Syst. Res.*, vol. 67, no. 2, pp. 123–131, 2003.

[41] R. Rajendran and N. Devarajan, "Analysis and FPGA realization of a pulse width modulator based on voltage space vectors," *Int. J. Comput. Appl.*, vol. 2, no. 6, pp. 46–51, 2010.

[42] M. D. G. Pagar and S. Khule, "Implementation of Space Vector PWM for Hybrid DSTATCOM," 2017.

[43] P. Piagi and R. H. Lasseter, "Autonomous control of microgrids," 2006, pp. 8-pp.

[44] P. C. Loh and D. G. Holmes, "Analysis of multiloop control strategies for LC/CL/LCL-filtered voltage-source and current-source inverters," *IEEE Trans. Ind. Appl.*, vol. 41, no. 2, pp. 644–654, 2005.

[45] J. Selvaraj and N. A. Rahim, "Multilevel inverter for grid-connected PV system employing digital PI controller," *IEEE Trans. Ind. Electron.*, vol. 56, no. 1, pp. 149–158, 2008.

[46] mohamed said OUAHABI and lamouri AISSAT, "SIL and PIL Simulation of Second Order SMC of HVDC Systems," Université de M'sila, 2019.

[47] M. BOUZIDI, "COMMANDES NON LINEAIRES D'UN REDRESSEUR PWM TRIPHASE," 2009.

[48] Q.-C. Zhong and Y. Zeng, "Universal droop control of inverters with different types of output impedance," *IEEE Access*, vol. 4, pp. 702–712, 2016.

[49] Y. Li, "Power management of power electronics interfaced low-voltage microgrid in islanding operation," 2010.

[50] IEEE Standard Association, "IEEE Std. 1547-2018," *Stand. Interconnect. Interoperability Distrib. Energy Resour. Assoc. Electr. Power Syst. Interfaces*, vol. 10, 2018.

[51] J. M. Guerrero, L. G. De Vicuna, J. Matas, M. Castilla, and J. Miret, "A wireless controller to enhance dynamic performance of parallel inverters in distributed generation systems," *IEEE Trans. Power Electron.*, vol. 19, no. 5, pp. 1205–1213, 2004.

[52] J. M. Guerrero, L. G. de Vicuna, J. Matas, J. Miret, and M. Castilla, "Output impedance design of parallel-connected UPS inverters," 2004, vol. 2, pp. 1123–1128.

[53] P. Zhang, H. Zhao, H. Cai, J. Shi, and X. He, "Power decoupling strategy based on 'virtual negative resistor'for inverters in low-voltage microgrids," *IET Power Electron.*, vol. 9, no. 5, pp. 1037–1044, 2016.

[54] M. A. Abusara, S. M. Sharkh, and J. M. Guerrero, "Improved droop control strategy for grid-connected inverters," *Sustain. Energy Grids Netw.*, vol. 1, pp. 10–19, 2015.

[55] M. Pape, "Design of a flexible and modular test bed for studies on islanded microgrids," 2015.

[56] H. Akagi, E. H. Watanabe, and M. Aredes, *Instantaneous power theory and applications to power conditioning*. John Wiley & Sons, 2017.

[57] D. Le Deaut, "Simplified sallen-key low-pass filter circuit," Feb. 2011.

[58] J. M. Guerrero, "Microgrids: Integration of distributed energy resources into the smart-grid," 2010, pp. 4281–4414.

[59] M. Ramli, M. Rahmat, and M. Najib, "Design and modeling of integral control state-feedback controller for implementation on servomotor control," presented at the 6th WSEAS International Conference on circuits, systems, electronics, control & signal processing, Cairo, Egypt, 2007.

[60] N. S. Nise, "Control system engineering, john wiley & sons," *Inc N. Y.*, 2011.

[61] "Download citation of Commande Avancée (contrôle optimal et prédictif) Master Automatique." https://www.researchgate.net/publication/337305272_Commande_Avancee_controle_optimal_et_predictif_Master_Automatique/citation/download (accessed Jun. 07, 2022).

[62] G. H. Valencia-Rivera, L. R. Merchan-Villalba, G. Tapia-Tinoco, J. M. Lozano-Garcia, M. A. Ibarra-Manzano, and J. G. Avina-Cervantes, "Hybrid LQR-PI control for microgrids under unbalanced linear and nonlinear loads," *Mathematics*, vol. 8, no. 7, p. 1096, 2020.

[63] P. Saraf, M. Gupta, and A. M. Parimi, "A Comparative Study Between a Classical and Optimal Controller for a Quadrotor," 2020, pp. 1–6.

[64] M. Islam, M. Okasha, E. Sulaeman, S. Fatai, and A. Legowo, "Performance evaluation of linear quadratic regulator and linear quadratic gaussian controllers on quadrotor platform," *Int. J. Recent Technol. Eng.*, vol. 7, pp. 191–195, 2019.

[65] N. Hamaizia, "Commande optimale d'un onduleur monophasé sous l'environnement Matlab/Simulink," 2017.

[66] S. Boyd, "Linear quadratic regulator: Discrete-time finite horizon, lecture notes," 2008.

[67] M. Youcef, "Conception et Réalisation d'un Système de Contrôle et de Communication à base de la Carte à Microcontrôleur STM32F7." Université Kasdi Merbah Ouargla, May 2016.

[68] B. E. youcefa, "Etude de l'association d'un filtre actif parallèle à des sources d'énergie renouvelables." UNIVERSITE DJILLALI LIABES DE SIDI-BEL-ABBES, 03 2020.

[69] S. Motahhir, A. El Ghzizal, S. Sebti, and A. Derouich, "MIL and SIL and PIL tests for MPPT algorithm," *Cogent Eng.*, vol. 4, no. 1, p. 1378475, 2017.

[70] T. Menzies and A. Marcus, "Automated severity assessment of software defect reports," 2008, pp. 346–355.

[71] C. O. Moreira, "Rapid Control Prototyping Using STM32 Microcontroller." Research Bachelor Thesis, Institut fur Elektrische Informationstechnik, Technische Universitat Clausthal, Clausthal-Zellerfeld, Germany., Aug. 28, 2015.

[72] B. Fekkak, M. Menaa, A. Loukriz, and A. Kouzou, "Control of grid-connected PMSG-based wind turbine system with back-to-back converters topology using a new PIL integration method," *Int. Trans. Electr. Energy Syst.*, vol. 31, no. 6, p. e12882, 2021.

Abstract:

The growing use of parallel distributed generators (DGs) based microgrid helps in integrating local renewable energy sources by using governed power inverters. In this thesis, we have focused on developing DGs based autonomous microgrid to address issues related to power quality problems and power sharing between several units especially under disturbances created by load change. In this regards, linear quadratic regulator (LQR) based droop control equipped with an integral action has been proposed to contribute in enhancing power quality of autonomous microgrid based on distributed generators and helping in ensuring optimal power load sharing. Also, by means of simulation, the performance of the proposed LQR is compared to that of classical PI in a manner to validate its effectiveness. Finally, processor-in-the-loop validation of LQR based control technique applied to an autonomous microgrid is adopted both to check possible errors, and to verify the feasibility and the performance of the generated code. This approach leads to test the numerical equivalence between the model and real computation, which is helpful in predicting the real behavior of the system.

Keywords: Autonomous microgrid, Parallel inverters, Droop control, linear quadratic regulator, Processor-in-the-loop simulation.

Résumé :

L'utilisation croissante de micro-réseaux basés sur des générateurs distribués (DGs) parallèles aide à intégrer des sources d'énergie renouvelables locales en utilisant des onduleurs de puissance régulés. Dans cette thèse, nous nous sommes concentrés sur le développement de micro-réseaux autonomes basés sur des DGs pour résoudre les soucis liés aux problèmes de qualité d'énergie et au partage de l'énergie entre plusieurs unités, en particulier sous des perturbations générées par le changement de la charge. À cet égard, un contrôle de statisme basé sur un régulateur linéaire quadratique (LQR) équipé d'une action

intégrale a été proposé pour contribuer à l'amélioration de la qualité d'énergie du micro-réseau autonome basé sur des générateurs distribués et aider à assurer un partage optimal de la puissance de charge. Aussi, à l'aide d'une étude par simulation, la performance du LQR proposé est comparée à celle du PI classique de manière à valider son efficacité. Enfin, la validation par processeur dans la boucle de la technique de contrôle basée du contrôleur LQR appliquée au micro-réseau autonome est adoptée à la fois pour vérifier les erreurs possibles et pour vérifier la faisabilité et les performances du code généré. Cette approche permit de tester l'équivalence numérique entre le modèle et le calcul réel, ce qui est utile pour prédire le comportement réel du système.

Mots-clés : Micro-réseau autonome, Onduleurs parallèles, Contrôle de statisme, Régulateur quadratique linéaire, Simulation par processeur dans la boucle.

ملخص :

يساعد الاستخدام المتزايد للشبكات الدقيقة القائمة على المولدات الموزعة (DGs)في دمج مصادر الطاقة المتجددة المحلية RESs باستخدام محولات الطاقة الإلكترونية المحكومة. في هذه المذكرة، ركزنا على تطوير شبكة ميكروية مستقلة قائمة على DGs لمعالجة المشكلات المتعلقة بمشاكل جودة الطاقة وتقاسم الطاقة بين عدة وحدات خاصة في ظل الاضطرابات الناتجة عن اختلافات الإدخال وتغيير الحمل. في هذا الصدد، تم اقتراح التحكم المستند إلى LQR-I والمجهز بإجراءات متكاملة مثالية للمساهمة في تحسين جودة الطاقة للشبكة الصغيرة المستقلة استنادًا إلى المولدات الموزعة والمساعدة في ضمان المشاركة المثلى للحمل. أيضًا، عن طريق المحاكاة، تتم مقارنة أداء متحكم LQR المقترح بأداء متحكم PI الكلاسيكي وذلك للتحقق من فعاليته. أخيرًا، تم اعتماد التحقق من صحة المعالج في الحلقة لتقنية التحكم القائمة على LQR-I المطبقة على الشبكة الصغيرة المستقلة للتحقق من الأخطاء المحتملة، وللتحقق من جدوى وأداء الكود الذي تم إنشاؤه. يؤدي هذا النهج إلى اختبار التكافؤ العددي بين النموذج والحساب الحقيقي مما يساعد في التنبؤ بالسلوك الحقيقي للنظام.

الكلمات المفتاحية: شبكة ميكروية؛ عاكس على التفرع؛ التحكم في التدلي؛ متحكم خطي تربيعي؛ محاكاة بواسطة المعالج في الحلقة